Electronic Supporting Information (ESI) accompanying

Screening Metal-Organic Frameworks for Mixture Separations in Fixed-Bed Adsorbers using a Combined Selectivity/Capacity Metric

Rajamani Krishna

Van 't Hoff Institute for Molecular Sciences, University of Amsterdam, Science Park 904,

1098 XH Amsterdam, The Netherlands

E-mail: r.krishna@contact.uva.nl

Table of Contents

1. Preamble

This Electronic Supporting Information (ESI) accompanying the article *Screening Metal-Organic Frameworks for Mixture Separations in Fixed-Bed Adsorbers using a Combined Selectivity/Capacity Metric* provides (a) methodology used for transient breakthrough simulations, (b) analytic solutions to the shock wave model for fixed bed transient operations, (c) structural information on the MOFs investigated, (d) unary isotherm data for each guest/host combination, and (e) details simulation results for each of the investigated systems.

The information provided in this ESI is sufficiently detailed to enable interested researchers and practitioners to reproduce all of the calculations presented in this article.

For ease of reading, this ESI is written as a stand-alone document; as a consequence, there is some overlap of material with the main manuscript.

Two video animations for transient breakthrough simulations for 20/80 Xe/Kr mixtures at 298 K and 100 kPa in a fixed bed packed with SBMOF-2 are also uploaded. The first video shows the transient development of the gas phase concentrations of Xe, and Kr along the length of the fixed bed adsorber. The second video shows the transient development of the molar loadings within the SBMOF-2 along the length of the fixed bed adsorber.

2. Simulation methodology for transient breakthrough in fixed bed adsorbers

Fixed beds, packed with crystals of microporous materials, are commonly used for separation of mixtures (see schematic in Figure 1); such adsorbers are commonly operated in a transient mode, and the compositions of the gas phase, and component loadings within the crystals, vary

with position and time. During the initial stages of the transience, the pores are loaded up gradually, and only towards the end of the adsorption cycle are conditions corresponding to pore saturation attained. Put another way, separations in fixed bed adsorbers are influenced by both the Henry regime of adsorption as well as the conditions corresponding to pore saturation. For a given separation task, transient breakthroughs provide more a realistic evaluation of the efficacy of a material, as they reflect the combined influence of adsorption selectivity, and adsorption capacity.[1, 2]

We describe below the simulation methodology used to perform transient breakthrough calculations that are presented in this work. This simulation methodology is the same as that used in our previous published works.[1, 2]

Assuming plug flow of an *n*-component gas mixture through a fixed bed maintained under isothermal, isobaric, conditions, the molar concentrations in the gas phase at any position and instant of time are obtained by solving the following set of partial differential equations for each of the species *i* in the gas mixture.[3]

$$\frac{\partial c_i(t,z)}{\partial t} + \frac{\partial\left(v(t,z)c_i(t,z)\right)}{\partial z} + \frac{\left(1-\varepsilon\right)}{\varepsilon}\rho\frac{\partial \bar{q}_i(t,z)}{\partial t} = 0; \quad i = 1,2,...n \tag{1}$$

In equation (1), t is the time, z is the distance along the adsorber, ρ is the framework density, ε is the bed voidage, v is the interstitial gas velocity, and $\bar{q}_i(t,z)$ is the *spatially averaged* molar loading within the crystallites of radius r_c, monitored at position z, and at time t. The time $t = 0$, corresponds to the time at which the feed mixture is injected at the inlet to the fixed bed. Prior to injection of the feed, it is assumed that an inert, non-adsorbing, gas flows through the fixed bed.

At any time t, during the transient approach to thermodynamic equilibrium, the spatially averaged molar loading within the crystallite r_c is obtained by integration of the radial loading profile

$$\bar{q}_i(t) = \frac{3}{r_c^3}\int_0^{r_c} q_i(r,t) r^2 dr \tag{2}$$

For transient unary uptake within a crystal at any position and time with the fixed bed, the radial distribution of molar loadings, q_i, within a spherical crystallite, of radius r_c, is obtained from a solution of a set of differential equations describing the uptake

$$\frac{\partial q_i(r,t)}{\partial t} = -\frac{1}{\rho}\frac{1}{r^2}\frac{\partial}{\partial r}\left(r^2 N_i\right) \tag{3}$$

The molar flux N_i of component i may be described by the simplified version of the Maxwell-Stefan equations in which both correlation effects and thermodynamic coupling effects are considered to be of negligible importance [1]

$$N_i = -\rho Đ_i \frac{\partial q_i}{\partial r} \tag{4}$$

Summing equation (**2**) over all n species in the mixture allows calculation of the *total average* molar loading of the mixture within the crystallite

$$\bar{q}_t(t,z) = \sum_{i=1}^{n} \bar{q}_i(t,z) \tag{5}$$

The *interstitial* gas velocity is related to the *superficial* gas velocity by

$$v = \frac{u}{\varepsilon} \tag{6}$$

The adsorber bed is assumed to be initially free of adsorbates, i.e. we have the initial condition

$$t = 0; \quad q_i(0,z) = 0 \tag{7}$$

Equation (7) is relevant to the operation of the transient breakthrough experiments on a laboratory scale, but are not truly reflective of industrial operations.

At time, $t = 0$, the inlet to the adsorber, $z = 0$, is subjected to a step input of the n-component gas mixture and this step input is maintained till the end of the adsorption cycle when steady-state conditions are reached.

$$t \geq 0; \quad p_i(0,t) = p_{i0}; \quad u(0,t) = u_0 \tag{8}$$

where $u_0 = v_0\varepsilon$ is the superficial gas velocity at the inlet to the adsorber.

If the value of $\frac{Đ_i}{r_c^2}$ is large enough to ensure that intra-crystalline gradients are absent and the entire crystallite particle can be considered to be in thermodynamic equilibrium with the surrounding bulk gas phase at that time t, and position z of the adsorber

$$\bar{q}_i(t,z) = q_i(t,z) \tag{9}$$

The molar loadings at the *outer surface* of the crystallites, i.e. at $r = r_c$, are calculated on the basis of adsorption equilibrium with the bulk gas phase partial pressures p_i at that position z and time t. The adsorption equilibrium can be calculated on the basis of the Ideal Adsorbed Solution Theory (IAST) of Myers and Prausnitz.[4] In all the simulation results we present in this article, the IAST calculations use pure component isotherms fitted with Langmuir, Langmuir-Freundlich, or the dual-site Langmuir-Freundlich models, as appropriate for each case. For all the simulations presented in this article, the diffusional effects are considered to be negligible.

For presenting the breakthrough simulation results, we use the dimensionless time, $\tau = \frac{tu}{L\varepsilon}$, obtained by dividing the actual time, t, by the characteristic time, $\frac{L\varepsilon}{u}$, where L is the length of adsorber, u is the superficial fluid velocity, ε is the bed voidage.[5]

For all the simulations reported in this article we choose the following: adsorber length, L = 0.3 m; cross-sectional area, A = 1 m^2; superficial gas velocity in the bed, u_0 = 0.04 m s^{-1}; voidage of the packed bed, ε = 0.4. Also, the total pressures is assumed to be constant along the length of the fixed bed. Please note that since the superficial gas velocity is specified, the specification of the cross-sectional area of the tube, A, is not relevant in the simulation results presented. The total volume of the bed is $V_{bed} = LA$. The volume of MOF used in the simulations is $V_{ads} = LA(1-\varepsilon)$ = 0.18 m^3. If ρ is the framework density, the mass of the adsorbent in the bed is $m_{ads} = \rho LA(1-\varepsilon)$ kg. It is important to note that the volume of adsorbent, V_{ads}, includes the pore volume of the adsorbent material. In these breakthrough simulations we use the same volume of adsorbent in the breakthrough apparatus, i.e. (1 - ε) A L = 0.18 m^3 = 180 L. In all of the transient breakthrough simulations reported in this work, the value of $\frac{Đ_i}{r_c^2}$ is chosen to be large enough to ensure that intra-crystalline gradients are absent and the entire crystallite particle can be considered to be in thermodynamic equilibrium.

As illustration, Figure 2 presents results of transient breakthrough simulations for 20/80 Xe/Kr mixtures at 298 K and 100 kPa in a fixed bed packed with SBMOF-2. Figure 2a plots the dimensionless concentrations of Xe and Kr along the dimensionless length of the adsorber, $\frac{z}{L}$.

Figure 2b plots the dimensionless concentrations of Xe and Kr at the exit of the fixed bed, $z = L$, as a function of the dimensionless time, $\tau = \frac{tu}{L\varepsilon}$.

The corresponding plots of the component molar loadings are shown in Figures 2c,d.

The dotted lines in Figure 2 are the breakthroughs anticipated on the basis of a model that assumes that the spatio-temporal developments of the concentrations follows that of "shock waves", discussed in the following section.

We define the displacement time interval, $\Delta\tau = \tau_{Xe} - \tau_{Kr}$, as the difference between the breakthrough times of Xe (= τ_{Xe}) and Kr (= τ_{Kr}). During the displacement interval, $\Delta\tau$, that pure Kr with < 1000 ppm Xe can be recovered; see Figure 3a. Pure Xe, with < 1000 ppm Kr, can be recovered during the desorption cycle; see Figure 3b. The desorption cycle is simulated by purging the equilibrated bed with non-adsorbing gas such as helium (considered as the third component in the mixture). Please also note that the *y*-axes in Figure 3 are calculated on a helium-free basis.

3. Shock wave model for binary A/B mixtures in fixed beds

Kluge et al.[6] have published analytic solutions for transient breakthroughs of binary gas mixtures that are based on the assumption that the breakthroughs can be described in terms of "shock waves" that traverse the bed at two different velocities. For an A/B binary mixture, the more poorly adsorbed component B traverses the bed faster, and breaks through earlier; the more strongly adsorbed component A traverses the bed a lower velocity and breaks through at longer times. The analytic solutions are based on the following set of assumptions:

(1) Isothermal conditions prevail in the fixed bed

(2) The total pressure, p_t, is constant along the length L of the fixed bed, i.e. no pressure drop is taken into account

(3) Plug flow of gas through the bed

(4) No diffusional resistances, either intra-crystalline or external to the particles in the bed.

For the binary mixture of A, and B, equation (1) is written by Kluge et al.[6] in the form

$$\begin{aligned}\left(\frac{\varepsilon}{(1-\varepsilon)}\right)\frac{\partial c_A}{\partial t}+\rho\frac{\partial q_A}{\partial t}+\frac{1}{(1-\varepsilon)}\frac{\partial(uc_A)}{\partial z}=0\\ \left(\frac{\varepsilon}{(1-\varepsilon)}\right)\frac{\partial c_B}{\partial t}+\rho\frac{\partial q_B}{\partial t}+\frac{1}{(1-\varepsilon)}\frac{\partial(c_B)}{\partial z}=0\end{aligned} \qquad (10)$$

In equations (10), u is the superficial gas velocity, $u=v\varepsilon$. Equations (10) should be comparable to equations (1) and (2) of Kluge et al.[6] It should be noted, that equations (1) and (2) of Kluge et al.[6] contain an additional term for the contribution of the pore volume; this term is absent in equations (10), because in our formulation, the volume of adsorbent, V_{ads}, includes the pore volume of the adsorbent material; in other words, we use the appropriate density ρ, for the adsorbent material. Indeed, our formulation is also consistent with the work of Malek and Farooq.[7] Readers should also note that Kluge et al.[6] write the gas phase concentrations, and component loadings in mass units. Herein, we use molar units consistently. Furthermore, in the following set of equations, A is considered to be the more strongly adsorbed component, and B, the component that is more weakly adsorbed. In the set of equations presented by Kluge et al., component 1 is more weak adsorbed, and component 2 is more strongly adsorbed species.

The initial and boundary conditions are

$$\begin{aligned}&c_A=c_{A0};c_B=c_{B0};u=u_0;\quad t\geq 0;z=0\\ &c_A=0;c_B=0;q_A=0;q_B=0;\quad t=0;\quad 0<z<L\end{aligned} \qquad (11)$$

The ideal gas law dictates $c_A + c_B = c_t = \frac{p_t}{RT}$.

Kluge et al.[6] solve the set of equations (10), and (11) assuming that the spatio-temporal variations of concentrations as a function of the dimensionless length, $\frac{z}{L}$, and dimensionless time, $\tau = \frac{tu}{L\varepsilon}$, are represented by shock wave fronts, shown as dotted lines in Figures 1a,b.

The solutions for the spatio-temporal development of concentration have the form given below

$$
\begin{aligned}
c_A(z,t) &= c_{A0} - c_{A0}\Phi\left(\frac{z}{L} - \frac{t}{t_A}\right) \\
c_B(z,t) &= c_{B0} + (c_{dis} - c_{B0})\Phi\left(\frac{z}{L} - \frac{t}{t_A}\right) - c_{dis}\Phi\left(\frac{z}{L} - \frac{t}{t_B}\right) \\
q_A(z,t) &= q_{A0} - q_{A0}\Phi\left(\frac{z}{L} - \frac{t}{t_A}\right) \\
q_B(z,t) &= q_{B0} + (q_{dis} - q_{B0})\Phi\left(\frac{z}{L} - \frac{t}{t_A}\right) - q_{dis}\Phi\left(\frac{z}{L} - \frac{t}{t_B}\right)
\end{aligned}
\qquad (12)
$$

where

$$\Phi(\zeta) = \begin{Bmatrix} 1, \zeta \geq 0 \\ 0, \zeta < 0 \end{Bmatrix}$$

is the Heaviside function. The subscript dis, refers to values during the displacement interval. For isobaric operations, the molar concentration $c_{dis} = c_{A0} + c_{B0}$. In dimensionless form, transient development of gas phase concentrations may be written as

$$
\begin{aligned}
\frac{c_A(z,\tau)}{c_{A0}} &= 1 - \Phi\left(\frac{z}{L} - \frac{\tau}{\tau_A}\right) \\
\frac{c_B(z,\tau)}{c_{B0}} &= 1 + \left(\frac{y_A}{y_B}\right)\Phi\left(\frac{z}{L} - \frac{\tau}{\tau_A}\right) - \frac{1}{y_B}\Phi\left(\frac{z}{L} - \frac{\tau}{\tau_B}\right)
\end{aligned}
\qquad (13)
$$

where c_{A0} and c_{B0} are the molar concentrations of the gaseous components entering the fixed bed, with mole fractions mole fractions y_A, and $y_B = 1 - y_A$; τ is the dimensionless time, $\tau = \frac{tu}{L\varepsilon}$; τ_A, and τ_B are the dimensionless breakthrough times of A, and B, respectively; since A is more strongly adsorbed, $\tau_A > \tau_B$. As illustration, Figure 4 presents the shock wave solution for breakthrough of a mixture of CO_2 (= A) and CH_4 (= B) in fixed bed adsorber packed with pellets of activated carbon.

Alternatively, equation (12) may be expressed in terms of mole fractions in the gas phase:

$$\begin{aligned} y_A(z,\tau) &= y_{A0} - y_{A0}\Phi\left(\frac{z}{L} - \frac{\tau}{\tau_A}\right) \\ y_B(z,\tau) &= y_{B0} + (1 - y_{B0})\Phi\left(\frac{z}{L} - \frac{\tau}{\tau_A}\right) - \Phi\left(\frac{z}{L} - \frac{\tau}{\tau_B}\right) \end{aligned} \tag{14}$$

The "shock wave" solutions for separation of 20/60 Xe/Kr mixtures in SBMOF-2 are shown by the dotted lines in Figure 2.

The equilibrated molar loading of the more strongly adsorbed component A in the bed is

$$q_A = \frac{c_{A0}}{m_{ads}}\left(u_0 A t_A - \varepsilon V_{bed}\right) = \frac{c_t y_A}{\rho LA(1-\varepsilon)}\left(v_0 \varepsilon A t_A - \varepsilon LA\right) = \frac{\varepsilon}{(1-\varepsilon)}\frac{c_t y_A}{\rho}\left(\tau_A - 1\right) \tag{15}$$

where $\tau_A = \frac{v_0 t_A}{L}$ is the dimensionless time at which A breaks through. Equation (15) is equivalent to equation (10) of Kluge et al.[6], but expressed consistently in molar units. In equation (15), the mole fraction y_A refers to the mole fraction of component A in the inlet feed mixture; this was denoted as y_{A0} in equation (14).

The equilibrated molar loading of the more poorly adsorbed component B in the bed, at the end of the adsorption cycle, is

$$q_B = \frac{c_{B0}}{m_{ads}}\left(v_0 \varepsilon A t_A - \varepsilon v_0 A\left(t_A - t_B\right) - \varepsilon LA\right) - \frac{c_{A0}}{m_{ads}} v_0 \varepsilon A\left(t_A - t_B\right) \tag{16}$$

Equation (16) is equivalent to equation (12) of Kluge et al.[6], but expressed in molar units. We assume for the purposes of our development that the interstitial velocity remains constant during the entire breakthrough, and equals v_0 at the inlet.

Equation (16) simplifies to

$$q_B = \frac{\varepsilon}{\left(1-\varepsilon\right)} \frac{c_t y_B}{\rho}\left(\tau_A - 1\right) - \frac{\varepsilon}{\left(1-\varepsilon\right)} \frac{c_t}{\rho}\left(\tau_A - \tau_B\right). \tag{17}$$

The number of moles of gas that is purged during the time interval $t_B < t < t_A$ per kg of adsorbent in the bed is derived from a combination of equations (15), and (16)

$$\frac{\left(c_{A0} + c_{B0}\right)}{m_{ads}} u_{dis} A\left(t_A - t_B\right) = \left(q_A \frac{p_B}{p_A} - q_B\right) = \left(q_A \frac{y_B}{1 - y_B} - q_B\right) \tag{18}$$

In equation (18), mole fractions y_A, and $y_B = 1 - y_A$, are the mole fractions of the feed gas mixture. During the interval $t_B < t < t_A$ the purge gas contains only "pure" B and therefore equation (18) is the productivity of pure B, expressed per kg of adsorbent. Equation (18) is an important new result that was not derived by Kluge et al.[6]

Figure 4 presents a comparison of the shock wave solution (equations (12)) for the transient breakthrough of CO_2 and CH_4 mixture in fixed bed adsorber packed with pellets of activated carbon operating at 293 K and constant total pressure of 501 kPa with experimental data reported in Table 1 and Figure 2 of Kluge et al.[6]. From the experimental data on transient breakthroughs, the equilibrated loadings of CO_2 and CH_4 can be determined using Equation (15), and Equation (16), respectively. The productivity of CH_4 can be determined from Equation (18).

In all of the breakthrough simulations presented in this work, the fixed bed adsorber is packed with MOFs that occupy the same volume $V_{ads} = LA(1-\varepsilon)$. Therefore, the appropriate metric for comparing the MOFs is the separation potential that is expressed per volume of adsorbent material:

$$\Delta Q_{B/A} = Q_A \frac{y_B}{1-y_B} - Q_B \tag{19}$$

Equation (19) defines the productivity of pure B, expressed in the units moles of B purged from the fixed bed adsorber during the $t_B < t < t_A$, per m^3, or per L, of adsorbent in the packed bed. Since the expression is derived from the shock wave model for the adsorber, this productivity represents the *theoretical maximum* that is achievable. The separation potential, defined by $\Delta Q_{B/A} \equiv \left(Q_A \frac{y_B}{1-y_B} - Q_B \right)$, reflects the separation capability of the MOF. A different way of expressing the separation potential is to invoke the definition of the adsorption selectivity, $S_{A/B}$

$$S_{A/B} = \frac{q_A / q_B}{y_A / y_B} \tag{20}$$

where the q_A, and q_B represent the molar loadings within the MOF that is in equilibrium with a bulk gas phase with partial pressures p_A, and p_B. The molar loadings, also called *gravimetric uptake capacities*, are usually expressed with the units mol kg^{-1}. The *volumetric uptake capacities*, are

$$Q_A = \rho q_A; \quad Q_B = \rho q_B \tag{21}$$

where ρ is the crystal framework density of the MOF, expressed say in unis of kg m^{-3}, or kg L^{-1}.

The uptake capacities can be calculated using pure components isotherm fits, along with the mixed-gas Langmuir model or the Ideal Adsorbed Solution Theory (IAST) of Myers and Prausnitz [4] for binary adsorption equilibrium.

Combining equations (19) and (20), we obtain

$$\Delta Q_{B/A} = Q_A \frac{y_B}{1-y_B}\left(1-\frac{1}{S_{A/B}}\right) \tag{22}$$

Therefore, we may view the separation potential as a combined selectivity/capacity metric.

4. Separation of binary A/B mixtures with 20 "hypothetical" MOFs

To gain insights into the relative importance of selectivity and capacity metrics, we investigated the separation of binary A/B mixtures using 20 different "hypothetical" HypMOFs. The unary adsorption isotherms for each HypMOF is described by the 1-site Langmuir isotherm

$$q = q_{sat}\frac{bp}{1+bp} \tag{23}$$

We take the saturation capacity of both A and B to be identical to each other. This allows the use of the mixed-gas Langmuir model

$$\frac{q_A}{q_{sat}} = \frac{b_A p_A}{1+b_A p_A + b_B p_B}; \quad \frac{q_B}{q_{sat}} = \frac{b_B p_B}{1+b_A p_A + b_B p_B} \tag{24}$$

Twenty different "hypothetical" HypMOFs are "constructed" by choice of the three parameters q_{sat}, b_A, b_B; ten of the HypMOFs have $q_{sat} = 2.5$ mol kg^{-1}; for the other ten MOFs, $q_{sat} = 5$ mol kg^{-1}. The values of b_A, b_B are chosen to realize selectivities of 1.5, 2, 4, 6, 8, 10, 20, 10^2, 10^3, and 10^4; see Table 1. In all cases, the Langmuir parameters are chosen such that species A is more

strongly adsorbed. The chosen parameters are: adsorber length, L = 0.3 m; cross-sectional area, A = 1 m^2; superficial gas velocity in the bed, u = 0.04 m s^{-1}; voidage of the packed bed, ε = 0.4.

Let us set the scene by first analyzing separations with HypMOF-17 that is described by, $q_{sat} = 5$ mol kg^{-1}, and $S_{A/B} = b_A/b_B = 10$. The feed gas mixture composition, y_A = 0.8, and total pressure constant at the value $p_t = p_A + p_B = 100$ kPa. Figure 5 presents the results of the transient breakthrough simulations. In all the plots, the x- axis is dimensionless time, $\tau = \frac{tu}{L\varepsilon}$, obtained by dividing the actual time, t, by the characteristic time, $\frac{L\varepsilon}{u}$, where L is the length of adsorber, u is the superficial fluid velocity, ε is the bed voidage.[5] Figure 5a plots the gas phase molar concentrations exiting the packed bed, and Figure 5b shows the corresponding gas phase mole fractions of A and B in the exit of the fixed bed adsorber. The more strongly adsorbed A is the component that elutes last; the less strongly adsorbed B breaks through earlier. We demand a purity of 99.95% B, and the breakthrough time for A, τ_A, is defined as the dimensionless time at which the composition of A in the outlet gas is 0.05%. Figure 5c shows the spatially averaged molar loadings of A and B within the HypMOFs in the fixed, plotted as a function of dimensionless time. There is a finite time interval, $\Delta\tau$, during which pure 99.95% pure B can be produced. From a material balance on the adsorber, we determine the number of moles of B that can be produced per liter of adsorbent in the packed bed.

For any given HypMOF, with specified set of isotherm characteristics, there is a theoretical maximum to the value of the amount of pure B can be produced per L of adsorbent.

For HypMOF-17, for y_A = 0.8, the value of the separation potential $\Delta Q_{B/A}$ = 1.084 mol L^{-1}. For the specified purity level, Figure 5d shows the number of moles of 99.95% pure B that can be recovered from the exit product gas, express per L of HypMOF in the packed bed, as a

function of the dimensionless time. The productivity of pure B increases from 0 mol L^{-1} at $\tau = \frac{tu}{L\varepsilon}$ = 160.6, to the value of 1.053 mol L^{-1} at $\tau = \frac{tu}{L\varepsilon}$ = 204.4. The productivity of pure B plummets to zero for longer times because of the increasing presence of A in the product gas. The achieved productivity of 1.053 is slightly lower than the value of the separation potential, $\Delta Q_{B/A}$ = 1.084 mol L^{-1}. The reason for the lowering, albeit slight, of the productivity in a fixed bed is that the breakthrough characteristics have a slightly distended character. The extent to which the breakthrough shows distended characteristics is related to the separation selectivity. The lower the separation selectivity, the more pronounced is the degree of distention, and the productivity is reduced.

Since the concept of the separation potential is an important new concept, we present additional verification by presenting transient breakthrough simulation results for HypMOF-17 using the feed gas composition, y_A = 0.2. The corresponding results are shown in Figure 6. The discussions regarding Figures 6a,b,c are precisely analogous to that in the foregoing section. Since the feed mixture is richer in B, a higher amount of pure B can be produced. Figure 6d shows the number of moles of 99.95% pure B that can be recovered from the exit product gas, express per L of HypMOF in the packed bed, as a function of the dimensionless time. The productivity of pure B increases from 0 mol L^{-1} at $\tau = \frac{tu}{L\varepsilon}$ = 152.04, to the value of 11.0 mol L^{-1} at $\tau = \frac{tu}{L\varepsilon}$ = 583.2. The productivity of pure B plummets to zero for longer times because of the increasing presence of A in the product gas. The achieved productivity of 11.0 mol L^{-1} is slightly lower than the value of the separation potential, $\Delta Q_{B/A}$ = 12.4 mol L^{-1}, calculated using equation (19).

In order to confirm the key results portrayed in Figures 5d, and 6d, we carried out a set of transient breakthrough experiments for HypMOF-17 with, $q_{sat} = 5$ mol kg^{-1}, and $S_{A/B} = b_A/b_B = 10$ with varying feed gas mixture compositions, y_A = 0.1 (0.1)…0.9, keeping the total pressure constant at the value $p_t = p_A + p_B = 100$ kPa. Figure 7a plots the number of moles of B produced per liter of HypMOF in the packed bed as a function of the differences in dimensionless breakthrough times, $\Delta\tau$. There is a perfect linear correlation between the two sets as expected; a larger difference in dimensionless breakthrough times, $\Delta\tau$, results in a higher productivity of 99.95% pure B. Figure 7b presents a plot of the number of moles of B produced per liter of HypMOF in the packed bed, as a function of the separation potential, $\Delta Q_{B/A}$, calculated using equation (19). Again, we note that there is a perfect linear relation between the two sets of results. The actual amount of 99.95% pure B produced in the fixed bed is lower than the theoretical maximum dictated by the separation potential. The separation potential $\Delta Q_{B/A}$ will be attained to an increasing extent at higher selectivities.

Figure 7b is another key result that will be tested for screening 20 different HypMOFs. Transient breakthrough simulations for *equimolar* (i.e. y_A=0.5 = y_B = 1 - y_A) A/B mixtures in a fixed bed packed with twenty different HypMOFs operating at 298 K, and a total pressure of 100 kPa were undertaken. As illustration, Figure 8a shows transient breakthrough simulations for equimolar A/B mixtures in a fixed bed packed with HypMOF-9 and HypMOF-11, with adsorption isotherms as specified in Table 1. HypMOF-9 has a saturation capacity $q_{sat} = 2.5$ mol kg^{-1} and selectivity $S_{A/B} = b_A/b_B = 1000$. HypMOF-11 has a higher saturation capacity, $q_{sat} = 5$ mol kg^{-1}, but a significantly lower selectivity $S_{A/B} = b_A/b_B = 1.5$. For both HypMOFs, the more strongly adsorbed A is the component that elutes last; the less strongly adsorbed B breaks

through earlier. For HypMOF-9, with the higher selectivity, the component B breaks through practically at the start of the breakthrough "experiment".

We demand a purity of 99.95% B, and the breakthrough time for A, τ_A, is defined as the dimensionless time at which the composition of A in the outlet gas is 0.05%. The breakthroughs obtained with HypMOF-11 has a more distended characteristics, than that for HypMOF-9. The dotted lines in Figure 8a are the shock wave solutions for transient breakthroughs. Longer breakthrough times, τ_A, are obtained with HypMOFs with the higher saturation capacity. Longer breakthrough times imply that a larger amount of A can be captured in the fixed bed. Figure 8b presents a plot of the number of moles of A captured per liter of HypMOF in the packed bed. The capture capacity of A, correlates linearly with the dimensionless breakthrough time, τ_A. The first important conclusion that can be drawn is that higher saturation capacities result in larger amounts of A that can be captured in the fixed bed adsorber.

Figure 8c plots the number of moles of A captured per liter of HypMOF in the fixed bed, as a function of the selectivity $S_{A/B}$. The first conclusion that can be drawn from Figure 8c is that choosing a MOF with a higher saturation capacity leads to a higher capture capacity of A in the fixed bed. Also, importantly, the adsorption selectivity is not a good reflection of the capture capacity for A. It is also interesting to note that increase of selectivities above 10^2 does not lead to a concomitant increase in the amount of A that can be captured.

There is a finite time interval, $\Delta\tau$, during which pure 99.95% pure B can be produced. The larger value of $\Delta\tau$, the higher is the productivity of pure B. From a material balance on the adsorber, we determine the number of moles of B that can be produced per liter of adsorbent in the packed bed. Figure 8d presents a plot of the number of moles of B produced per liter of HypMOF in the packed bed, plotted as a function of the selectivity $S_{A/B}$. Again, we note that

the productivity of 99.95% B in the fixed bed does not correlate with the adsorption selectivity. Increase of selectivities above 10^2 does not lead to a concomitant increase in the amount of B that can be produced; this implies that the total exclusion of any component, i.e. infinite selectivities, may not be the best separation strategy to adopt in practice. It is better to choose a MOF with a higher saturation capacity.

In Figure 9a, the number of moles of A captured per liter of HypMOF in the fixed bed is plotted as a function of the volumetric uptake capacity of A, $Q = \rho q_A$, calculated using equation (24). There is a good correlation between the two sets of data. The number of moles of A captured in the fixed bed is lower than the volumetric uptake capacity of A, calculated from the mixed-gas Langmuir model because the adsorption selectivities of the twenty MOFs examined are finite. If the objective is to choose a MOF with the highest capture capacity of A, then the screening can be done pure on the basis of the calculations of the volumetric uptake capacity of A.

In Figure 9b, we plot the number of moles of 99.95% pure B produced per liter of HypMOF in the packed bed, as a function of the separation potential, $\Delta Q_{B/A}$, using equation (19). There is a good correlation between the two sets. The actual productivity of 99.95% pure B in the fixed bed is lower than the values of $\Delta Q_{B/A}$, calculated from the mixed-gas Langmuir model, calculated using equation (19), because the separation selectivities of the twenty MOFs are finite. Finite selectivities lead to distended breakthrough characteristics and lower productivities. As verification of this hypothesis, Figure 9c plots the % deviation between the productivity of 99.95% pure B, determined from breakthrough simulations, with the corresponding values of the separation potential, $\Delta Q_{B/A}$, calculated from the mixed-gas Langmuir model, using equation

(19). There is a significant reduction in the % deviation as the adsorption selectivity increases. At the highest selectivities, the % deviations are about 10%.

If the objective of the separation is to produce 99.95% pure B, then the screening can be done on the basis of the hierarchy of $\Delta Q_{B/A}$ values.

Pure A can only be recovered in the desorption phase. Figures 10a,b show transient breakthrough simulations for (a) adsorption, and (b) desorption phases for HypMOF-17 with, with feed gas mixture composition, y_A = 0.2, and total pressure constant at the value $p_t = p_A + p_B = 100$ kPa. In the simulations of the desorption phase, the bed was purged with a non-adsorbing gas, such as helium, injected into the equilibrated bed, at time t = 0, at a total pressure of 100 kPa. Figure 10b pure A that can be recovered from the exit product gas in the desorption cycle during a finite time interval. Transient breakthrough simulations were carried out for the desorption phase with varying feed gas mixture compositions, y_A = 0.1 (0.1)…0.9, keeping the total pressure constant at the value $p_t = p_A + p_B = 100$ kPa. The number of moles of 99.95% pure A recovered of MOF in the packed bed is plotted in Figure 10c as a function of the separation potential $\Delta Q_{A/B}$, defined as $\Delta Q_{A/B} = Q_A - Q_B \frac{y_A}{y_B} = \rho\left(q_A - q_B \frac{y_A}{1-y_A} \right)$. We again note a linear dependence of the productivity of pure A with the- separation potential. Generally speaking the breakthrough characteristics have a more distended character in the desorption phase than in the adsorption phase. Consequently the 99.95% pure A productivity is significantly lower than the productivity of 99.95% pure B; this can be verified by comparing the results in Figure 10b with the corresponding results in Figure 7b.

The key results from the analysis of the separations with twenty different MOFs, presented in Figures 7, and 9 will be used for screening MOFs for a wide variety of separation tasks.

5. Shock wave model for A/B/C ternary mixtures in fixed beds

The shock wave model for a ternary A/B/C mixture with the hierarchy of adsorption strengths A > B > C, is given in equations (12), (13), and (14) of Malek and Farooq.[7] Unfortunately, however, there are typographical errors in these equations (this has been confirmed in an email exchange with Professor S. Farooq, NUS, Singapore). The corrected set of equations, are presented below for A/B/C mixtures with the additional assumption that the interstitial velocity is constant during the entire transient breakthrough.

The dimensionless breakthrough times for A, B, and C are indicated by τ_A, τ_B, and τ_C; see schematic of breakthrough in Figure 11a. We have the hierarchy $\tau_A > \tau_B > \tau_C$. See schematic in Figure 11a.

The shock wave profiles for the mole fractions in the gas phase are

$$
\begin{aligned}
y_A(z,\tau) &= y_{A0} - y_{A0}\Phi\left(\frac{z}{L} - \frac{\tau}{\tau_A}\right) \\
y_B(z,\tau) &= y_{B0} + (1 - y_{C0} - y_{B0})\Phi\left(\frac{z}{L} - \frac{\tau}{\tau_A}\right) - (1 - y_C)\Phi\left(\frac{z}{L} - \frac{\tau}{\tau_B}\right) \\
y_C(z,\tau) &= y_{C0} + \Phi\left(\frac{z}{L} - \frac{\tau}{\tau_C}\right) + (1 - y_{C0})\Phi\left(\frac{z}{L} - \frac{\tau}{\tau_B}\right)
\end{aligned}
\tag{25}
$$

In equation (25), y_{A0}, y_{B0}, and y_{C0} are the mole fractions of the components in the inlet feed mixture; these are *not* time invariant. In proceeding further with the derivations, we denote the feed mixture compositions as y_A, y_B, and y_C. The solutions for the equilibrated molar loading of A is the same as that Equation (15):

$$
q_A = \frac{\varepsilon}{(1-\varepsilon)}\frac{c_t y_A}{\rho}(\tau_A - 1) \tag{26}
$$

The equilibrated molar loading of B is

$$q_B = \frac{\varepsilon}{(1-\varepsilon)}\frac{c_t y_B}{\rho}(\tau_A - 1) - \frac{\varepsilon}{(1-\varepsilon)}\frac{c_t}{\rho}(\tau_A - \tau_B)(1 - y_C)$$
$$q_B = q_A \frac{y_B}{y_A} - \frac{\varepsilon}{(1-\varepsilon)}\frac{c_t}{\rho}(\tau_A - \tau_B)(1 - y_C) \quad (27)$$

Equation (27) differs from equation (17) because the $(1 - y_C)$ must be introduced to account for the escape of the least adsorbed component in the gas phase.

The number of moles of B that is purged into the gas phase during the time interval $(\tau_A - \tau_B)$ is

$$\Delta q_{B/A} = \frac{\varepsilon}{(1-\varepsilon)}\frac{c_t}{\rho}(\tau_A - \tau_B)(1 - y_C) = q_A \frac{y_B}{y_A} - q_B . \quad (28)$$

The equilibrated molar loading of C is

$$q_C = \frac{\varepsilon}{(1-\varepsilon)}\frac{c_t y_C}{\rho}(\tau_A - 1) - \frac{\varepsilon}{(1-\varepsilon)}\frac{c_t}{\rho}(\tau_A - \tau_B) y_C - \frac{\varepsilon}{(1-\varepsilon)}\frac{c_t}{\rho}(\tau_B - \tau_C)$$
$$q_C = q_A \frac{y_C}{y_A} - \Delta q_{B/A}\frac{y_C}{1 - y_C} - \frac{\varepsilon}{(1-\varepsilon)}\frac{c_t}{\rho}(\tau_B - \tau_C) \quad (29)$$

The number of moles of C that can be recovered in pure form during the interval $(\tau_B - \tau_C)$ is given by $\frac{\varepsilon}{(1-\varepsilon)}\frac{c_t}{\rho}(\tau_B - \tau_A)$. The productivity of pure C, per kg of adsorbent in the fixed bed can be determined by combining equations (26), (27), and (29); the result is remarkably simple.

$$\Delta q_{C/BA} = \frac{\varepsilon}{(1-\varepsilon)}\frac{c_t}{\rho}(\tau_B - \tau_C) = q_A \frac{y_C}{y_A} - \Delta q_{B/A}\frac{y_C}{1 - y_C} - q_C \quad (30)$$

The right member of equation (30), is the separation potential for A/B/C mixtures and quantifies the maximum productivity of pure C during the adsorption cycle.

In terms of volumetric uptake capacities, IAST calculations can be used to calculate the separation potential

$$\Delta Q_{C/BA} = Q_A \frac{y_C}{y_A} - \Delta Q_{B/A} \frac{y_C}{(1-y_C)} - Q_C$$
$$\Delta Q_{C/BA} = Q_A \frac{y_C}{y_A} - \left(Q_A \frac{y_B}{y_A} - Q_B \right) \frac{y_C}{(1-y_C)} - Q_C \qquad (31)$$
$$\Delta Q_{C/BA} = (Q_A + Q_B) \frac{y_C}{1-y_C} - Q_C$$

The adsorption selectivity of B with respect to C is $S_{B/C} = \frac{Q_B}{Q_C} \frac{y_C}{y_B}$; $Q_C = \frac{Q_B}{S_{B/C}} \frac{y_C}{y_B}$, and so equation (31) may also be re-written in terms of selectivities

$$\Delta Q_{C/BA} = S_{A/B} Q_B \frac{y_C}{y_B} - Q_B (S_{A/B} - 1) \frac{y_C}{(1-y_C)} - \frac{Q_B}{S_{B/C}} \frac{y_C}{y_B}$$
$$\Delta Q_{C/BA} = \left(S_{A/B} \frac{y_C}{y_B} - (S_{A/B} - 1) \frac{y_C}{(1-y_C)} - \frac{1}{S_{B/C}} \frac{y_C}{y_B} \right) Q_B \qquad (32)$$

In order to demonstrate the validity of equation (31), Figure 11b presents results of transient breakthrough simulations for hypothetical MOF with, $q_{sat} = 5$ mol kg^{-1}, and $b_A = 0.02$ Pa^{-1}; $b_B = 0.01$ Pa^{-1}; $b_C = 0.001$ Pa^{-1} with varying feed gas mixture compositions, y_A, y_B, and y_C, keeping the total pressure constant at the value $p_t = p_A + p_B + p_c = 100$ kPa. The plot of the number of moles of 99.95% pure C produced per liter of HypMOF in the packed bed, as a function of function of the separation potential, $\Delta Q_{C/BA} = (Q_A + Q_B) \frac{y_C}{1-y_C} - Q_C$ shows a linear inter-dependence; the actual values are below the parity line. This confirms that equation (31) represents the value of the maximum productivity of pure C that can be achieved.

6. Shock wave model for A/B/C/D quaternary mixtures in fixed beds

The shock wave model for a quaternary A/B/C/D mixture with the hierarchy of adsorption strengths A > B > C > D, can be easily developed as a logical extension of the analysis of ternary mixtures in the foregoing section.

The dimensionless breakthrough times for A, B, and C are indicated by τ_A, τ_B, τ_C, and τ_D; we have the hierarchy $\tau_A > \tau_B > \tau_C > \tau_D$. See schematic in Figure 12a.

The shock wave profiles for the mole fractions in the gas phase are

$$
\begin{aligned}
y_A(z,\tau) &= y_{A0} - y_{A0}\Phi\left(\frac{z}{L} - \frac{\tau}{\tau_A}\right) \\
y_B(z,\tau) &= y_{B0} + (1 - y_{B0} - y_{C0} - y_{D0})\Phi\left(\frac{z}{L} - \frac{\tau}{\tau_A}\right) - (1 - y_C - y_D)\Phi\left(\frac{z}{L} - \frac{\tau}{\tau_B}\right) \\
y_C(z,\tau) &= y_{C0} + (1 - y_{C0} - y_{D0})\Phi\left(\frac{z}{L} - \frac{\tau}{\tau_B}\right) - (1 - y_D)\Phi\left(\frac{z}{L} - \frac{\tau}{\tau_C}\right) \\
y_D(z,\tau) &= y_{D0} + \Phi\left(\frac{z}{L} - \frac{\tau}{\tau_D}\right) + (1 - y_{D0})\Phi\left(\frac{z}{L} - \frac{\tau}{\tau_C}\right)
\end{aligned}
\tag{33}
$$

In equation (33), y_{A0}, y_{B0}, y_{C0},and y_{D0} are the mole fractions of the components in the inlet feed mixture; these are *not* time invariant. In proceeding further with the derivations, we denote the feed mixture compositions as y_A, y_B, y_C, and y_D. The solutions for the equilibrated molar loading of A is the same as that Equation (15):

$$
q_A = \frac{\varepsilon}{(1-\varepsilon)}\frac{c_t y_A}{\rho}(\tau_A - 1) \tag{34}
$$

The equilibrated molar loading of B is

$$q_B = \frac{\varepsilon}{(1-\varepsilon)}\frac{c_t y_B}{\rho}(\tau_A - 1) - \frac{\varepsilon}{(1-\varepsilon)}\frac{c_t}{\rho}(\tau_A - \tau_B)(1 - y_C - y_D)$$
$$q_B = q_A \frac{y_B}{y_A} - \frac{\varepsilon}{(1-\varepsilon)}\frac{c_t}{\rho}(\tau_A - \tau_B)(1 - y_C - y_D) \quad (35)$$

The separation potential for B/A separation is

$$\Delta q_{B/A} = \frac{\varepsilon}{(1-\varepsilon)}\frac{c_t}{\rho}(\tau_A - \tau_B)(1 - y_C - y_D) = q_A \frac{y_B}{y_A} - q_B \quad (36)$$

The equilibrated molar loading of C is

$$q_C = \frac{\varepsilon}{(1-\varepsilon)}\frac{c_t y_C}{\rho}(\tau_A - 1) - \frac{\varepsilon}{(1-\varepsilon)}\frac{c_t}{\rho}(\tau_A - \tau_B)(y_C) - \frac{\varepsilon}{(1-\varepsilon)}\frac{c_t}{\rho}(\tau_B - \tau_C)(1 - y_D)$$
$$q_C = q_A \frac{y_C}{y_A} - \Delta q_{B/A}\frac{y_C}{1 - y_C - y_D} - \frac{\varepsilon}{(1-\varepsilon)}\frac{c_t}{\rho}(\tau_B - \tau_C)(1 - y_D) \quad (37)$$

The separation potential for C/BA separation is

$$\Delta q_{C/BA} = \frac{\varepsilon}{(1-\varepsilon)}\frac{c_t}{\rho}(\tau_B - \tau_C)(1 - y_D) = q_A \frac{y_C}{y_A} - \Delta q_{B/A}\frac{y_C}{1 - y_C - y_D} - q_C \quad (38)$$

The equilibrated molar loading of D is

$$q_D = \frac{\varepsilon}{(1-\varepsilon)}\frac{c_t y_D}{\rho}(\tau_A - 1) - \frac{\varepsilon}{(1-\varepsilon)}\frac{c_t}{\rho}(\tau_A - \tau_B)y_D - \frac{\varepsilon}{(1-\varepsilon)}\frac{c_t}{\rho}(\tau_B - \tau_C)y_D - \frac{\varepsilon}{(1-\varepsilon)}\frac{c_t}{\rho}(\tau_C - \tau_D) \quad (39)$$

The separation potential for D/CBA separation is

$$\Delta q_{D/CBA} = \frac{\varepsilon}{(1-\varepsilon)}\frac{c_t}{\rho}(\tau_C - \tau_D) = q_A \frac{y_D}{y_A} - \Delta q_{B/A}\frac{y_D}{1 - y_C - y_D} - \Delta q_{C/BA}\frac{y_D}{1 - y_D} - q_D \quad (40)$$

In terms of volumetric uptake capacities, we write

$$\Delta Q_{D/CBA} = Q_A \frac{y_D}{y_A} - \Delta Q_{B/A} \frac{y_D}{1-y_C-y_D} - \Delta Q_{C/BA} \frac{y_D}{1-y_D} - Q_D \tag{41}$$

From equation (38) we write for the separation potential for C/BA separation:

$$\Delta Q_{C/BA} = Q_A \frac{y_C}{y_A} - \Delta Q_{B/A} \frac{y_C}{1-y_C-y_D} - Q_C \tag{42}$$

Combining equations (36), (41), and (42) yields

$$\begin{aligned}
\Delta Q_{D/CBA} &= Q_A \frac{y_D}{y_A} - \Delta Q_{B/A} \frac{y_D}{1-y_C-y_D} - \left(Q_A \frac{y_C}{y_A} - \Delta Q_{B/A} \frac{y_C}{1-y_C-y_D} - Q_C \right) \frac{y_D}{1-y_D} - Q_D \\
\Delta Q_{D/CBA} &= Q_A \left(\frac{y_D}{y_A} - \frac{y_C}{y_A} \frac{y_D}{1-y_D} \right) - \Delta Q_{B/A} \frac{y_D}{1-y_D} + Q_C \frac{y_D}{1-y_D} - Q_D \\
\Delta Q_{D/CBA} &= Q_A \left(\frac{y_D}{y_A} - \frac{y_C}{y_A} \frac{y_D}{1-y_D} \right) - \left(Q_A \frac{y_B}{y_A} - Q_B \right) \frac{y_D}{1-y_D} + Q_C \frac{y_D}{1-y_D} - Q_D \\
\Delta Q_{D/CBA} &= \left(Q_A + Q_B + Q_C \right) \frac{y_D}{1-y_D} - Q_D
\end{aligned} \tag{43}$$

In applying $\Delta Q_{D/CBA} = \left(Q_A + Q_B + Q_C \right) \frac{y_D}{1-y_D} - Q_D$, the hierarchy of adsorption strengths of A, B, and C is not of essentially importance; D must be the component with the lowest adsorption strength.

In order to demonstrate the validity of equation (41), Figure 12b presents results of transient breakthrough simulations for hypothetical MOF with, $q_{sat} = 5$ mol kg^{-1}, and $b_A = 0.02$ Pa^{-1}; $b_B = 0.01$ Pa^{-1}; $b_C = 0.002$ Pa^{-1}; $b_D = 0.0002$ Pa^{-1} with varying feed gas mixture compositions, y_A, y_B, y_C, and y_D keeping the total pressure constant at the value $p_t = p_A + p_B + p_C + p_D = 100$ kPa. The plot of the number of moles of 99.95% pure D produced per liter of HypMOF in the packed bed, as a function of function of the separation potential,

$\Delta Q_{D/CBA} = (Q_A + Q_B + Q_C)\frac{y_D}{1-y_D} - Q_D$ shows a linear inter-dependence; the actual values are below the parity line. This confirms that equation (41), represents the value of the maximum productivity of pure D that can be achieved.

If the desired separation task is to produce pure (D+C) product, the separation potential for DC/BA separations is given by

$$\Delta q_{DC/BA} = \frac{\varepsilon}{(1-\varepsilon)}\frac{c_t}{\rho}(\tau_B - \tau_C)(1-y_D) + \frac{\varepsilon}{(1-\varepsilon)}\frac{c_t}{\rho}(\tau_B - \tau_C)y_D + \frac{\varepsilon}{(1-\varepsilon)}\frac{c_t}{\rho}(\tau_C - \tau_D)$$

$$\Delta q_{DC/BA} = \frac{\varepsilon}{(1-\varepsilon)}\frac{c_t}{\rho}(\tau_B - \tau_C) + \frac{\varepsilon}{(1-\varepsilon)}\frac{c_t}{\rho}(\tau_C - \tau_D) \quad (44)$$

From equation (38), we get $\frac{\varepsilon}{(1-\varepsilon)}\frac{c_t}{\rho}(\tau_B - \tau_C) = \frac{\Delta q_{C/BA}}{1-y_D}$. From Equation (40), we obtain

$\frac{\varepsilon}{(1-\varepsilon)}\frac{c_t}{\rho}(\tau_C - \tau_D) = q_A\frac{y_D}{y_A} - \Delta q_{B/A}\frac{y_D}{1-y_C-y_D} - \Delta q_{C/BA}\frac{y_D}{1-y_D} - q_D$. Therefore,

$$\Delta q_{DC/BA} = \frac{\Delta q_{C/BA}}{1-y_D} + q_A\frac{y_D}{y_A} - \Delta q_{B/A}\frac{y_D}{1-y_C-y_D} - \Delta q_{C/BA}\frac{y_D}{1-y_D} - q_D$$

$$\Delta q_{DC/BA} = q_A\frac{y_C}{y_A} - \Delta q_{B/A}\frac{y_C}{1-y_C-y_D} - q_C + q_A\frac{y_D}{y_A} - \Delta q_{B/A}\frac{y_D}{1-y_C-y_D} - q_D \quad (45)$$

Collecting the terms in equation (45), we get

$$\Delta q_{DC/BA} = q_A\left(\frac{y_C}{y_A} + \frac{y_D}{y_A}\right) - \Delta q_{B/A}\frac{y_C+y_D}{1-y_C-y_D} - q_C - q_D \quad (46)$$

Substituting $\Delta q_{B/A} = q_A\frac{y_B}{y_A} - q_B$, we get

$$\Delta q_{DC/BA} = q_A\left(\frac{y_C}{y_A}+\frac{y_D}{y_A}\right)-\left(q_A\frac{y_B}{y_A}-q_B\right)\frac{y_C+y_D}{1-y_C-y_D}-q_C-q_D$$
$$\Delta q_{DC/BA} = \frac{q_A(y_C+y_D)}{y_A}\left(1-\frac{y_B}{1-y_C-y_D}\right)+q_B\frac{y_C+y_D}{1-y_C-y_D}-q_C-q_D \quad (47)$$
$$\Delta q_{DC/BA} = \frac{q_A(y_C+y_D)}{y_A}\left(\frac{1-y_C-y_D-y_B}{1-y_C-y_D}\right)+q_B\frac{y_C+y_D}{1-y_C-y_D}-q_C-q_D$$
$$\Delta q_{DC/BA} = q_A\frac{(y_C+y_D)}{1-y_C-y_D}+q_B\frac{y_C+y_D}{1-y_C-y_D}-q_C-q_D$$

In terms of volumetric uptakes, we write

$$\Delta Q_{DC/BA} = (Q_A+Q_B)\frac{y_C+y_D}{1-y_C-y_D}-(Q_C+Q_D) \quad (48)$$

7. Shock wave model for 5-component A/B/C/D/E mixtures in fixed beds

The extension of equation (43) to 5-component mixtures can be derived using the same procedure as in the foregoing section; the final result is

$$\Delta Q_{E/DCBA} = (Q_A+Q_B+Q_C+Q_D)\frac{y_E}{1-y_E}-Q_E \quad (49)$$

The extension of equation (48) to 5-component mixtures is easy to derive; the final result is

$$\Delta Q_{ED/CBA} = (Q_A+Q_B+Q_C)\frac{y_D+y_E}{1-y_D-y_E}-(Q_D+Q_E) \quad (50)$$

8. Summary of the key equations for the separation potential for multicomponent mixtures:

For binary A/B mixture, the separation potential for recovery of B from the gas phase in a fixed bed is

$$\Delta Q_{B/A} = Q_A \frac{y_B}{1-y_A} - Q_B$$

For ternary A/B/C mixture, the separation potential for recovery of C from the gas phase in a fixed bed is:

$$\Delta Q_{C/BA} = (Q_A + Q_B)\frac{y_C}{1-y_C} - Q_C$$

For quaternary A/B/C/D mixture, the separation potential for recovery of D from the gas phase in a fixed bed is:

$$\Delta Q_{D/CBA} = (Q_A + Q_B + Q_C)\frac{y_D}{1-y_D} - Q_D$$

For quinary A/B/C/D/E mixture, the separation potential for recovery of D from the gas phase in a fixed bed is:

$$\Delta Q_{E/DCBA} = (Q_A + Q_B + Q_C + Q_D)\frac{y_E}{1-y_E} - Q_E$$

For 5-component A/B/C/D/E mixture, the separation potential for recovery of a mixture of E and D from the gas phase in a fixed bed is:

$$\Delta Q_{ED/CBA} = (Q_A + Q_B + Q_C)\frac{y_D + y_E}{1-y_D-y_E} - (Q_D + Q_E)$$

9. Screening of MOFs for Xe/Kr separations

The recovery of noble gases such as Xe and Kr from used nuclear fuels is an important industrial problem.[8] In the published literature, a number of MOFs have been developed with the potential for application in the Xe/Kr separation process.[8] We screen a total of six MOFs for this separation task: NiMOF-74[9, 10] Ag@NiMOF-74,[10] CuBTC,[9, 11] SBMOF-2,[12] CoFormate[13] (= $Co_3(HCOO)_6$), and SAPO-34[14]. There is period of time during the displacement period of the

adsorption cycle, that pure Kr with < 1000 ppm Xe can be recovered; see Figure 3a for SBMOF-2. Pure Xe, with < 1000 ppm Kr, can be recovered during the desorption cycle; see Figure 3b.

Figure 13a plots the adsorption selectivity for 20/80 Xe/Kr mixtures vs Xe uptake capacity. We note that the hierarchy of S_{ads} is CoFormate > Ag@NiMOF-74 > NiMOF-74 > SBMOF-2 > SAPO-34 > CuBTC. Wang et al.[13] attribute the highly selective adsorption of Xe in CoFormate, to commensurate positioning of Xe within the cages. This commensurate positioning also implies that the intra-crystalline diffusivity of Xe will be significantly lower than that of Kr.[8, 15, 16] The introduction of well-dispersed Ag nanoparticles into NiMOF-74, results in stronger interactions of the polarizable Xe with the adsorbent Ag@NiMOF-74. The geometry of the channels of SBMOF-2 provides a better match for the larger Xe atoms rather than smaller Kr, and helps explain the selectivity for Xe over Kr.

The hierarchy of uptake capacities is Ag@NiMOF-74 > CoFormate > NiMOF-74 > SBMOF-2 > CuBTC > SAPO-34.

In order to resolve the selectivity vs uptake capacity issues, transient breakthrough simulations were undertaken for separation of 20/80 Xe/Kr mixtures at 298 K and p_t = 100 kPa in fixed beds packed with NiMOF-74, Ag@NiMOF-74, CuBTC, SBMOF-2, CoFormate, and SAPO-34.

Figure 13b plots the productivities of pure Kr, containing less than 1000 ppm Xe, as a function of the differences in dimensionless breakthrough times, $\Delta\tau$, defined as the difference between the breakthrough times of Xe and Kr. The productivity of pure Kr is linearly related to the $\Delta\tau$, as expected.

Figure 13c plots the pure Kr productivity as a function of the separation potential $\Delta Q_{Kr/Xe} = Q_{Xe}\frac{0.8}{0.2} - Q_{Kr}$, calculated from IAST. Again, a perfectly linear relation is observed. The actual productivity in the fixed beds is lower than that separation potential because of the

distended nature of the breakthrough characteristiscs. The best MOF for this separation is Ag@NiMOF-74. It is also worth noting, that a detailed analysis of the diffusional limitations of CoFormate, indicates that this MOF is subject to strong diffusional limitations that are detrimental to Kr productivity due to the enhanced distention in the breakthroughs.[2]

Pure Xe, with < 1000 ppm Kr, can be recovered during the desorption cycle; see Figure 3b for SBMOF-2. Simulations of the desorption cycles were performed to determine the productivity of pure Xe. This correlates linearly with the separation potential defined by $\Delta Q_{Xe/Kr} = Q_{Xe} - Q_{Kr}\frac{0.2}{0.8}$; see Figure 13d. The hierarchy of productivities or pure Xe is the same as the hierarchy of productivities of pure Kr.

10. Screening of MOFs for C_2H_2/CO_2 separations

Let us consider the separation of C_2H_2/CO_2 mixtures. This separation is important in industry for production of pure C_2H_2, that is required for a variety of applications in the petrochemical and electronic industries.[17] The separation is particularly challenging in view of the similarity in the molecular dimensions.[17, 18] Both molecules possess zero dipole moments and approximately the same quadrupole moment. The polarizability of C_2H_2 is slightly higher than that CO_2. On the basis of available data on unary isotherms, we conclude that four MOFs have the potential of being applied in this separation task: HOF-3 (a rod-packing 3D microporous hydrogen-bonded organic framework),[19] ZJU-60a (= Cu_2(MFDI),[20] PCP-33,[21] ZnMOF-74,[22] and UTSA-74.[22] UTSA-74 = $Zn_2(H_2O)$-(dobdc)·0.5(H2O) (H_4dobdc = 2,5-dioxido-1,4- benzenedicarboxylic acid), is an isomer of ZnMOF-74 whose synthesis has been reported by Luo et. al. [22]. It has a novel four coordinated fgl topology with one-dimensional channels of about 8.0 Å. After activation, UTSA-74a has two accessible gas binding sites per Zn^{2-} ion. All five MOFs can

selectively adsorb ethyne. With HOF-3, the preferential adsorption of ethyne over CO_2 is attributed to the unique pockets and pore surfaces.[19]

For separations of 50/50 C_2H_2/CO_2 mixtures, IAST calculations of the adsorption selectivity and volumetric and C_2H_2uptake capacities are compared in Figure 14a. HOF-3 has the highest selectivity but the lowest uptake capacity for C_2H_2 uptake. On the other hand, UTSA-74 has the highest uptake capacity for C_2H_2, but a significantly lower selectivity than HOF-3.

Transient breakthrough simulations were undertaken to productivity of 99.95% pure CO_2; the results are presented in Figure 14b as a function of the separation potential $\Delta Q = Q_{CH2} - Q_{CO2}$. The highest productivity of CO_2 is achieved with UTSA-74, primarily because of its high uptake capacity. The MOF with the highest C_2H_2/CO_2 selectivity, HOF-3, is severely limited by capacity, underscoring the fallacy of choosing MOFs based on selectivity considerations alone.

The screening of the MOFs can also be done on the basis of the volumetric capture capacity of C_2H_2 in the fixed bed; the capture capacity correlates with the IAST calculations of the volumetric uptake of C_2H_2; see Figure 14c. The hierarchy of separation performance in the two different screening methodologies leads to the same conclusion that UTSA-74 is the best MOF for C_2H_2/CO_2 mixture separations.

11. Screening of MOFs for C_2H_2/C_2H_4 separations

Cui et al. [23] report a series of coordination networks composed of inorganic anions of $(SiF_6)^{2-}$ (hexafluorosilicate, SIFSIX), that offer potential for separation of C_2H_2/C_2H_4 mixtures. In these SIFSIX materials, two-dimensional (2D) nets of organic ligand (= pyridine) and metal (Cu, Ni, or Zn) node are pillared with $(SiF_6)^{2-}$ anions in the third dimension to form 3D coordination networks that have primitive cubic topology; Figure 15a shows the structure of SIFSIX-1-Cu (1 = 4,4'-bipyridene). The pore sizes within this family of materials can be systematically tuned by

changing the length of the organic linkers, the metal node, and/or the framework interpenetration. Figure 15b shows the structure SIFSIX-2-Cu-i (2 = 4,4'-dipyridylacetylene, i = interpenetrated); in this case, each C_2H_2 molecule is bound by two F atoms from different nets. The binding of C_2H_4 with the F atoms is weaker because it is far less acidic than C_2H_2.

For separation of 1/99 C_2H_2/C_2H_4 mixtures, the selectivity vs C_2H_2 uptake plots are shown in Figure 16a for SIFSIX- (1-Cu, 2-Cu, 3-Zn, 2-Cu-i, 3-Ni), M'MOF-3a, and UTSA-100a. We note that SIFSIX-2-Cu-i (2 = 4,4'-dipyridylacetylene, i = interpenetrated) has the combination of both high selectivity and high C_2H_2 uptake capacities.

For the separation of 1/99 C_2H_2/C_2H_4 mixtures, the impurity level of C_2H_2 in the product C_2H_4 is restricted to 40 ppm. The results of the productivity of pure C_2H_4 are shown in Figure 16b, as a function of the separation potential $\Delta Q = Q_{C2H2}\frac{0.99}{0.01} - Q_{C2H4}$. There is a perfect linear relation between the productivity of C_2H_4 in the fixed bed and the IAST calculations of the separation potential.

We may also screen the MOFs on the basis of the C_2H_2 capture capacity. Figure 16c plots the C_2H_2 volumetric capture capacity in the fixed bed as a function of the volumetric uptake of C_2H_2, calculated from IAST.

Both screening procedures confirm that the best MOF is SIFSIX-2-Cu-i. The superior performance of SIFSIX-2-Cu-i has also been established by Cui et al.[23] using transient breakthrough *experiments*.

For separation of 50/50 C_2H_2/C_2H_4 mixtures, the selectivity vs C_2H_2 uptake plots are shown in Figure 17a for SIFSIX- (1-Cu, 2-Cu, 3-Zn, 2-Cu-i, 3-Ni), M'MOF-3a, and UTSA-100a. For this mixture composition, the choice of the "ideal" MOF is less clear because on the basis of selectivity, the best MOF is SIFSIX-2-Cu-i, whereas SIFSIX-1-Cu has the higher C_2H_2 uptake.

To resolve this dilemma, transient breakthrough simulations were carried out and the productivity of pure C_2H_4 (with impurity level of C_2H_2 in the product being restricted to 40 ppm) determined from a material balance on the fixed bed adsorber. The results of the productivity of pure C_2H_4 are shown in Figure 17b, as a function of the separation potential $\Delta Q = Q_{C2H2}\frac{0.5}{0.5} - Q_{C2H4}$. There is a linear relation between the productivity of C_2H_4 in the fixed bed and the IAST calculations of the separation potential. The best MOF for 50/50 C_2H_2/C_2H_4 mixture separation is SIFSIX-1-Cu, whose uptake capacity for C_2H_2 is the highest; screening MOFs on the basis of adsorption selectivity leads to an erroneous conclusion that SIFSIX-2-Cu-i is best.

We may also screen the MOFs on the basis of the C_2H_2 capture capacity. Figure 17c plots the C_2H_2 volumetric capture capacity in the fixed bed as a function of the volumetric uptake of C_2H_2, calculated from IAST. Both screening procedures confirm that the best MOF is SIFSIX-1-Cu. The superior performance of SIFSIX-1-Cu for 50/50 C_2H_2/C_2H_4 mixture separations has been established by Cui et al. [23] using transient breakthrough *experiments*.

12. Comparative analysis of MOFs for alkene/alkane separations

Ethene is an important chemical used as feedstock in manufacture of polymers such as polyethene, polyvinyl chloride, polyester, polystyrene as well as other organic chemicals. Propene is an important chemical used as feedstock in manufacture of polymers such as polypropene. Key processing steps in preparing feedstocks for polymer production are the separations of ethene/ethane, and propene/propane mixtures. The boiling points are below ambient temperatures: ethane (184.5 K), ethene (169.4 K), propane (225.4 K), propene (225.4 K). Due to the small differences in the boiling points, the separations of ethene/ethane, and

propene/propane mixtures have low relative volatilities, in the range of 1.1 – 1.2. These separations are traditionally carried out by distillation columns that operate at high pressures and low temperatures. The purity requirement of the alkenes as feedstocks to polymerization reactors is 99.95%, and consequently the distillation columns are some of the largest and tallest distillation columns used in the petrochemical industries. Several MOFs offer potential for separation of ethene/ethane and propene/propane mixtures, as alternatives to distillation.[24-30]

With potential for alkene/alkane separations are MOFs with coordinatively unsaturated metal centers that may be created by evacuation of frameworks that have metal-bound solvent molecules. This strategy has been employed to expose M^{2+} cation sites in M_2(dobdc) [M = Mg, Mn, Co, Ni, Zn, Fe; $dobdc^{4-}$ = 2,5- dioxido-1,4-benzenedicarboxylate]; these MOFs are also referred to as M-MOF-74 and CPO-27-M. Unsaturated alkynes, and alkenes such as C_2H_2, C_2H_4, and C_3H_6 can bind with Fe^{2+} of FeMOF-74, with side-on attachment and π-coordination [26]; see Figures 18a. The capability of M-MOF-74 for the technologically important separations of C_2H_2/C_2H_4, C_2H_4/C_2H_6, and C_3H_6/C_3H_8 mixtures has been established in laboratory studies.[26, 27]

For all of the MOFs that are evaluated in this article (they are listed in Tables 3, 4, 5, and 6), the adsorption favors the unsaturated alkene, and consequently, 99.95% pure alkene can only be recovered in the desorption phase. As illustration, Figures 18b,c show transient breakthrough simulations for the adsorption, and desorption cycles for separation of 50/50 C_2H_4/C_2H_6 in a fixed bed adsorber packed with CoMOF-74. For the transient breakthrough simulations of the desorption cycle, an inert non-adsorbing gas is injected into the equilibrated bed at time $t = 0$, at a total pressure of 100 kPa. The breakthrough characteristics of transient desorption cycle has more distended characteristics than that of the adsorption cycle; this is evident on visual inspection of Figures 18b,c.

Customized for C_3H_6/C_3H_8 separations, Cadiau et al.[31] report the synthesis of NbOFFIVE-1-Ni (= KAUST-7), that belongs to the same class of SIFSIX materials, using pyrazine as the organic linker; see Figure 19a. The $(SiF_6)^{2-}$ pillars in the cage are replaced with somewhat bulkier $(NbOF_5)^{2-}$ pillars. This causes tilting of the pyrazine molecule on the linker, effectively reducing the aperture opening from 0.50 nm [with $(SiF_6)^{2-}$ pillars] to 0.30 nm. The small aperture permits ingress of the smaller C_3H_6 molecules, but practically excludes C_3H_8 on the basis of subtle differences in bond lengths and bond angles.

Figures 19b,c show transient breakthrough simulations for the adsorption, and desorption cycles for separation of 50/50 C_3H_6/C_3H_8 mixtures in fixed bed adsorbers packed with KAUST-7. It is noteworthy that the desorption cycle has more distended characteristics that the adsorption cycle.

For the alkene(A)/alkane(B) mixtures, of mole fractions y_A, and y_B, the separation potentials for production of pure B (in the adsorption cycle) and pure A (in the desorption cycle) are calculated from IAST calculations using the formulae $\Delta Q_{A/B} \equiv \rho\left(q_A \frac{y_B}{1-y_B} - q_B\right)$, and $\Delta Q_{A/B} \equiv \rho\left(q_A - q_B \frac{y_A}{1-y_A}\right)$, respectively. We now validate these formulae by comparison with transient breakthrough simulations for 50/50 C_2H_4/C_2H_6 and 50/50 C_3H_6/C_3H_8 mixtures.

13. Screening of MOFs for C_2H_4/C_2H_6 separations

Let us now compare the separation of 50/50 C_2H_4/C_2H_6 mixtures at 298 K and p_t = 100 kPa using M-MOF-74 (M= Fe, Co, Mn, Mg, Zn), PAF-1-SO_3Ag[29], MIL-101-Cr-SO_3Ag[28], and NOTT-300[30]. The IAST calculations of selectivity and uptake capacity are shown in Figure 20a. The highest S_{ads} value are realized with NOTT-300, and PAF-1-SO3Ag. Simultaneous and

cooperative hydrogen-bonding, and π···π stacking interactions account for the stronger binding of C_2H_4 in NOTT-300. The π-complexation of the alkenes with Ag (I) ions of PAF-1-SO_3Ag, account for its high alkene/alkane selectivity. The C_2H_4 uptake of NOTT-300 and PAF-1-SO_3Ag are, however, significantly lower than that of M-MOF-74; the highest volumetric uptakes are obtained with FeMOF-74, and CoMOF-74. For FeMOF-74, Bloch et al.[26] have established that each alkene molecule attaches *side-on* to an Fe(II) atom in the FeMOF-74 framework.

Transient breakthrough simulations (adsorption cycle) in fixed bed adsobers were performed and the productivity of 99.95% pure C_2H_6 determined. Figure 20b shows the C_2H_6 productivities plotted as a function of the separation potential for the adsorption cycle, $\Delta Q_{C2H6/C2H4} = Q_{C2H4}\frac{0.5}{0.5} - Q_{C2H6} = \rho\left(q_{C2H4}\frac{0.5}{0.5} - q_{C2H6}\right)$, calculated from IAST. The inter-dependence is linear; the highest productivity is achieved with FeMOF-74, that significantly outperforms both NOTT-300 and PAF-1-SO_3Ag.

The screening of the MOFs can also be done on the basis of the volumetric capture capacity of C_2H_4 in the fixed bed; the capture capacity correlates with the IAST calculations of the volumetric uptake of C_2H_4; see Figure 20c. The hierarchy of separation performance in the two different screening methodologies leads to the same conclusion that FeMOF-74 is the best MOF for this separation duty.

The productivity of 99.95% pure C_2H_4, in the *desorption* cycle, are shown in Figure 20d. The productivity, determined from transient breakthrough simulations of the desorption cycle, correlates well with the separation potential for the desorption cycle: $\Delta Q_{C2H4/C2H6} = Q_{C2H4} - Q_{C2H6}\frac{0.5}{0.5} = \rho\left(q_{C2H4} - q_{C2H6}\frac{0.5}{0.5}\right)$, calculated from IAST. It is noteworthy, that the productivity of 99.95% pure C_2H_4 in any MOF is lower than the

corresponding values of the productivity of 99.95% pure C_2H_6 (cf. Figure 20b). This is because the breakthrough characteristics of transient desorption cycle has more distended characteristics than that of the adsorption cycle; cf. Figures 18a,b,c,d. The highest productivities of 99.95% pure C_2H_4 are obtained with Fe-MOF-74, coincident with the conclusions reached on the basis of the analysis of breakthroughs in the adsorption cycle. This leads us to conclude that the MOF that is best for production of 99.95% pure C_2H_4 is also the MOF that is best for production of 99.95% pure C_2H_6.

14. Screening of MOFs for C_3H_6/C_3H_8 separations

For separations of 50/50 C_3H_6/C_3H_8 mixtures, IAST calculations of the adsorption selectivity and volumetric C_3H_6 uptake capacities are compared in Figure 21a for M-MOF-74 (M= Fe, Co, Ni, Mn, Mg, Zn), 13X zeolite, LTA-5A zeolite, and KAUST-7. KAUST-7 has the highest selectivity but the lowest uptake capacity for C_3H_6 uptake. On the other hand, NiMOF-74 has the highest uptake capacity for the unsaturated alkene, but a significantly lower selectivity than KAUST-7.

Transient breakthrough simulations were undertaken to productivity of 99.95% pure C_3H_8; the results are presented in Figure 21b as a function of the separation potential $\Delta Q = Q_{C3H6}\frac{0.5}{0.5} - Q_{C3H8} = \rho\left(q_{C3H6}\frac{0.5}{0.5} - q_{C3H8}\right)$.The highest productivity of C_3H_8 is achieved with NiMOF-74, primarily because of its high uptake capacity. The MOF with the highest C_3H_6/C_3H_8 selectivity, KAUST-7, is severely limited by capacity, underscoring the fallacy of choosing MOFs based on selectivity considerations alone.

The screening of the MOFs can also be done on the basis of the volumetric capture capacity of C_3H_6 in the fixed bed; the capture capacity correlates with the IAST calculations of the

volumetric uptake of C_3H_6; see Figure 21c. The hierarchy of separation performance in the two different screening methodologies leads to the same conclusion that NiMOF-74 is the best MOF for C_3H_6/C_3H_8 mixture separations.

15. Screening of MOFs for CO_2/CH_4 separations

Separation of CO_2 from CH_4 is relevant to the purification of natural gas, which can have up to 92% CO_2 impurity at its source.[32] Removal of CO_2, which is most commonly accomplished using amine *ab*sorption technology, is conducted between 2 MPa and 7 MPa.[33] The separation requirements for production of liquefied natural gas (LNG) are rather stringent, often requiring the achievement of impurity levels of less than 500 ppm CO_2.

We first examine separations of 50/50 CO_2/CH_4 mixtures at 298 K at a total pressure of 100 kPa. Figure 22a presents IAST calculations of S_{ads} versus the CO_2 uptake capacity. The hierarchy of S_{ads} values is MgMOF-74 > 13X > NiMOF-74 > Cu-TDPAT > Kureha carbon. The hierarchy of volumetric CO_2 uptake capacity is NiMOF-74 > MgMOF-74 > 13X > Cu-TDPAT > Kureha carbon. The productivity of 99.95% pure CH_4 is linearly correlated with the separation potential $\Delta Q_{CH4/CO2} = Q_{CO2}\frac{0.5}{0.5} - Q_{CH4}$; see Figure 22b. The highest productivity is achieved with NiMOF-74 that has the higher volumetric CO_2 uptake capacity. The CO_2 capture capacity correlates linearly with the volumetric uptake capacity of CO_2. The CO_2 capture capacity in NiMOF-74 is also the highest; see Figure 22c.

The binding of CO_2 is particularly strong for M-MOF-74 frameworks. Neutron diffraction data[34] establish that CO_2 molecules attach via O atoms to the Mg atoms of the MgMOF-74 framework as pictured in Figure 23. Intuitively one might expect CO_2 molecules to undergo a rotational motion when hopping from one Mg atom to a neighbouring one. Such rotational

motion is observed in video animations of MD simulations,[35] and has also been established experimentally.[36]

For separation of CO_2 from CH_4 at high pressures, uptake capacities become increasingly important. To illustrate this, let us compare separations of 50/50 CO_2/CH_4 mixtures at 298 K using MgMOF-74, NiMOF-74, NaX zeolite (also called 13X zeolite), Kureha carbon, and Cu-TDPAT. The experimental isotherm data for Kureha carbon is available only for pressures up to 0.3 MPa;[37] consequently the comparisons of the separations are done for a total pressure of 0.6 MPa. Figure 24a presents IAST calculations of S_{ads} versus the CO_2 uptake capacity. The hierarchy of S_{ads} values is MgMOF-74 > 13X > NiMOF-74 > Cu-TDPAT > Kureha carbon. The hierarchy of volumetric CO_2 uptake capacity is NiMOF-74 > MgMOF-74 > Kureha carbon > 13X > Cu-TDPAT.

The productivity of 99.95% pure CH_4 is linearly correlated with the separation potential $\Delta Q_{CH4/CO2} = Q_{CO2}\frac{0.5}{0.5} - Q_{CH4}$; see Figure 24b. The highest productivity is achieved with NiMOF-74 that has the higher volumetric CO_2 uptake capacity. The CO_2 capture capacity in NiMOF-74 is also the highest; see Figure 24c.

The superior separation characteristics of M-MOF-74 adsorbents are also confirmed by published breakthrough experiments; these are re-analyzed using the shock wave model developed earlier.

Figures 25a, b, c, d, e present the experimental breakthrough data of Li et al.[38] for CO_2/CH_4 mixtures in packed bed with (a) Mg_2(dobdc) (= MgMOF-74), (b) Co_2(dobdc) (= CoMOF-74), (c) Ni_2(dobdc) (= NiMOF-74), (d) MIL-100(Cr), and (e) Activated Carbon (AC) at 298 K. The *y*-axis represents the % CO_2, and CH_4 of in the exit gas phase. The partial pressures at the inlet are

p_1 = 40 kPa; p_2 = 60 kPa; p_t = 100 kPa. The continuous solid lines are the shock wave model calculations using equations (14), adjusting the breakthrough times to match the experiments.

Figures 25f compares the productivity of CH_4, calculated using the left member of equation (18) for each of the five materials, with the displacement time interval, Δt. The productivity of CH_4 correlates linearly with the displacement time Δt. This plot shows clearly the superior separation capability of CoMOF-74, MgMOF-74, and NiMOF-74.

Figures 26a,b present comparisons of the experimental data of Chen et al.[39] and Yu et al.[37] for transient breakthroughs of CO_2/CH_4/He mixtures in bed packed with (a) NiMOF-74 and (b) Kureha carbon, operating at T = 298 K with the shock wave solutions, for the ternary A/B/C gas mixture (A=CO_2; B=CH_4; C=He)

$$\begin{aligned} y_A(z,\tau) &= y_A - y_A\Phi\left(\frac{z}{L}-\frac{\tau}{\tau_A}\right) \\ y_B(z,\tau) &= y_B + \left(y_{B,dis}-y_B\right)\Phi\left(\frac{z}{L}-\frac{\tau}{\tau_A}\right) - y_{B,dis}\Phi\left(\frac{z}{L}-\frac{\tau}{\tau_B}\right) \end{aligned} \tag{51}$$

where $y_{B,dis}$ = 0.333 is the mole fraction of CH_4 during the displacement interval.

The volumetric productivity of CH_4 (= B) is calculated from $\frac{\left(c_{A0}+c_{B0}+c_{B0}\right)}{m_{ads}} u_{dis} A\left(t_A - t_B\right) y_{B,dis}$. Figure 26c plots the volumetric productivity of CH_4 as a function of the displacement interval, $\Delta t = \left(t_A - t_B\right)$, i.e. the difference in the breakthrough times of A=CO_2, and B=CH_4. We note a perfect linear dependence, in line with the analysis in Figure 25.

16. Screening of MOFs for CO_2/N_2 separations

For CO_2 capture from flue gas, typically containing 15% CO_2, and 85% N_2,[40] we can rely on selective CO_2 binding with extra-framework cations (e.g. Na^+, K^+, Ca^{++}, Ba^{++}) of zeolites NaX (= 13X), LTA-4A, and LTA-5A. With MOFs, selective CO_2 binding could, for example, achieved with M^{2+} of M_2(dobdc) [Mg, Mn, Co, Ni, Zn, Fe, Cu, Mg] or M^{2+} of $M_3(BTC)_2$ [M = Cu, Cr, Mo]. Wu et al.[34] have established that the O atoms of CO_2 bind with the Mg atoms of MgMOF-74 with an associated binding energy of about 42 kJ mol^{-1}.

Figure 27a presents the IAST calculations of S_{ads} for separation of 15/85 CO_2/N_2 mixtures at 298 K using five different adsorbents: MgMOF-74,[40] NiMOF-74,[41] NaX zeolite,[42] Kureha carbon,[37] and NOTT-300.[43] Kureha carbon exhibits the lowest CO_2/N_2 selectivity. The high selectivities of MgMOF-74, and NiMOF-74 are attributable to the strong binding of CO_2 with open metal sites. The electrostatic interactions of CO_2 with the extra framework cations Na^+ and Cu^{2+} account for the high selectivities exhibited by 13 X zeolite.

The productivity of 99.95% pure N_2 is linearly correlated with the separation potential $\Delta Q_{N2/CO2} = Q_{CO2}\frac{0.85}{0.15} - Q_{N2}$; see Figure 27b. The highest productivity is achieved with MgMOF-74, followed closely by NiMOF-74.

17. Screening of MOFs for H_2 purification

Pressure swing adsorption is the most commonly used technology for recovery of pure hydrogen from a gaseous streams containing 60–90 mol% H_2.[44] Steam-methane reformer off-gas (SMROG), after it has been further treated in a water-gas shift reactor, is a commonly used feed gas stream, with typical compositions 70–80% H_2, 15–25% CO_2, 3–6% CH_4, 1–3% CO, and also containing some N_2.[44-46] The production of pure H_2 from steam-methane reformer off-gas

requires operation of PSA units at pressures reaching about 7 MPa. Typically, H_2 is required with 99.95%+ purity.[44] In fuel cell applications, the purity demands are as high as 99.999%.[47] The commonly used adsorbents are LTA-5A[48, 49] (with Na^+ and Ca^{++} extra-framework cations), and NaX[42] (also commonly denoted by its trade name 13X, with Na^+ extra-framework cations) zeolites. In recent years there has been a considerable amount of research on the development of MOFs for use as adsorbents in PSA processes.[32, 44, 46, 50, 51]

As illustration of the application of the concept of separation potential to the screening of MOFs for H_2 purification processes, we consider the separation of three representative mixtures: binary 20/80 CO_2/H_2 at 298 K and 7 MPa, ternary 40/10/50 $CO_2/CH_4/H_2$ mixtures at 298 K and 7 MPa, and quaternary 40/5/5/50 $CO_2/CO/CH_4/H_2$ mixtures at 298 K and 6 MPa.

Figure 28a presents the IAST calculations of S_{ads} for separation of 20/80 CO_2/H_2 mixtures at 298 K and 7 MPa, using MgMOF-74, 13X zeolite, LTA-5A, CuTDPAT, and MIL-101.MIL-10 exhibits the lowest CO_2/H_2 selectivity. The high selectivity of MgMOF-74 is attributable to the strong binding of CO_2 with open metal sites. The electrostatic interactions of CO_2 with the extra framework cations Na^+ and Cu^{2+} account for the high selectivities exhibited by 13X zeolite and LTA-5A.

The productivity of 99.95% pure H_2 is linearly correlated with the separation potential $\Delta Q = Q_{CO2}\frac{0.8}{0.2} - Q_{H2}$; see Figure 28b. The highest H_2 productivity is achieved with MgMOF-74.

Figure 29a present transient breakthrough simulations for separation of 40/10/50 $CO_2/CH_4/H_2$ mixtures at 298 K and 7 MPa in fixed bed adsorber packed with CuTDPAT. The sequence of breakthroughs is: H_2, CH_4, and CO_2. The purity of H_2 in the product gas exiting the adsorber is primarily dictated by the presence of CH_4, rather than CO_2, that is the main impurity in the feed gas mixture. The CH_4/H_2 adsorption selectivity are far more relevant than the CO_2/H_2 selectivity.

Figure 29b presents a comparison of productivities of 99.95% pure H_2, obtained from breakthrough simulations for four different adsorbents, plotted as a function of the separation potential $\Delta Q_{H2/(CH4+CO2)} = (Q_{CO2} + Q_{CH4})\frac{y_{H2}}{(1-y_{H2})} - Q_{H2}$, calculated from IAST. The productivity is a linearly related to ΔQ, indicating that the separation potential can be used for screening purposes. It is interesting to note that the best performing MOF is CuBTC, and not MgMOF-74 that has the highest CO_2 capture capacity. [32]

Figure 30a present transient breakthrough simulations for separation of 40/5/5/50 CO_2/CO/CH_4/H_2 mixtures at 298 K and 6 MPa in fixed bed adsorber packed with CuTDPAT. The sequence of breakthroughs is H_2, CO, CH_4, and CO_2. The purity of H_2 in the product gas exiting the adsorber is primarily dictated by the presence of CO, and CH_4, rather than CO_2, that is the main impurity in the feed gas mixture. The CO/H_2, and CH_4/H_2 adsorption selectivities are far more relevant than the CO_2/H_2 selectivity.

Figure 30b presents a comparison of productivities of 99.95% pure H_2, obtained from breakthrough simulations for four different adsorbents, plotted as a function of the separation potential, $\Delta Q_{H2/(CO+CH4+CO2)} = (Q_{CO2} + Q_{CO} + Q_{CH4})\frac{y_{H2}}{(1-y_{H2})} - Q_{H2}$, calculated from IAST. The producitivity is a linearly related to ΔQ, indicating that the separation potential can be used for screening purposes. The best performing MOF is CuBTC.

18. Screening of MOFs for separation of pentane isomers

The pentane isomers: n-pentane (nC5), and 2-methyl-butane (2MB, also called iso-pentane), form about 30%-40% of light naphtha fractions.[52] 2-methylbutane is used as a solvent and as feedstock for production of isoprene by oxidative dehydrogenation. The research octane numbers

(RON) values of nC5, and 2MB are, respectively, 61.7, and 93.5; therefore, the branched isomer may be incorporated into the gasoline pool for octane enhancement.[52] The boiling points of nC5, and 2MB are, respectively, 309 K, and 301 K; consequently, separation by distillation is expected to be prohibitively energy-intensive.

For the separation of binary 50/50 n-pentane(nC5)/2-methylbutane (2MB) mixtures, Figure 31a presents plots of the nC5/2MB selectivity vs uptake capacity of nC5. Separations with $Fe_2(BDP)_3$ are the most effective because it has the combination of both high selectivity and high 2MB uptake capacity. $Fe_2(BDP)_3$ [BDP^{2-} = 1,4-benzenedipyrazolate] [53, 54]; this MOF has one-dimensional (1D) triangular channels, that are 4.9 Å in size (see Figure 32). Linear alkanes such as *n*-pentane and *n*-hexane can align commensurately with the channel landscape (see Figure 32); this allows maximum degree of van der Waals interactions of the C atoms with the channel walls. The branched mono-branched and di-branched isomers are significantly more constrained within the triangular channels; not all of the C atoms can effectively interact with the walls.

Figure 31b presents plots of the number of moles of 99% pure 2MB recovered in fixed beds packed with $Fe_2(BDP)_3$, MFI zeolite, ZIF-8, ZIF-77, plotted as a function of the separation potential $\Delta Q_{2MB/nC5} = Q_{nC5} - Q_{2MB}$, calculated from IAST; see Figure 31d. The linearity of this plot validates the use of the separation potential for screening purposes.

19. Screening of MOFs for separation of hexane isomers

The separation of hexane isomers, n-hexane (nC6), 2-methylpentane (2MP), 3-methylpentane (3MP), 2,2 dimethylbutane (22DMB), and 2,3 dimethylbutane (23DMB) is required for production of high-octane gasoline. The values of the Research Octane Number (RON) increases with the degree of branching; the RON values are: nC6 = 30, 2MP = 74.5, 3MP = 75.5, 22DMB = 94, 23DMB = 105. Therefore, di-branched isomers are preferred products for incorporation

into the high-octane gasoline pool.[1, 55, 56] Currently, the separation of hexane isomers is performed using LTA-5A zeolite that operates on the principle of molecular sieving; see Figure 33a. Linear nC6 can hop from one cage to the adjacent cage through the 4 Å windows of LTA-5A, but branched alkanes are largely excluded. An improved separation scheme, pictured in Figure 33b, would require an adsorbent that would separate the di-branched isomers 22DMB and 23DMB from the nC6, 2MP, and 3MP; this would allow the low-RON components to be recycled back to the isomerization reactor. The separation of 22DMB and 23DMB from the remaining isomers is a difficult task because it requires distinguishing molecules on the *degree* of branching; such a separation is not feasible with the currently used LTA-5A. Typically, in such a processing scheme the aim would be to produce a product stream from the separation step with RON value > 92. This requirement of 92+ RON implies that the product stream will contain predominantly the di-branched isomers 22DMB and 23DMB, while allowing a small proportion of 2MP and 3MP to be incorporated into the product stream. Sharp separations between mono- and di- branched isomers is not a strict requirement.

Figures 34 ($Fe_2(BDP)_3$), 35 (ZIF-77), 36 (MFI), 37 (Co(BDP)), 38 (MgMOF-74), 39 (Zn(MOF-74), 40 (ZIF-8), 41 (BEA zeolite), 42 (Zn(bdc)dabco), amd 43 (ZnHBDC) showsthe transient breakthrough simulations for separation of equimolar nC6/2MP/3MP/22DMB/23DMB mixtures at 433 K and 100 kPa in fixed bed adsorber packed with different adsorbents. The sequence of breakthroughs is di-branched isomers, mon-branched isomers, and linear nC6. Also shown is the RON of product gas at the outlet of fixed bed; the RON values are calculated from the pure component values, weighted with the mole fractions in the exit gas stream at any time, *t*. There is a time interval during which product gas exiting the fixed bed has an average RON value higher than 92, the target RON value. Since the RON values of both 22DMB and 23DMB

are higher than 92, the desired separation is between 23DMB and 3MP. The appropriate expression for the separation potential is given by Equation (50):

$$\Delta Q_{(22DMB+23DMB)/(nC6+2MP+3MP)} = \left(Q_{nC6} + Q_{2MP} + Q_{3MP}\right)\frac{y_{22MB} + y_{23DMB}}{1 - y_{22MB} - y_{23DMB}} - \left(Q_{22DMB} + Q_{23DMB}\right)$$

Figure 47 compares 92+ RON productivity for a total of nine different adsorbent materials: ZnMOF-74, MgMOF-74, Co(BDP), $Fe_2(BDP)_3$, MFI, BEA, ZIF-8, Zn(bdc)dabco, and ZIF-77, plotted as a function of the separation potential $\Delta Q_{(22DMB+23DMB)/(nC6+2MP+3MP)}$, calculated from IAST. The productivity is linearly related to the separation potential. The best performing MOF for this separation duty is $Fe_2(BDP)_3$, in line with the earlier work of Herm et al.[53]

For the UiO-66, CFI, and ATS, the di-branched isomers are most strongly adsorbed and these can be recovered only during the desorption phase; see the adsorption/desorption simulations in Figures 44 (UiO-66), 45 (CFI), and 46 (ATS). The separation potential that describes the recovery of the di-branched isomers is given by

$$\Delta Q_{(22DMB+23DMB)/(nC6+2MP+3MP)} = \left(Q_{22DMB} + Q_{23DMB}\right) - \left(Q_{nC6} + Q_{2MP} + Q_{3MP}\right)\frac{1 - y_{22MB} - y_{23DMB}}{y_{22MB} + y_{23DMB}}$$

For most materials 23DMB is intermediate in adsorption strength between 22DMB and the di-branched isomer 3MP. Therefore the separation performance should be expected to be different in the ternary mixture: nC6/3MP/22DMB.

For the separation of nC6/3MP/22DMB mixtures, a total of eight different adsorbent materials have been screened: ZnMOF-74, MgMOF-74, Co(BDP), $Fe_2(BDP)_3$, MFI, BEA, ZIF-8, and ZIF-77 for operations at 300 kPa, and 433 K. We choose a target RON value of 90 because the RON of 22DMB is only 94, compared to the value of 105 for 23DMB. Typical breakthroughs are shown in Figures 48a,b for ZIF-77 and ZnMOF-74 as adsorbent; we note that there is a finite time during which product gas of 90+ RON can be recovered from the gas phase exiting the

adsorber. Figure 48c comparison of productivities of 90+ RON productivities, plotted as a function of with the values of the separation potential, calculated from IAST: $\Delta Q_{22DMB/(3MP+nC6)} = (Q_{nC6} + Q_{3MP})\frac{y_{22DMB}}{(1-y_{22DMB})} - Q_{22DMB}$. The inter-dependence is perfectly linear, confirming that ΔQ is the appropriate metric to use for screening purposes. The hierarchy of 90+ RON productivities are ZnMOF-74 > MgMOF-74 > Co(BDP) > $Fe_2(BDP)_3$ > ZIF-8 > ZIF-77 > BEA > MFI zeolite. The same hierarchy prevails for operation at a total pressure of 100 kPa; see Figure 48d.

The best MOF for separation of nC6/3MP/22DMB mixtures is ZnMOF-74.

This screening study demonstrate that the screening of MOFs must be carried out with a truly representative hexane isomer mixture, and $Fe_2(BDP)_3$ is the best choice for this separation task [1, 2, 53, 54, 56]

20. Screening of MOFs for separation of xylene isomers

Para-xylene is a valuable petrochemical feedstock; the largest use of p-xylene is in its oxidation to make terephthalic acid, that is used in turn to make polymers such as polyethylene terephthalate (PET) and polybutylene terephthalate (PBT). PET is one of the largest volume polymers in the world, and is used to produce fibers, resins, films, and blown beverage bottles.

In a commonly used separation scheme (cf. Figure 49), the xylenes rich stream from the bottom of the reformer splitter is routed to a xylenes splitter. Here, the heavier aromatics (C9+) are removed from the bottom of the column. The overhead stream from the xylenes splitter, typically containing 19% ethylbenzene, 44% m-xylene, 20% o-xylene, and 17% p-xylene, needs to be separated for recovery of p-xylene. In current technology this mixture is separated in a Simulated Moving Bed (SMB) adsorption separation unit. The adsorbent used is BaX zeolite,

that selectively adsorbs p-xylene. Since the adsorbent particles are in contact with a mixture in the *liquid* phase, the pores of the adsorbent material are practically saturated with guest molecules.[57] For mixture adsorption, let us define the fractional occupancy within the pores, θ_t

$$\theta_t = \sum_{i=1}^{n} \frac{q_i}{q_{i,sat}} \tag{52}$$

where q_i is the molar loading of species *i* in the mixture, and $q_{i,sat}$ is its saturation capacity. In the SMB unit with BaX zeolite, pore saturation prevails, i.e. $\theta_t \to 1$; the hierarchy of adsorption strengths is dictated by molecular packing, or entropy, effects.[57] Binding energies of guest molecules with the framework walls or non-framework cations do not solely determine the separation performance.

For separation of 4-component equimolar o-xylene(1)/m-xylene(2)/p-xylene(3)/ethylbenzene(4) mixtures we adopt the following definition of selectivity that was used in the paper of Torres-Knoop et al.[58]

$$S_{ads} = \frac{(q_3)/(q_1+q_2+q_4)}{(p_3)/(p_1+p_2+p_4)} = 3\frac{(q_3)}{(q_1+q_2+q_4)} \tag{53}$$

Figure 50a presents IAST calculations for p-xylene adsorption selectivity for 4-component o-xylene/m-xylene/p-xylene/ethylbenzene mixture in MAF-X8, JUC-77, Co(BDP), MIL-125, MIL-125-NH_2, and BaX zeolite, plotted against the volumetric uptake of p-xylene; these data are culled from Figure 5 of Torres-Knoop et al.[58] The highest uptake capacity is achieved with MAF-X8; this is ascribable to commensurate stacking within the 10 Å channels as evidenced in the computational snapshots in Figure 50b. The commercially used BaX zeolite has the highest adsorption selectivity, but the lowest p-xylene uptake capacity. In order to solve the selectivity/capacity dilemma, Torres-Knoop et al.[58] used breakthrough simulations and

determined the dimensionless cycle time, τ_{cycle}, in order to conclude that MAF-X8 would be expected to have the best performance in the simulated moving bed adsorber; see the plot in Figure 5b of Torres-Knoop et al.[58] Furthermore, the data plotted in Figure 5b of Torres-Knoop et al.[58] showed that the dimensionless cycle time, τ_{cycle}, correlates nicely with the IAST calculations of volumetric uptake of p-xylene.

Since the publication of the article by Torres-Knoop et al.,[58] more recent work of Mukherjee et al.[59, 60] have reported the synthesis of a Zn(II)-based dynamic coordination framework, $[Zn_4O(L)_3]$ where the ligand L = 4, 4'- ((4-(tert-butyl) - 1,2- phenylene)bis(oxy))dibenzoate; the framework gets transformed in such a manner as to allow optimal packing of p-xylene within the cavities. This structure has also been dubbed as DynaMOF-100.

We now compare the performace of MAF-X8, JUC-77, Co(BDP), MIL-125, MIL-125-NH_2, and BaX zeolite with DynMOF-100 using the concept of the separation potential. The volumetric separation potential for preferential adsorption of p-xylene, and rejection of o-xylene, m-xylene, and ethylbenzene is

$$\Delta Q_{(oX+mX+EthBz)/pX} = \left(Q_{pX}\right)\frac{y_{oX}+y_{mX}+y_{EthBz}}{1-y_{oX}-y_{mX}-y_{EthBz}} - \left(Q_{oX}+Q_{mX}+Q_{EthBz}\right) \qquad (54)$$

The hierarchy of separation potentials is in agreement with the corresponding hierarchy of volumetric uptake of p-xylene; see the comparisons in Figure 51.

Based on the comparisons in Figure 51, we conclude that the best MOFs for separation of p-xylene selective separation of xylene isomers are DynaMOF-100, and MAF-X8. However, for neither of these MOFs, there is experimental evidence in fixed bed adsorbers to confirm their potential for practical applications.

21. Screening of MOFs for styrene/ethylbenzene separations

Alkylation of benzene with ethene produces ethyl benzene (cf. Figure 52a), which is dehydrogenated to styrene, a monomer used in the manufacture of many commercial polymers and co-polymers The conversion of ethylbenzene to styrene is only partial, and the reactor product contains a large fraction, in the range of 20%-40%, of unreacted ethylbenzene. Due to the small, 9 K, difference in their boiling points, the distillation separation of styrene and ethylbenzene has to be carried out in tall vacuum towers that have high energy demands; adsorptive separations using microprous metal-organic frameworks offer energy-efficient alternatives.

In the recent screening study of Torres-Knoop et al.,[61] MIL-47(V)[62] and MIL-53(Al)[62] emerged as the best adsorbents for separation of styrene/ethylbenzene mixtures. Let us now compare the performance of MIL-47(V) and MIL-53(Al) with DynaMOF-100 that undergoes guest-induced structural changes to selectively encapsulate styrene (cf. Figure 52b).

Figure 53a presents the IAST calculations in which the x-axis is fractional occupancy, θ_t, within the pores of the MOFs. We note that the value of S_{ads} for DynaMOF-100 is about one to two orders of magnitude higher than that of MIL-47(V) and MIL-53(Al). Figure 53b compares IAST calculations for styrene uptake capacity in the three MOFs; the uptake capacity of DynaMOF-100 is higher than that of the other two MOFs. Figure 53c presents a plot of selectivity vs uptake capacity at pore saturation, $\theta_t \approx 1$. Due to the significantly higher adsorption selectivity, and higher styrene uptake capacity, we should expect separations with DynaMOF-100 to be significantly superior to those realized with either MIL-47(V) or MIL-53(Al).

Figure 53d presents a plot of the separation potential, $\Delta Q_{EthBz/Sty} = Q_{St} - Q_{EthBz}$, vs styrene uptake capacity at $\theta_t \approx 1$. The clear superiority of DynaMOF-100 for styrene/ethylbenzene separations needs, however, to be established by experiments in fixed bed adsorbers.

22. Notation

A	cross-sectional area of breakthrough tube, m^2
b_A	dual-Langmuir-Freundlich constant for species i at adsorption site A, $Pa^{-\nu_A}$
b_B	dual-Langmuir-Freundlich constant for species i at adsorption site B, $Pa^{-\nu_B}$
c_i	molar concentration of species i in gas mixture, mol m^{-3}
c_{i0}	molar concentration of species i in gas mixture at inlet to adsorber, mol m^{-3}
$Đ_i$	Maxwell-Stefan diffusivity, m^2 s^{-1}
f_i	partial fugacity of species i, Pa
f_t	total fugacity of bulk fluid mixture, Pa
L	length of packed bed adsorber, m
n	number of species in the mixture, dimensionless
N_i	molar flux of species i, mol m^{-2} s^{-1}
p_i	partial pressure of species i in mixture, Pa
p_t	total system pressure, Pa
q_i	molar loading of species i, mol kg^{-1}
$q_{i,sat}$	molar loading of species i at saturation, mol kg^{-1}
q_t	total molar loading in mixture, mol kg^{-1}
Q	volumetric loading in adsorbed phase, mol m^{-3}
ΔQ	separation potential, mol m^{-3}
r	radial coordinate, m
r_c	radius of crystallite, m
R	gas constant, 8.314 J mol^{-1} K^{-1}
$S_{A/B}$	adsorption selectivity, dimensionless
t	time, s

T	absolute temperature, K
u	superficial gas velocity in packed bed, m s^{-1}
v	interstitial gas velocity in packed bed, m s^{-1}
y	gas phase mole fraction, dimensionless
z	distance along the adsorber, and along membrane layer, m

Greek letters

ε	voidage of packed bed, dimensionless
ν	exponent in dual-Langmuir-Freundlich isotherm, dimensionless
ρ	framework density, kg m^{-3}
τ	time, dimensionless

Subscripts

A	referring to site A
B	referring to site B
i	referring to component *i*
t	referring to total mixture

Table 1. 1-site Langmuir parameters for 20 different hypothetical MOFs examined for separation of A and B at 298 K. The saturation capacities of A and B are taken to equal each other. Also presented are mixed gas Langmuir calculations of selectivity and component loadings. The framework density of all MOFs ar taken to be equal to 1 kg L^{-1}.

	Langmuir parameters			Mixed-gas Lanmuir calculations for p_A=p_B=50 kPa; 298 K.			
HypMOF	q_{sat} mol kg^{-1}	b_A Pa^{-1}	b_B Pa^{-1}	Q_A mol L^{-1}	Q_B mol L^{-1}	ΔQ mol L^{-1}	$S_{A/B}$
1	2.5	0.0002	0.0001	1.563	0.781	0.781	2
2	2.5	0.0004	0.0001	1.923	0.481	1.442	4
3	2.5	0.0006	0.0001	2.083	0.347	1.736	6
4	2.5	0.0008	0.0001	2.174	0.272	1.902	8
5	2.5	0.002	0.0001	2.358	0.118	2.241	20
6	2.5	0.01	0.0001	2.470	0.025	2.446	100
7	2.5	0.001	0.0001	2.232	0.223	2.009	10
8	2.5	0.001	0.00001	2.427	0.024	2.403	100
9	2.5	0.001	0.000001	2.449	0.002	2.446	1000
10	2.5	0.001	1E-07	2.451	0.000	2.450	10000
11	5	0.00015	0.0001	2.777	1.852	0.926	1.5
12	5	0.0004	0.0001	3.846	0.962	2.885	4
13	5	0.0006	0.0001	4.167	0.694	3.472	6
14	5	0.0008	0.0001	4.348	0.543	3.804	8
15	5	0.002	0.0001	4.717	0.236	4.481	20
16	5	0.01	0.0001	4.941	0.049	4.891	100
17	5	0.001	0.0001	4.464	0.446	4.018	10
18	5	0.001	0.00001	4.854	0.049	4.806	100
19	5	0.001	0.000001	4.897	0.005	4.892	1000
20	5	0.001	1E-07	4.901	0.000	4.901	10000

Table 2. Breakthrough calculations for 20 different hypothetical HypMOFs. For the breakthrough simulations, the following parameter values were used: length of packed bed, L = 0.3 m; voidage of packed bed, ε = 0.4; superficial gas velocity at inlet, u = 0.04 m/s.

HypMOF	τ_{C2H4}	τ_{C2H2}	$\Delta\tau_{C2H2}$	A captured mol L^{-1}	B productivity mol L^{-1}
1	78.330	97.383	19.053	1.300	0.456
2	79.783	126.037	46.253	1.683	1.172
3	79.473	138.007	58.533	1.844	1.467
4	79.610	144.797	65.187	1.933	1.639
5	79.877	158.503	78.627	2.117	1.978
6	80.033	167.197	87.163	2.239	2.194
7	79.770	149.117	69.347	1.994	1.744
8	46.583	163.880	117.297	2.189	2.156
9	6.623	165.560	158.937	2.217	2.211
10	1.329	165.713	164.385	2.217	2.217
11	154.727	162.217	7.49	2.172	0.116
12	157.370	251.297	93.927	3.367	2.350
13	157.950	274.997	117.047	3.689	2.939
14	158.237	288.643	130.407	3.872	3.272
15	158.787	316.020	157.233	4.239	3.956
16	159.010	333.433	174.423	4.472	4.383
17	158.360	297.260	138.900	3.989	3.489
18	92.327	326.850	234.523	4.383	4.317
19	12.530	330.180	317.650	4.428	4.422
20	1.947	330.480	328.533	4.433	4.433

Table 3. Langmuir-Freundlich parameter fits for C_2H_4 and C_2H_6 in M-MOF-74 (M = Mg, Co, Fe, Mn, and Zn). The fit parameters were determined from the isotherm data reported by Geier et al. [27] at T = 313 K, 333 K, and 353 K. The Langmuir parameters are T-dependent, and were extrapolated to T = 298 K for use in the IAST and breakthrough calculations reported in this article.

$$q = q_{A,sat}\frac{b_A p^{\nu_A}}{1+b_A p^{\nu_A}} + q_{B,sat}\frac{b_B p^{\nu_B}}{1+b_B p^{\nu_B}}; \quad b_A = b_{A0}\exp\left(\frac{E_A}{RT}\right); \quad b_B = b_{B0}\exp\left(\frac{E_B}{RT}\right)$$

	Site A				Site B			
	$q_{A,sat}$ mol kg^{-1}	b_{A0} Pa$^{-\nu_A}$	E_A kJ mol^{-1}	ν_A	$q_{B,sat}$ mol kg^{-1}	b_{B0} Pa$^{-\nu_B}$	E_B kJ mol^{-1}	ν_B
Mg/C_2H_4	8.1	7.47E-11	23.5	1.06	6.1	1.04E-11	42	1
Mg/C_2H_6	6.2	3.64E-14	38	1.5	0.6	3.58E-09	27	1
Co/C_2H_4	3	4.64E-12	30.6	1.1	5.9	1.4E-11	43.6	1
Co/C_2H_6	5.6	1.77E-14	41.4	1.54	0.5	2.97E-08	22.9	1
Fe/C_2H_4	1.74	6.51E-12	38	1.12	4.9	4.16E-13	53	1.12
Fe/C_2H_6	8.42	4.47E-11	31	1.1				
Mn/C_2H_4	2.3	3.29E-10	21.2	1.1	6	1.17E-11	44.4	1
Mn/C_2H_6	6.3	1.22E-14	43	1.47	0.4	2.9E-09	29	1
Zn/C_2H_4	6	4.18E-19	74.5	1	6	3.43E-11	37.5	1
Zn/C_2H_6	5.6	6.62E-15	42.3	1.54	0.5	5.9E-09	26.3	1

Table 4. Data sources for isotherms of C_2H_4 and C_2H_6 in MOFs.

MOF	Surface area $m^2\ g^{-1}$	Pore volume $cm^3\ g^{-1}$	Framework density $kg\ m^{-3}$	Data sources for unary isotherm fits
NOTT-300	1370	0.433	1062	The isotherm fits are from Table S13 of Yang.[30] The data is for 293 K.
PAF-1-SO3Ag	1938	0.93	1070	[29]
MIL-101-Cr-SO_3Ag	1374	0.56	700	[28]

PAF-1-SO3Ag introduces π-complexation into highly porous PAF-122 with Ag(I) ions.[29]

MIL-101–Cr–SO_3Ag was afforded via Ag(I) ion exchange of the sulphonic acid functionalized MIL-101–Cr.[28]

NOTT-300 = $[Al_2(OH)_2(C_{16}O_8H_6)]$.[30, 43] It has 6.5 Å × 6.5 Å channels. The isotherm data are available at 293 K.[30]

Table 5. Langmuir-Freundlich parameter fits for C_3H_6 and C_3H_8 in M-MOF-74 (M = Mg, Co, Fe, Ni, Mn, and Zn). The fit parameters were determined from the isotherm data reported by Geier et al. [27] at T = 313 K, 333 K, and 353 K. The Langmuir parameters are T-dependent, and were extrapolated to T = 298 K for use in the IAST and breakthrough calculations reported in this article.

$$q = q_{A,sat}\frac{b_A p^{\nu_A}}{1+b_A p^{\nu_A}} + q_{B,sat}\frac{b_B p^{\nu_B}}{1+b_B p^{\nu_B}}; \quad b_A = b_{A0}\exp\left(\frac{E_A}{RT}\right); \quad b_B = b_{B0}\exp\left(\frac{E_B}{RT}\right)$$

	Site A				Site B			
	$q_{A,sat}$ mol kg^{-1}	b_{A0} Pa$^{-\nu_A}$	E_A kJ mol^{-1}	ν_A	$q_{B,sat}$ mol kg^{-1}	b_{B0} Pa$^{-\nu_B}$	E_B kJ mol^{-1}	ν_B
Mg/C_2H_4	5.5	3.53E-13	54.4	1.15	2.9	6.93E-11	36.6	0.9
Mg/C_2H_6	1.4	5.82E-27	100	2.8	4.9	1.38E-10	36	1
Co/C_2H_4	5.4	3.34E-15	68	1.34	1.8	6.24E-10	36	0.78
Co/C_2H_6	1.9	6.78E-27	106	2.8	3.9	9.03E-10	33.4	1
Fe/C_3H_6	5.3	1.42E-20	97	1.76	1.7	1.29E-10	33	1.13
Fe/C_3H_8	2.1	5.95E-12	48	0.83	4.3	6.15E-15	53	1.63
Ni/C_2H_4	4.9	1.19E-12	56	1.06	2.7	1.71E-09	34	0.74
Ni/C_2H_6	1.3	5.95E-27	107	2.65	4.4	4.68E-10	34	1
Mn/C_2H_4	5.8	1.43E-14	67	1.2	2.9	1.74E-08	26	0.7
Mn/C_2H_6	1.9	9.74E-27	105	2.8	3.9	9.03E-10	33.4	1
Zn/C_2H_4	5	2.49E-13	55	1.18	1.5	3.6E-15	62	1
Zn/C_2H_6	1.7	3.08E-28	108	2.9	3.8	4.17E-10	34	1

Table 6. 1-site Langmuir parameter fits for C_3H_6 and C_3H_8 in NbOFFIVE-1-Ni (= KAUST-7). The isotherm data for, were scanned from Figures 3B and S11 of Cadiau et al.[31]

KAUST-7	q_{sat} mol kg^{-1}	b_A Pa^{-1}
C_3H_6	2.1	2.6×10^{-5}
C_3H_8	3	2×10^{-7}

For 13X zeolite, and LTA-5A zeolite, the dual-site Langmuir isotherm fits for C_3H_6 and C_3H_8 are taken from Table 2 of Divekar et al.[63]

Table 7. Data sources for isotherms of CO_2 and CH_4 in MOFs, zeolites and AC.

MOF	Surface area $m^2\ g^{-1}$	Pore volume $cm^3\ g^{-1}$	Framework density $kg\ m^{-3}$	Data sources for unary isotherm fits
MgMOF-74	1669	0.607	909	[40, 64]
NiMOF-74	1532	0.582	1194	[35, 41]
NaX	950	0.280	1421	[42, 64]
CuBTC	2097	0.848	879	[64, 65]
Cu-TDPAT	1938	0.93	782	[51, 64]
Kureha carbon	1300	0.56	1860	[37]

MgMOF-74 (= Mg_2 (dobdc) = Mg\(dobdc) with dobdc = (dobdc4– = 1,4-dioxido-2,5-benzenedicarboxylate)). This MOF consists of one-dimensional hexagonal-shaped channels with free internal diameter of ca. 11 Å

NiMOF-74 = (Ni_2 (dobdc) = Ni\(dobdc) with dobdc = (dobdc4– = 1,4-dioxido-2,5-benzenedicarboxylate)). This MOF consists of one-dimensional hexagonal-shaped channels with free internal diameter of ca. 11 Å

NaX zeolite, also referred to as 13 X zeolite, has the FAU topology. The FAU topology consists of 785.7 $Å^3$ size cages separated by 7.4 Å size windows. Cage size is calculated on the basis of the equivalent sphere volume.

CuBTC (=$Cu_3(BTC)_2$ with BTC = 1,3,5-benzenetricarboxylate, also known as HKUST-1) structure consists of two types of "cages" and two types of "windows" separating these cages. Large cages are inter-connected by 9 Å windows of square cross-section. The large cages are also connected to tetrahedral-shaped pockets of ca. 6 Å size through triangular-shaped windows of ca. 4.6 Å size

Cu-TDPAT =an rht-type metal−organic framework; H_6TDPAT = 2,4,6-tris(3,5-dicarboxylphenylamino)-1,3,5-triazine.

Kureha carbon is a commercially available, purely microporous material ,with pore-size distribution centered at 0.6 and 1.1 nm.[37]

Table 8. Data sources for isotherms of CO_2 and N_2 in MOFs, zeolites and AC.

MOF	Surface area $m^2\ g^{-1}$	Pore volume $cm^3\ g^{-1}$	Framework density $kg\ m^{-3}$	Data sources for unary isotherm fits
MgMOF-74	1669	0.607	909	[40, 64]
NiMOF-74	1532	0.582	1194	[35, 41]
NaX	950	0.280	1421	[42, 64]
Kureha carbon	1300	0.56	1860	[37]
NOTT-300	1370	0.433	1062	[43]

MgMOF-74 (= Mg_2 (dobdc) = Mg\(dobdc) with dobdc = (dobdc4– = 1,4-dioxido-2,5-benzenedicarboxylate)), This MOF consists of one-dimensional hexagonal-shaped channels with free internal diameter of ca. 11 Å

NiMOF-74 = (Ni_2 (dobdc) = Ni\(dobdc) with dobdc = (dobdc4– = 1,4-dioxido-2,5-benzenedicarboxylate)). This MOF consists of one-dimensional hexagonal-shaped channels with free internal diameter of ca. 11 Å

NaX zeolite, also referred to as 13 X zeolite, has the FAU topology. The FAU topology consists of 785.7 $Å^3$ size cages separated by 7.4 Å size windows. Cage size is calculated on the basis of the equivalent sphere volume.

Kureha carbon is a commercially available, purely microporous material with pore-size distribution centered at 0.6 and 1.1 nm.[37]

NOTT-300 = $[Al_2(OH)_2(C_{16}O_8H_6)]$.[43] The pore dimensions are 6.5 Å × 6.5 Å.

Table 9. Data sources for isotherms of CO_2, CO, CH_4 and H_2 in MOFs, and zeolites. The data for MgMOF-74 and NaX are from Herm et al.[32] and Krishna and Long.[5] The data for MIL-101 are taken from Chowdhury et al.[66] The data for LTA-5A are from Pakseresht et al.[48] and Sircar and Golden.[44] The isotherm fits are convenient summarized in the Supporting Information accompanying the paper by Wu et al.[51]

MOF	Surface area $m^2\ g^{-1}$	Pore volume $cm^3\ g^{-1}$	Framework density $kg\ m^{-3}$	Data sources for unary isotherm fits
MgMOF-74	1669	0.607	909	[40, 64]
Cu-TDPAT	1938	0.93	782	[51, 64]
NaX zeolite	950	0.280	1421	[42, 64]
MIL-101	2674	1.38	440	[64, 67]
LTA-5A	900	0.25	1508	[51]
CuBTC	2097	0.848	879	[64, 67]

Cu-TDPAT =an rht-type metal−organic framework; H_6TDPAT = 2,4,6-tris(3,5-dicarboxylphenylamino)-1,3,5-triazine.

CuBTC (=$Cu_3(BTC)_2$ with BTC = 1,3,5-benzenetricarboxylate, also known as HKUST-1) structure consists of two types of "cages" and two types of "windows" separating these cages. Large cages are inter-connected by 9 Å windows of square cross-section. The large cages are also connected to tetrahedral-shaped pockets of ca. 6 Å size through triangular-shaped windows of ca. 4.6 Å size.

NaX zeolite (=13X), also referred to as 13 X zeolite, has the FAU topology. The FAU topology consists of 785.7 $Å^3$ size cages separated by 7.4 Å size windows. Cage size is calculated on the basis of the equivalent sphere volume.

LTA-5A consists of 743.05 $Å^3$ size cages separated by 4 Å windows.

Table 10. Dual-Langmuir parameter fits of CBMC simulations at 433 K of pure component alkane isotherms in $Fe_2(BDP)_3$. The fits are reported in the Supplementary Material accompanying the paper by Krishna and van Baten.[54]

$q_i = q_{A,sat}\frac{b_A f}{1+b_A f} + q_{B,sat}\frac{b_B f}{1+b_B f}$	Site A		Site B	
	$q_{A,sat}$ mol/kg	b_A Pa^{-1}	$q_{B,sat}$ mol/kg	b_B Pa^{-1}
nC5	2.0	1.23×10^{-3}	0.7	6.08×10^{-7}
2MB	2.9	1.75×10^{-5}		
neoP	2.8	6.28×10^{-8}		
nC6	1.6	5.9×10^{-3}	0.4	6.26×10^{-5}
2MP	2.1	8.35×10^{-5}		
3MP	2	6.96×10^{-5}		
22DMB	2.75	1.72×10^{-7}		
23DMB	2.75	7.5×10^{-8}		
nC7	1.38	3.93×10^{-2}		
2MH	1.8	5.77×10^{-4}		
3MH	1.85	1.44×10^{-4}		
22DMP	2	4.94×10^{-7}		
23DMP	2	3.24×10^{-7}		

Table 11. Dual-site Langmuir-Freundlich parameters for pure component pentane and hexane isomers at 433 K in MFI zeolite. The fits are based on CBMC simulation data of Krishna and van Baten.[68]

$\Theta = \Theta_{A,sat} \frac{b_A f^{\nu_A}}{1+b_A f^{\nu_A}} + \Theta_{B,sat} \frac{b_B f^{\nu_B}}{1+b_B f^{\nu_B}}$	Site A			Site B		
	$\Theta_{A,sat}$ molecules uc^{-1}	b_A Pa$^{-\nu_A}$	ν_A dimensionless	$\Theta_{B,sat}$ molecules uc^{-1}	b_B Pa$^{-\nu_B}$	ν_B dimensionless
nC5	4	6.26×10^{-6}	1.12	4	1.94×10^{-4}	1
2MB	4	1.69×10^{-4}	1	2	4.93×10^{-7}	1
Neo-pentane	4	1.24×10^{-4}	1			
nC6	3.2	2.21×10^{-8}	1.6	4.3	7.42×10^{-4}	1
2MP	4	7.85×10^{-4}	1.03			
3MP	4	4.22×10^{-4}	1.02	1	9.88×10^{-7}	1
22DMB	4	2.55×10^{-4}	1.02			
23DMB	4	4.59×10^{-4}	1.02			

Table 12. Langmuir parameter fits for nC5 and 2MB in ZIF-8. The fits are based on experimental isotherm data of Zhang et al.[52] measured at 308 K, 343 K and 373 K. The experimental data were scanned from Figures 6 and 7 of Zhang et al.[52]

$q = q_{sat}\frac{bp}{1+bp};$ $b = b_0 \exp\left(\frac{E}{RT}\right)$	q_{sat} mol kg^{-1}	b_0 Pa^{-1}	E kJ mol^{-1}
nC5	3.5	6.5×10^{-11}	45
2MB	2.2	8×10^{-10}	35.4

Table 13. Dual-site Langmuir parameters for pure component butane, pentane, hexane, and heptane isomers at 433 K in ZIF-77. The fits are based on the CBMC simulations of Dubbeldam et al.[56]

$q = q_{A,sat}\frac{b_A f}{1+b_A f} + q_{B,sat}\frac{b_B f}{1+b_B f}$	Site A		Site B	
	$q_{A,sat}$ mol/kg	b_A Pa^{-1}	$q_{B,sat}$ mol/kg	b_B Pa^{-1}
nC4	0.91	5.75×10^{-5}	0.81	1.33×10^{-6}
iC4	0.92	1.63×10^{-5}	1.14	3.09×10^{-7}
nC5	0.87	1.82×10^{-4}	0.66	1.87×10^{-6}
2MB	0.8	2.0×10^{-5}	0.6	2.0×10^{-7}
DMP	0.7	6.23×10^{-8}		
nC6	0.81	5.25×10^{-4}	0.59	2.24×10^{-6}
2MP	0.92	4.95×10^{-5}	0.43	1.66×10^{-8}
3MP	0.8	2.15×10^{-5}	0.4	5.15×10^{-8}
22DMB	0.7	2.1×10^{-8}		
23DMB	0.96	6.31×10^{-7}	0.2	3.65×10^{-9}
nC7	0.74	1.72×10^{-3}	0.49	1.69×10^{-6}
2MH	0.8	1.02×10^{-4}	0.27	9.35×10^{-7}
3MH	0.77	5.62×10^{-5}	0.26	1.86×10^{-7}
22DMP	0.71	4.0×10^{-8}	1.1	6.47×10^{-12}
23DMP	0.74	1.38×10^{-6}		

Table 14. Dual-site Langmuir-Freundlich parameters for pure component hexane isomers at 433 K in Co(BDP). The fits are based on CBMC simulation data of Krishna and van Baten.[68]

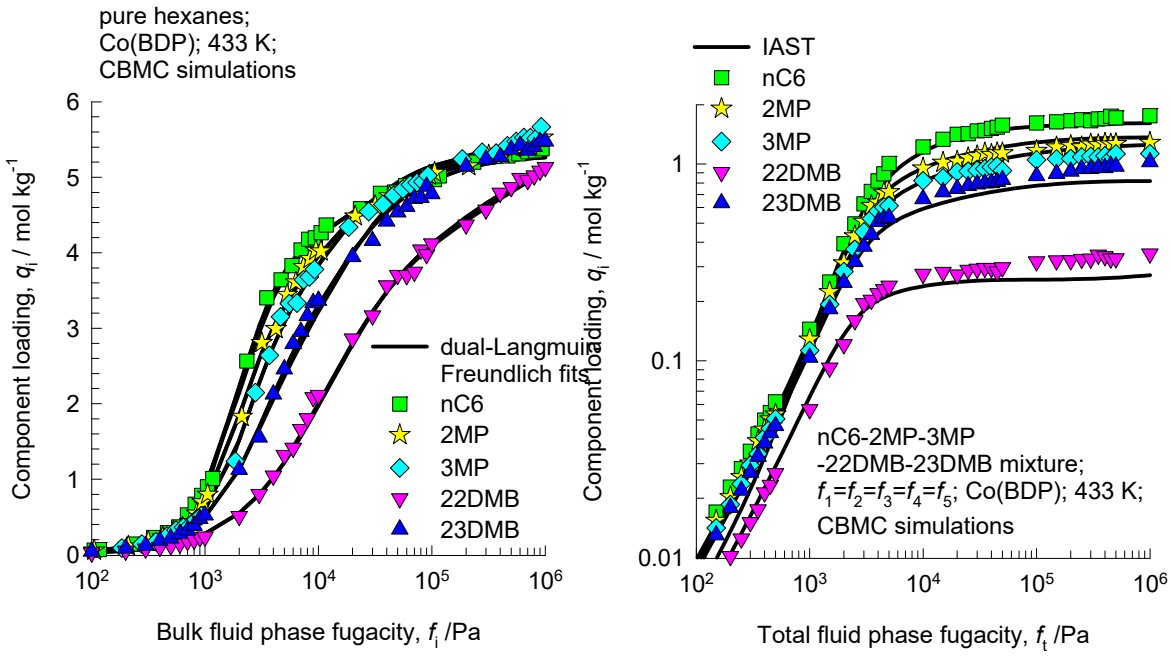

	Site A			Site B		
	$q_{i,A,sat}$ mol kg^{-1}	$b_{i,A}$ Pa$^{-\nu_i}$	$\nu_{i,A}$ dimensionless	$q_{i,B,sat}$ mol kg^{-1}	$b_{i,B}$ Pa$^{-\nu_i}$	$\nu_{i,B}$ dimensionless
nC6	1.7	3.65×10^{-4}	0.8	3.7	6.29×10^{-8}	2.2
2MP	3.3	1.49×10^{-4}	1	2	6.77×10^{-10}	2.8
3MP	3.5	1.3×10^{-4}	1	1.9	8.82×10^{-10}	2.7
22DMB	1.8	5.14×10^{-5}	0.74	4.1	3.42×10^{-5}	1.1
23DMB	4	1.07×10^{-4}	1	1.3	1.24×10^{-8}	2.3

Table 15. Dual-site Langmuir-Freundlich parameters for pure component hexane isomers at 433 K in MgMOF-74. The fits are based on CBMC simulation data of Krishna and van Baten.[68]

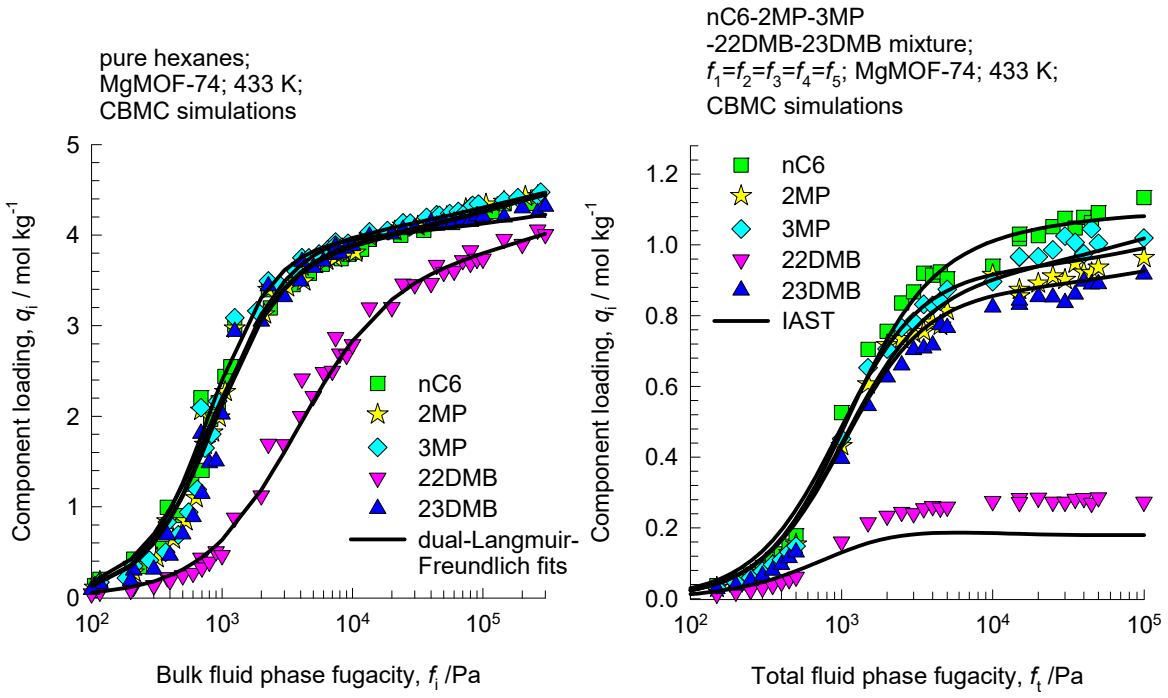

	Site A			Site B		
	$q_{i,A,sat}$ mol kg^{-1}	$b_{i,A}$ Pa$^{-\nu_i}$	$\nu_{i,A}$ dimensionless	$q_{i,B,sat}$ mol kg^{-1}	$b_{i,B}$ Pa$^{-\nu_i}$	$\nu_{i,B}$ dimensionless
nC6	3.95	1.98×10^{-5}	1.66	1.1	1.41×10^{-3}	0.5
2MP	3.84	1.85×10^{-5}	1.66	1.2	1.39×10^{-3}	0.52
3MP	3.95	1.81×10^{-5}	1.66	1.1	1.43×10^{-3}	0.5
22DMB	3.5	4×10^{-5}	1.3	1.2	5×10^{-4}	0.6
23DMB	3.9	9.94×10^{-6}	1.73	1.04	1.57×10^{-3}	0.45

Table 16. Dual-site Langmuir-Freundlich parameters for pure component hexane isomers at 433 K in ZnMOF-74. The fits are based on CBMC simulation data of Krishna and van Baten.[68]

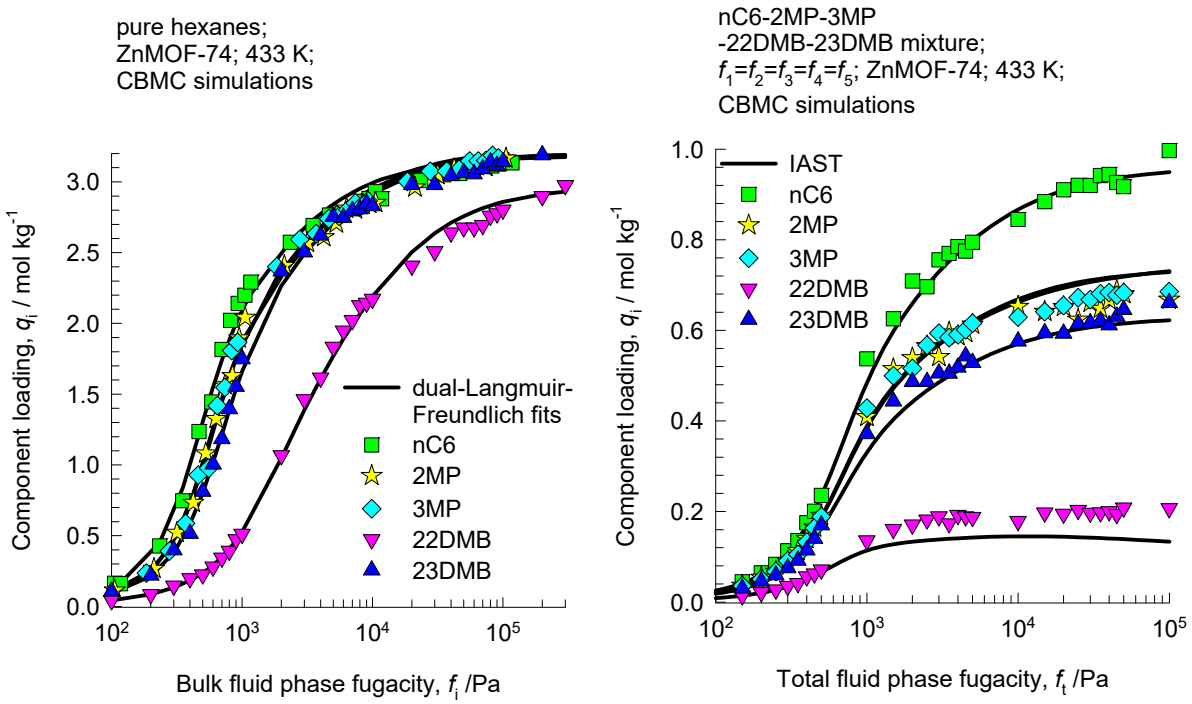

	Site A			Site B		
	$q_{i,A,sat}$ mol kg^{-1}	$b_{i,A}$ Pa$^{-\nu_i}$	$\nu_{i,A}$ dimensionless	$q_{i,B,sat}$ mol kg^{-1}	$b_{i,B}$ Pa$^{-\nu_i}$	$\nu_{i,B}$ dimensionless
nC6	1.6	6.05×10^{-8}	2.7	1.6	7.57×10^{-4}	1
2MP	1.4	6.31×10^{-9}	3	1.83	5.54×10^{-4}	1
3MP	1.5	1.88×10^{-8}	2.8	1.7	5.81×10^{-4}	1
22DMB	0.77	7.53×10^{-8}	2.2	2.2	1.88×10^{-4}	1
23DMB	1.5	4.25×10^{-8}	2.6	1.7	5.04×10^{-4}	1

Table 17. Dual-site Langmuir-Freundlich parameters for pure component hexane isomers at 433 K in ZIF-8. The fits are based on the CBMC simulations of Dubbeldam et al.[56]

(a) Pure components

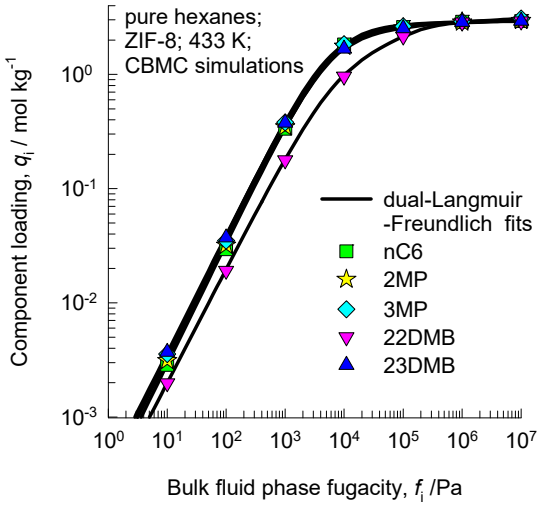

(b) 5-component mixture

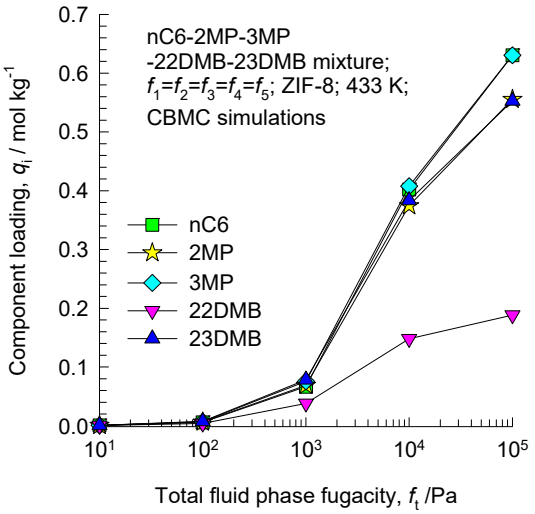

	Site A			Site B		
	$q_{i,A,sat}$ mol kg^{-1}	$b_{i,A}$ Pa$^{-\nu_{iA}}$	$\nu_{i,A}$ dimensionless	$q_{i,B,sat}$ mol kg^{-1}	$b_{i,B}$ Pa$^{-\nu_{iA}}$	$\nu_{i,B}$ dimensionless
nC6	2.8	8.53×10^{-5}	1.07	0.44	5.59×10^{-5}	0.59
2MP	2.8	1.06×10^{-4}	1.04	1.0	8.08×10^{-6}	0.64
3MP	2.8	9.81×10^{-5}	1.07	1.2	2.98×10^{-5}	0.58
22DMB	1.82	1.09×10^{-4}	1.0	1.1	1.55×10^{-7}	1.34
23DMB	2.4	1.18×10^{-4}	1.06	0.6	1.11×10^{-4}	0.76

Table 18. Dual-site Langmuir-Freundlich parameters for pure component hexane isomers at 433 K in BEA zeolite. The fits are based on the isotherm data of Bárcia et al.[69]

	Site A			Site B		
	$q_{i,A,sat}$ mol kg^{-1}	$b_{i,A}$ Pa$^{-\nu_{iA}}$	$\nu_{i,A}$ dimensionless	$q_{i,B,sat}$ mol kg^{-1}	$b_{i,B}$ Pa$^{-\nu_{iA}}$	$\nu_{i,B}$ dimensionless
nC6	0.32	2.43×10^{-6}	1.36	0.6	1.04×10^{-2}	0.8
3MP	0.44	6.97×10^{-5}	1	0.51	1.13×10^{-3}	1
22DMB	0.31	6.18×10^{-4}	0.85	0.67	2.63×10^{-5}	1.13
23DMB	0.44	1.51×10^{-4}	1	0.47	2.37×10^{-4}	1

Table 19. Dual-site Langmuir-Freundlich parameters for pure component hexane isomers at 433 K in Zn(bdc)(dabco)$_{0.5}$. The fits are based on the CBMC simulations of Dubbeldam et al.[56]

	Site A			Site B		
	$q_{i,A,sat}$ mol kg^{-1}	$b_{i,A}$ Pa$^{-\nu_{iA}}$	$\nu_{i,A}$ dimensionless	$q_{i,B,sat}$ mol kg^{-1}	$b_{i,B}$ Pa$^{-\nu_{iA}}$	$\nu_{i,B}$ dimensionless
nC6	0.75	3.56×10^{-11}	2	3.8	2.21×10^{-4}	1.03
2MP	1.3	1.47×10^{-7}	1.3	3.4	3.07×10^{-4}	1.04
3MP	1.4	4.38×10^{-7}	1.24	3.3	3.83×10^{-4}	1.04
22DMB	0.4	2.36×10^{-9}	1.5	2.8	2.89×10^{-4}	1.03
23DMB	2.9	9.91×10^{-5}	0.62	2.9	4.19×10^{-4}	1.07

Table 20. Dual-site Langmuir-Freundlich parameters for pure component hexane isomers at 433 K in UiO-66. The fits are based on the CBMC simulations of Dubbeldam et al.[56]

	Site A			Site B		
	$q_{i,A,sat}$ mol kg^{-1}	$b_{i,A}$ Pa$^{-\nu_{i,A}}$	$\nu_{i,A}$ dimensionless	$q_{i,B,sat}$ mol kg^{-1}	$b_{i,B}$ Pa$^{-\nu_{i,A}}$	$\nu_{i,B}$ dimensionless
nC6	1.82	3.63×10^{-4}	1			
2MP	1.56	2.72×10^{-3}	1	0.28	1.57×10^{-4}	1
3MP	1.45	1.1×10^{-2}	1	0.4	2.44×10^{-4}	1
22DMB	1.35	2.67×10^{-2}	1	0.49	3.87×10^{-4}	1
23DMB	1.33	7.14×10^{-2}	1	0.52	9.11×10^{-4}	1

Table 21. Dual-site Langmuir-Freundlich parameters for pure component hexane isomers at 433 K in CFI. The fits are based on the CBMC simulations of Dubbeldam et al.[56]

	Site A			Site B		
	$q_{i,A,sat}$ mol kg^{-1}	$b_{i,A}$ Pa$^{-\nu_{iA}}$	$\nu_{i,A}$ dimensionless	$q_{i,B,sat}$ mol kg^{-1}	$b_{i,B}$ Pa$^{-\nu_{iA}}$	$\nu_{i,B}$ dimensionless
nC6	0.25	2.92×10^{-8}	1	0.59	3.41×10^{-4}	1
2MP	0.22	5.07×10^{-7}	1	0.61	7.71×10^{-4}	1
3MP	0.18	7.59×10^{-6}	1	0.65	8.03×10^{-4}	1
22DMB	0.11	2.65×10^{-5}	1	0.73	1.02×10^{-3}	1
23DMB	0.83	1.96×10^{-3}	1			

Table 22. Dual-site Langmuir-Freundlich parameters for pure component hexane isomers at 433 K in ATS. The fits are based on the CBMC simulations of Dubbeldam et al.[56]

	Site A			Site B		
	$q_{i,A,sat}$ mol kg^{-1}	$b_{i,A}$ Pa$^{-\nu_{iA}}$	$\nu_{i,A}$ dimensionless	$q_{i,B,sat}$ mol kg^{-1}	$b_{i,B}$ Pa$^{-\nu_{iA}}$	$\nu_{i,B}$ dimensionless
nC6	0.82	2.21×10^{-4}	1	0.54	9.78×10^{-7}	1
2MP	0.95	3.82×10^{-4}	1	0.37	6.41×10^{-7}	1
3MP	0.98	3.17×10^{-4}	1	0.285	4.34×10^{-7}	1
22DMB	1.03	2.57×10^{-4}	1	0.18	1.1×10^{-7}	1
23DMB	1.03	5.91×10^{-4}	1	0.2	3.11×10^{-7}	1

Table 23. Unary isotherm data sources for evaluation of the separation of xylene isomers.

MOF	Surface area $m^2\ g^{-1}$	Pore volume $cm^3\ g^{-1}$	Framework density $kg\ m^{-3}$	Data sources for unary isotherm fits
MAF-X8	1465	0.5184	954.29	CBMC simulated isotherms at 433 K.[58]
BaX zeolite			1480	Experimental data at 393 K and 453 K.[70, 71]
DynaMOF-100		0.626	1105	Experimental data on pure component isotherms at 298 K.[60]
Co(BDP)	2244	0.9053	721.88	CBMC simulated isotherms at 433 K.[58]
JUC-77	1098	0.4181	1144.03	CBMC simulated isotherms at 433 K.[58]
MIL-125	2231	0.7542	822.47	CBMC simulated isotherms at 433 K.[58]
MIL-125-NH_2	2231	0.6872	861.6	CBMC simulated isotherms at 433 K.[58]

MAF-X8 is a Zn(II) pyrazolate-carboxylate framework whose synthesis has been reported by He et al. [72] Within the one-dimensional 10 Å channels of MAF-X8, we have commensurate stacking of p-xylene.[58]

BaX is a cation-exchanged Faujasite zeolite. The FAU topology consists of 785.7 Å3 size cages separated by 7.4 Å size windows. Cage size is calculated on the basis of the equivalent sphere volume. The data plotted in the Figures are for 393 K.

DynaMOF-100 consists of a Zn(II)-based dynamic coordination framework, [Zn4O(L)3] where the ligand L = 4, 4'- ((4-(tert-butyl) - 1,2- phenylene)bis(oxy))dibenzoate)

Table 24. Unary isotherm data sources for evaluation of ethylbenzene/styrene separations.

MOF	Surface area $m^2\ g^{-1}$	Pore volume $cm^3\ g^{-1}$	Framework density $kg\ m^{-3}$	Data sources for unary isotherm fits	Comment
MIL-47(V)			1004	Experimental data at 298 K.[62] The original experiment data has been refitted; these parameters are used.[60]	The original experiment data has been refitted; [60] these parameters are used.
MIL-53(Al)			1041		
DynaMOF-100		0.626	1105	Experimental data on pure component isotherms at 298 K.[60]	

DynaMOF-100 consists of a Zn(II)-based dynamic coordination framework, [Zn4O(L)3] where the ligand L = 4, 4'- ((4-(tert-butyl) - 1,2- phenylene)bis(oxy))dibenzoate)

MIL-47 has one-dimensional diamond-shaped channels with free internal diameter of ca 8.5 Å

MIL-53 has one-dimensional diamond-shaped channels with free internal diameter of ca 8.5 Å

23. References

(1) Krishna, R. The Maxwell-Stefan Description of Mixture Diffusion in Nanoporous Crystalline Materials. *Microporous Mesoporous Mater.* **2014**, *185*, 30-50.

(2) Krishna, R. Methodologies for Evaluation of Metal-Organic Frameworks in Separation Applications. *RSC Adv.* **2015**, *5*, 52269-52295.

(3) Krishna, R.; Baur, R. Modelling Issues in Zeolite Based Separation Processes. *Sep. Purif. Technol.* **2003**, *33*, 213-254.

(4) Myers, A. L.; Prausnitz, J. M. Thermodynamics of Mixed Gas Adsorption. *A.I.Ch.E.J.* **1965**, *11*, 121-130.

(5) Krishna, R.; Long, J. R. Screening metal-organic frameworks by analysis of transient breakthrough of gas mixtures in a fixed bed adsorber. *J. Phys. Chem. C* **2011**, *115*, 12941-12950.

(6) Kluge, G.; Franke, T.; Schöllner, R.; Nagel, G. Estimation of Component Loadings in Fixed-Bed Adsorption from Breakthrough Curves of Binary Gas Mixtures in Nontrace Systems. *Chem. Eng. Sci.* **1991**, *46*, 368-371.

(7) Malek, A.; Farooq, S. Effect of Velocity Variation on Equilibrium Calculations from Multicomponent Breakthrough Experiments, 1997.

(8) Banerjee, D.; Cairns, A. J.; Liu, J.; Krishna, R.; Thallapally, P. K.; Strachan, D. M. Potential of Metal-Organic Frameworks for Capture of Noble Gases. *Acc. Chem. Res.* **2015**, *48*, 211-219.

(9) Liu, J.; Thallapally, P. K.; Strachan, D. Metal−Organic Frameworks for Removal of Xe and Kr from Nuclear Fuel Reprocessing Plants. *Langmuir* **2012**, *28*, 11584-11589.

(10) Liu, J.; Strachan, D. M.; Thallapally, P. K. Enhanced noble gas adsorption in Ag@MOF-74Ni. *Chem. Commun.* **2014**, *50*, 466-468.

(11) Gurdal, Y.; Keskin, S. Atomically Detailed Modeling of Metal Organic Frameworks for Adsorption, Diffusion, and Separation of Noble Gas Mixtures. *Ind. Eng. Chem. Res.* **2012**, *51*, 7373-8382.

(12) Chen, X.; Plonka, A. M.; Banerjee, D.; Krishna, R.; Schaef, H. T.; Ghose, D.; Thallapally, P. K.; Parise, J. B. Direct Observation of Xe and Kr Adsorption in a Xe-selective Microporous Metal Organic Framework. *J. Am. Chem. Soc.* **2015**, *137*, 7007-7010.

(13) Wang, H.; Yao, K.; Zhang, Z.; Jagiello, J.; Gong, Q.; Han, Y.; Li, J. The First Example of Commensurate Adsorption of Atomic Gas in a MOF and Effective Separation of Xenon from Other Noble Gases. *Chem. Sci.* **2014**, *5*, 620-624.

(14) Feng, X.; Zong, Z.; Elsaidi, S.; Jasinski, J. B.; Krishna, R.; Thallapally, P. K.; Carreon, M. A. Kr/Xe Separation over a Chabazite Zeolite Membrane *J. Am. Chem. Soc.* **2016**, *138*, 9791-9794.

(15) Krishna, R. Describing the Diffusion of Guest Molecules inside Porous Structures. *J. Phys. Chem. C* **2009**, *113*, 19756-19781.

(16) Krishna, R.; van Baten, J. M. A molecular simulation study of commensurate – incommensurate adsorption of n-alkanes in cobalt formate frameworks. *Molecular Simulation* **2009**, *35*, 1098-1104.

(17) Matsuda, R.; Kitaura, R.; Kitagawa, S.; Kubota, Y.; Belosludov, R. V.; Kobayashi, T. C.; Sakamoto, H.; Chiba, T.; Takata, M.; Kawazoe, Y.; Mita, Y. Highly controlled acetylene accommodation in a metal–organic microporous material. *Nature* **2005**, *436*, 238-241.

(18) Fischer, M.; Hoffmann, F.; Fröba, M. New Microporous Materials for Acetylene Storage and C_2H_2/CO_2 Separation: Insights from Molecular Simulations. *ChemPhysChem* **2010**, *11*, 2220-2229.

(19) Li, P.; He, Y.; Zhao, Y.; Weng, L.; Wang, H.; Krishna, R.; Wu, H.; Zhou, W.; O'Keeffe, M.; Han, Y.; Chen, B. A Rod-Packing Microporous Hydrogen-Bonded Organic Framework for Highly Selective Separation of C_2H_2/CO_2 at Room Temperature. *Angew. Chem. Int. Ed.* **2015**, *54*, 574-577.

(20) Duan, X.; Zhang, Q.; Cai, J.; Yang, Y.; Cui, Y.; He, Y.; Wu, C.; Krishna, R.; Chen, B.; Qian, G. A New Metal–Organic Framework with Potential for Adsorptive Separation of Methane from Carbon Dioxide, Acetylene, Ethylene, and Ethane Established by Simulated Breakthrough Experiments. *J. Mater. Chem. A* **2014**, *2*, 2628-2633.

(21) Duan, J.; Jin, W.; Krishna, R. Natural Gas Purification Using a Porous Coordination Polymer with Water and Chemical Stability. *Inorg. Chem.* **2015**, *54*, 4279-4284.

(22) Luo, F.; Yan, C.; Dang, L.; Krishna, R.; Zhou, W.; Wu, H.; Dong, X.; Han, Y.; Hu, T.-L.; O'Keeffe, M.; Wang, L.; Luo, M.; Lin, R.-B.; Chen, B. UTSA-74: A MOF-74 Isomer with Two Accessible Binding Sites per Metal Center for Highly Selective Gas Separation. *J. Am. Chem. Soc.* **2016**, *138*, 5678-5684.

(23) Cui, X.; Chen, K.; Xing, H.; Yang, Q.; Krishna, R.; Bao, Z.; Wu, H.; Zhou, W.; Dong, X.; Han, Y.; Li, B.; Ren, Q.; Zaworotko, M. J.; Chen, B. Pore Chemistry and Size Control in Hybrid Porous Materials for Acetylene Capture from Ethylene. *Science* **2016**, *353*, 141-144.

(24) Bae, Y.-S.; Lee, C. Y.; Kim, K. C.; Farha, O. K.; Nickias, P.; Hupp, J. T.; Nguyen, S. T.; Snurr, R. Q. High Propene/Propane Selectivity in Isostructural Metal–Organic Frameworks with High Densities of Open Metal Sites. *Angew. Chem. Int. Ed.* **2012**, *51*, 1857-1860.

(25) Bao, Z.; Alnemrat, S.; Vasiliev, I.; Ren, Q.; Yu, L.; Lu, X.; Deng, S. Adsorption of Ethane, Ethylene, Propane and Propylene on a Magnesium-Based Metal-Organic Framework. *Langmuir* **2011**, *27*, 13554-13562.

(26) Bloch, E. D.; Queen, W. L.; Krishna, R.; Zadrozny, J. M.; Brown, C. M.; Long, J. R. Hydrocarbon Separations in a Metal-Organic Framework with Open Iron(II) Coordination Sites. *Science* **2012**, *335*, 1606-1610.

(27) Geier, S. J.; Mason, J. A.; Bloch, E. D.; Queen, W. L.; Hudson, M. R.; Brown, C. M.; Long, J. R. Selective adsorption of ethylene over ethane and propylene over propane in the metal–organic frameworks M_2(dobdc) (M = Mg, Mn, Fe, Co, Ni, Zn). *Chem. Sci.* **2013**, *4*, 2054-2061.

(28) Zhang, Y.; Li, B.; Krishna, R.; Wu, Z.; Ma, D.; Shi, Z.; Pham, T.; Forrest, K.; Space, B.; Ma, S. Highly Selective Adsorption of Ethylene over Ethane in a MOF Featuring the Combination of Open Metal Site and π-Complexation. *Chem. Commun.* **2015**, *51*, 2714-2717.

(29) Li, B.; Zhang, Y.; Krishna, R.; Yao, K.; Han, Y.; Wu, Z.; Ma, D.; Shi, Z.; Pham, T.; Space, B.; Liu, J.; Thallapally, P. K.; Liu, J.; Chrzanowski, M.; Ma, S. Introduction of Π-Complexation into Porous Aromatic Framework for Highly Selective Adsorption of Ethylene over Ethane. *J. Am. Chem. Soc.* **2014**, *136*, 8654-8660.

(30) Yang, S.; Ramirez-Cuesta, A. J.; Newby, R.; Garcia-Sakai, V.; Manuel, P.; Callear, S. K.; Campbell, S. I.; Tang, C. C.; Schröder, M. Supramolecular binding and separation of hydrocarbons within a functionalized porous metal–organic framework. *Nature Chemistry* **2014**, *7*, 121-129.

(31) Cadiau, A.; Adil, K.; Bhatt, P. M.; Belmabkhout, Y.; Eddaoudi, M. A Metal-Organic Framework–Based Splitter for Separating Propylene from Propane. *Science* **2016**, *353*, 137-140.

(32) Herm, Z. R.; Swisher, J. A.; Smit, B.; Krishna, R.; Long, J. R. Metal-Organic Frameworks as Adsorbents for Hydrogen Purification and Pre-Combustion Carbon Dioxide Capture *J. Am. Chem. Soc.* **2011**, *133*, 5664-5667.

(33) Rochelle, G. T. Amine Scrubbing for CO_2 Capture. *Science* **2009**, *325*, 1652-1654.

(34) Wu, H.; Simmons, J. M.; Srinivas, G.; Zhou, W.; Yildrim, T. Adsorption Sites and Binding Nature of CO_2 in Prototypical Metal-Organic Frameworks: A Combined Neutron Diffraction and First-Principles Study. *J. Phys. Chem. Lett.* **2010**, *1*, 1946-1951.

(35) Krishna, R.; van Baten, J. M. Investigating the Relative Influences of Molecular Dimensions and Binding Energies on Diffusivities of Guest Species Inside Nanoporous Crystalline Materials *J. Phys. Chem. C* **2012**, *116*, 23556-23568.

(36) Kong, X.; Scott, E.; Ding, W.; Mason, J. A.; Long, J. R.; Reimer, J. A. CO_2 Dynamics in a Metal−Organic Framework with Open Metal Sites. *J. Am. Chem. Soc.* **2012**, *134*, 14341-14344.

(37) Yu, H.; Wang, X.; Xu, C.; Chen, D.-L.; Zhu, W.; Krishna, R. Utilizing transient breakthroughs for evaluating the potential of Kureha carbon for CO_2 capture. *Chem. Eng. J.* **2015**, *269*, 135-147.

(38) Li, L.; Yang, J.; Li, J.; Chen, Y.; Li, J. Separation of CO_2/CH_4 and CH_4/N_2 Mixtures by M/DOBDC: a Detailed Dynamic Comparison with MIL-100(Cr) and Activated Carbon. *Microporous Mesoporous Mater.* **2014**, *198*, 236-246.

(39) Chen, D.-L.; Shang, H.; Zhu, W.; Krishna, R. Transient Breakthroughs of CO_2/CH_4 and C_3H_6/C_3H_8 Mixtures in Fixed Beds packed with Ni-MOF-74. *Chem. Eng. Sci.* **2014**, *117*, 407-415.

(40) Mason, J. A.; Sumida, K.; Herm, Z. R.; Krishna, R.; Long, J. R. Evaluating Metal-Organic Frameworks for Post-Combustion Carbon Dioxide Capture via Temperature Swing Adsorption. *Energy Environ. Sci.* **2011**, *4*, 3030-3040.

(41) Dietzel, P. D. C.; Besikiotis, V.; Blom, R. Application of metal–organic frameworks with coordinatively unsaturated metal sites in storage and separation of methane and carbon dioxide. *J. Mater. Chem.* **2009**, *19*, 7362-7370.

(42) Belmabkhout, Y.; Pirngruber, G.; Jolimaitre, E.; Methivier, A. A complete experimental approach for synthesis gas separation studies using static gravimetric and column breakthrough experiments. *Adsorption* **2007**, *13*, 341-349.

(43) Yang, S.; Sun, J.; Ramirez-Cuesta, A. J.; Callear, S. K.; David, W. I. F.; Anderson, D. P.; Newby, R.; Blake, A. J.; Parker, J. E.; Tang, C. C.; Schröder, M. Selectivity and direct visualization of carbon dioxide and sulfur dioxide in a decorated porous host. *Nature Chemistry* **2012**, *4*, 887-894.

(44) Sircar, S.; Golden, T. C. Purification of Hydrogen by Pressure Swing Adsorption. *Separ. Sci. Technol.* **2000**, *35*, 667-687.

(45) Ribeiro, A. M.; Grande, C. A.; Lopes, F. V. S.; Loureiro, J. M.; Rodrigues, A. E. A parametric study of layered bed PSA for hydrogen purification. *Chem. Eng. Sci.* **2008**, *63*, 5258-5273.

(46) Banu, A. M.; Friedrich, D.; Brandani, S.; Düren, T. A Multiscale Study of MOFs as Adsorbents in H_2 PSA Purification. *Ind. Eng. Chem. Res.* **2013**, *52*, 9946-9957.

(47) Majlan, E. H.; Daud, W. R. W.; Iyuke, S. E.; Mohamad, A. B.; Kadhum, A. H.; Mohammad, A. W.; Takriff, M. S.; Bahaman, N. Hydrogen purification using compact pressure swing adsorption system for fuel cell. *Int. J. Hydrogen Energy* **2009**, *34*, 2771-2777.

(48) Pakseresht, S.; Kazemeini, M.; Akbarnejad, M. M. Equilibrium isotherms for CO, CO_2, CH_4 and C_2H_4 on the 5A molecular sieve by a simple volumetric apparatus. *Sep. Purif. Technol.* **2002**, *28*, 53-60.

(49) Sircar, S. Basic research needs for design of adsorptive gas separation processes *Ind. Eng. Chem. Res.* **2006**, *45*, 5435-5448.

(50) Herm, Z. R.; Krishna, R.; Long, J. R. CO_2/CH_4, CH_4/H_2 and $CO_2/CH_4/H_2$ separations at high pressures using Mg_2(dobdc). *Microporous Mesoporous Mater.* **2012**, *151*, 481-487.

(51) Wu, H.; Yao, K.; Zhu, Y.; Li, B.; Shi, Z.; Krishna, R.; Li, J. Cu-TDPAT, an *rht*-type Dual-Functional Metal–Organic Framework Offering Significant Potential for Use in H_2 and Natural Gas Purification Processes Operating at High Pressures. *J. Phys. Chem. C* **2012**, *116*, 16609-16618.

(52) Zhang, L.; Qian, G.; Liu, Z.; Cui, Q.; Wang, h.; Yao., H. Adsorption and Separation Properties of N-pentane/Isopentane on ZIF-8. *Sep. Purif. Technol.* **2015**, *156*, 472-479.

(53) Herm, Z. R.; Wiers, B. M.; Van Baten, J. M.; Hudson, M. R.; Zajdel, P.; Brown, C. M.; Maschiocchi, N.; Krishna, R.; Long, J. R. Separation of Hexane Isomers in a Metal-Organic Framework with Triangular Channels *Science* **2013**, *340*, 960-964.

(54) Krishna, R.; van Baten, J. M. Screening Metal-Organic Frameworks for Separation of Pentane Isomers. *Phys. Chem. Chem. Phys.* **2017**, *19*, 8380-8387.

(55) Krishna, R.; van Baten, J. M. Screening of zeolite adsorbents for separation of hexane isomers: A molecular simulation study. *Sep. Purif. Technol.* **2007**, *55*, 246-255.

(56) Dubbeldam, D.; Krishna, R.; Calero, S.; Yazaydın, A. Ö. Computer-Assisted Screening of Ordered Crystalline Nanoporous Adsorbents for Separation of Alkane Isomers. *Angew. Chem. Int. Ed.* **2012**, *51*, 11867-11871.

(57) Krishna, R. Separating Mixtures by Exploiting Molecular Packing Effects in Microporous Materials. *Phys. Chem. Chem. Phys.* **2015**, *17*, 39-59.

(58) Torres-Knoop, A.; Krishna, R.; Dubbeldam, D. Separating Xylene Isomers by Commensurate Stacking of p-Xylene within Channels of MAF-X8. *Angew. Chem. Int. Ed.* **2014**, *53*, 7774-7778.

(59) Mukherjee, S.; Joarder, B.; Manna, B.; Desai, A. V.; Chaudhari, A. K.; Ghosh, S. K. Framework-Flexibility Driven Selective Sorption of p-Xylene over Other Isomers by a Dynamic Metal-Organic Framework. *Sci. Rep.* **2014**, *4*, 5761. http://dx.doi.org/10.1038/srep05761

(60) Mukherjee, S.; Joarder, B.; Desai, A. V.; Manna, B.; Krishna, R.; Ghosh, S. K. Exploiting Framework Flexibility of a Metal-Organic Framework for Selective Adsorption of Styrene over Ethylbenzene. *Inorg. Chem.* **2015**, *54*, 4403-4408.

(61) Torres-Knoop, A.; Heinen, J.; Krishna, R.; Dubbeldam, D. Entropic Separation of Styrene/Ethylbenzene Mixtures by Exploitation of Subtle Differences in Molecular Configurations in Ordered Crystalline Nanoporous Adsorbents. *Langmuir* **2015**, *31*, 3771-3778.

(62) Maes, M.; Vermoortele, F.; Alaerts, L.; Couck, S.; Kirschhock, C. E. A.; Denayer, J. F. M.; De Vos, D. E. Separation of Styrene and Ethylbenzene on Metal-Organic Frameworks: Analogous Structures with Different Adsorption Mechanisms. *J. Am. Chem. Soc.* **2010**, *132*, 15277-15285.

(63) Divekar, S.; Nanoti, A.; Dasgupta, S.; Aarti; Chauhan, R.; Gupta, P.; Garg, M. O.; Singh, S. P.; Mishra, I. M. Adsorption Equilibria of Propylene and Propane on Zeolites and Prediction of Their Binary Adsorption with the Ideal Adsorbed Solution Theory. *J. Chem. Eng. Data* **2016**, *61*, 2629-2637.

(64) Kong, G. Q.; Han, Z. D.; He, Y.; Qu, S.; Zhou, W.; Yildirim, T.; Krishna, R.; Zou, C.; Wu, C. D.; Chen, B. Expanded Organic Building Units for the Construction of Highly Porous Metal-Organic Frameworks. *Chem. Eur. J.* **2013**, *19*, 14886-14894.

(65) Krishna, R. Adsorptive separation of $CO_2/CH_4/CO$ gas mixtures at high pressures. *Microporous Mesoporous Mater.* **2012**, *156*, 217-223.

(66) Chowdhury, P.; Mekala, S.; Dreisbach, F.; Gumma, S. Adsorption of CO, CO_2 and CH_4 on Cu-BTC and MIL-101 Metal Organic Frameworks: Effect of Open Metal Sites and Adsorbate Polarity. *Microporous Mesoporous Mater.* **2012**, *152*, 246-252.

(67) Moellmer, J.; Moeller, A.; Dreisbach, F.; Glaeser, R.; Staudt, R. High pressure adsorption of hydrogen, nitrogen, carbon dioxide and methane on the metal–organic framework HKUST-1. *Microporous Mesoporous Mater.* **2011**, *138*, 140-148.

(68) Krishna, R.; van Baten, J. M. In silico screening of metal-organic frameworks in separation applications. *Phys. Chem. Chem. Phys.* **2011**, *13*, 10593-10616.

(69) Bárcia, P. S.; Silva, J. A. C.; Rodrigues, A. E. Separation by fixed-bed adsorption of hexane isomers in zeolite BETA pellets. *Ind. Eng. Chem. Res.* **2006**, *45*, 4316-4328.

(70) Minceva, M.; Rodrigues, A. E. Understanding and Revamping of Industrial Scale SMB Units for p-Xylene Separation. *A.I.Ch.E.J.* **2007**, *53*, 138-149.

(71) Minceva, M.; Rodrigues, A. E. Adsorption of xylenes on Faujasite-type zeolite. Equilibrium and Kinetics in Batch Adsorber. *Chem. Eng. Res. Des.* **2004**, *82*, 667-681.

(72) He, C.-T.; Tian, J. Y.; Liu, S. Y.; Ouyang, G.; Zhang, J.-P.; Chen, X. M. A porous coordination framework for highly sensitive and selective solid-phase microextraction of non-polar volatile organic compounds. *Chem. Sci.* **2013**, *4*, 351-356.

(73) Lin, Y. S. Molecular Sieves for Gas Separation. *Science* **2016**, *353*, 121-122.

24. Caption for Figures

Figure 1. (a) Schematic of a packed bed adsorber.

Figure 2. Transient breakthrough simulations for 20/80 Xe/Kr mixtures at 298 K and 100 kPa in a fixed bed packed with SBMOF-2. (a) Plot of dimensionless gas phase concentrations of Xe and Kr along the dimensionless length of the adsorber, $\frac{z}{L}$, monitored at $\tau = 33$. (b) Plot of dimensionless gas phase concentrations of Xe and Kr at the position $z = L$, as a function of the dimensionless time, $\tau = \frac{tu}{L\varepsilon}$. (c) Plot of component molar loadings along the dimensionless length of the adsorber, $\frac{z}{L}$, monitored at $\tau = 33$. (d) Plot of component molar loadings at $z = L$, as a function of the dimensionless time, $\tau = \frac{tu}{L\varepsilon}$.

Figure 3. Transient breakthrough simulations for the (a) adsorption and (b) desorption cycles for separation of 20/80 Xe/Kr mixtures at 298 K and 100 kPa in a fixed bed packed with SBMOF-2. (a) Plot of ppm Xe vs $\tau = \frac{tu}{L\varepsilon}$ at the exit of fixed bed during the adsorption cycle. (b) Plot of ppm Kr vs $\tau = \frac{tu}{L\varepsilon}$ at the outlet during the desorption cycle.

Figure 4. Transient breakthrough of CO_2 and CH_4 mixtures in fixed bed adsorber packed with pellets of activated carbon operating at 293 K and constant total pressure of 501 kPa. (a) Plot of dimensionless gas phase concentrations of CO_2 and CH_4 as a function of time, *t*. (b) Plot of volumetric flow rate of the gas mixture as a function of time, *t*. The continuous solid lines are the shock wave solutions using the input data as reported for Run 3 in Table 1 and Figure 2 of Kluge et al.[6]. The symbols represent the experimental data scanned from Figure 2 of Kluge et al.[6]

Figure 5. Transient breakthrough simulations for HypMOF-17 with, $q_{sat} = 5$ mol kg^{-1}, and $S_{A/B} = b_A/b_B = 10$ with feed gas mixture composition, $y_A = 0.8$, and total pressure constant at the value $p_t = p_A + p_B = 100$ kPa. (a) The plot shows the gas phase molar concentrations of A and B in the exit of the fixed bed adsorber, plotted as a function of the dimensionless time, $\tau = \frac{tu}{L\varepsilon}$, obtained by dividing the actual time, *t*, by the characteristic time, $\frac{L\varepsilon}{u}$, where *L* is the length of adsorber, *u* is the superficial fluid velocity, ε is the bed voidage.[5] (b) The plots shows the gas phase mole fractions of A and B in the exit of the fixed bed adsorber, plotted as a function of the dimensionless time. (c) The plot shows the spatially averaged molar loadings of A and B within the MOFs in the fixed, plotted as a function of dimensionless time. (d) The plot shows the number of moles of 99.95% pure B that can be recovered from the exit product gas, express per

L of MOF in the packed bed, as a function of the dimensionless time. Also shown is separation potential $\Delta Q_{B/A}$, calculated from mixed-gas Langmuir model.

Figure 6. Transient breakthrough simulations for HypMOF-17 with, $q_{sat} = 5$ mol kg^{-1}, and $S_{A/B} = b_A/b_B = 10$ with feed gas mixture composition, $y_A = 0.2$, and total pressure constant at the value $p_t = p_A + p_B = 100$ kPa. (a) The plot shows the gas phase molar concentrations of A and B in the exit of the fixed bed adsorber, plotted as a function of the dimensionless time, $\tau = \frac{tu}{L\varepsilon}$. (b) The plot shows the gas phase mole fractions of A and B in the exit of the fixed bed adsorber, plotted as a function of the dimensionless time. (c) The plot shows the spatially averaged molar loadings of A and B within the MOFs in the fixed, plotted as a function of dimensionless time. (d) The plot shows the number of moles of 99.95% pure B that can be recovered from the exit product gas, express per L of MOF in the packed bed, as a function of the dimensionless time. Also shown is separation potential $\Delta Q_{B/A}$, calculated from mixed-gas Langmuir model.

Figure 7. Transient breakthrough simulations for HypMOF-17 with, $q_{sat} = 5$ mol kg^{-1}, and $S_{ads} = b_A/b_B = 10$ with varying feed gas mixture compositions, $y_A = 0.1$ (0.1)…0.9, keeping the total pressure constant at the value $p_t = p_A + p_B = 100$ kPa. (a) Plot of the number of moles of B produced per liter of HypMOF in the packed bed, as a function of the differences in dimensionless breakthrough times, $\Delta\tau$. (b) Plot of the number of moles of B produced per liter

of HypMOF in the packed bed, as a function of the separation potential, $\Delta Q_{B/A}$, calculated using equation (19).

Figure 8. (a) Transient breakthrough simulations for equimolar A/B mixtures in a fixed bed packed with HypMOF-9 and HypMOF-11, with adsorption isotherms as specified in Table 1, operating at 298 K, and a total pressure of 100 kPa. The plot shows the gas phase molar concentrations of A and B in the exit of the fixed bed adsorber, as a function of the dimensionless time, $\tau = \frac{tu}{L\varepsilon}$. (b) Plot of the number of moles of A captured per liter of HypMOF in the fixed bed, as a function of the dimensionless breakthrough time, τ_A. (c) Plot of the number of moles of A captured per liter of HypMOF in the fixed bed, as a function of the selectivity $S_{A/B}$. (c) Plot of the number of moles of B produced per liter of HypMOF in the packed bed, as a function of the selectivity $S_{A/B}$.

Figure 9. (a) Plot of the number of moles of A captured per liter of HypMOF in the fixed bed, plotted as a function of the volumetric uptake capacity of A, $Q = \rho q_A$, calculated using equation (24). (b) Plot of the number of moles of B produced per liter of HypMOF in the packed bed, as a function of the separation potential, $\Delta Q_{B/A}$, calculated using equation (19). (c, d) Plot of the % deviation between the productivity of 99.95% pure B, determined from breakthrough

simulations, with the corresponding values of the separation potential, $\Delta Q_{B/A}$, calculated from the mixed-gas Langmuir model, using equation (19).

Figure 10. Transient breakthrough simulations for (a) adsorption, and (b) desorption phases for HypMOF-17 with, $q_{sat} = 5$ mol kg^{-1}, and $S_{A/B} = b_A/b_B = 10$ with feed gas mixture composition, $y_A = 0.2$, and total pressure constant at the value $p_t = p_A + p_B = 100$ kPa. The plots show the % gas phase compositions of A and B in the exit of the fixed bed adsorber, as a function of the dimensionless time. For the desorption phase, the % compositions are on helium-free basis. (c) The plot shows the number of moles of 99.95% pure A that can be recovered from the exit product gas in the desorption cycle, per L of MOF in the packed bed, as a function of the separation potential $\Delta Q_{B/A}$, calculated using $\Delta Q_{B/A} = Q_A - Q_B \dfrac{y_A}{1-y_A} = \rho\left(q_A - q_B \dfrac{y_A}{1-y_A}\right)$.

Figure 11. (a) Transient breakthrough simulations for A/B/C mixture separation using hypothetical MOF with, $q_{sat} = 5$ mol kg^{-1}, and $b_A = 0.02$ Pa^{-1}; $b_B = 0.01$ Pa^{-1}; $b_C = 0.001$ Pa^{-1}. (b) Results of productivity calculations with varying feed gas mixture compositions, y_A, y_B, and y_C, keeping the total pressure constant at the value $p_t = p_A + p_B + p_C = 100$ kPa. Plot shows the number of moles of 99.95% pure C produced per liter of HypMOF in the packed bed, as a function of function of the separation potential, $\Delta Q_{C/BA} = Q_A \dfrac{y_C}{y_A} - \Delta Q_{B/A} \dfrac{y_C}{(1-y_C)} - Q_C$.

Figure 12. (a) Transient breakthrough simulations for A/B/C/D mixture separation using hypothetical MOF with, $q_{sat} = 5$ mol kg^{-1}, and $b_A = 0.02$ Pa^{-1}; $b_B = 0.01$ Pa^{-1}; $b_C = 0.002$ Pa^{-1}; $b_D = 0.0002$ Pa^{-1}. (b) Results of productivity calculations with varying feed gas mixture compositions, y_A, y_B, y_C, and y_D keeping the total pressure constant at the value $p_t = p_A + p_B + p_C + p_D = 100$ kPa. Plot of the number of moles of 99.95% pure D produced per liter of HypMOF in the packed bed, as a function of function of the separation potential, $\Delta Q_{D/CBA} = (Q_A + Q_B + Q_C)\frac{y_D}{1-y_D} - -Q_D$.

Figure 13. Separation of binary 20/80 Xe/Kr mixtures at 298 K and p_t = 100 kPa using NiMOF-74, Ag@NiMOF-74, CuBTC, SBMOF-2, CoFormate, and SAPO-34. (a) Plot of adsorption selectivity vs Xe uptake capacity, both calculated from IAST. (b, c) Transient breakthrough simulations for comparison of productivities of pure Kr in fixed bed adsorber, containing less than 1000 ppm Xe. (b) Plot of pure Kr productivity as a function of the separation potential $\Delta Q_{Kr/Xe} = Q_{Xe}\frac{0.8}{0.2} - Q_{Kr}$, calculated from IAST. (c) Plot of Xe capture capacity in fixed bed as a function of the Xe uptake Q_{Xe}, calculated from IAST. (d) Plot of pure Xe productivity as a function of the separation potential $\Delta Q_{Xe/Kr} = Q_{Xe} - Q_{Kr}\frac{0.2}{0.8}$, calculated from IAST; these are the

results of desorption simulations, with helium as inert gas. The unary isotherm data for MOFs are taken from earlier publications.[8, 12, 14]

Figure 14. Separation of 50/50 C_2H_2/CO_2 mixtures at 298 K and p_t = 100 kPa using UTSA-74, PCP-33, HOF-3, ZJU-60a, and ZnMOF-74. (a) Plot of the adsorption selectivity vs C_2H_2 uptake capacity. (b) Transient breakthrough simulations for comparison of productivities of 99.95% pure C_2H_2 in fixed bed adsorber, plotted as a function of the separation potential ΔQ, calculated from IAST. (c) Plot of C_2H_2 captured in fixed bed as a function of the C_2H_2 uptake from IAST. The isotherm data and breakthrough simulations are culled from Luo et al.[22]

Figure 15. (a) Structures of (a) SIFSIX-1-Cu, and (b) SIFSIX-2-Cu-i, highlighting the C_2H_2 binding with $(SiF_6)^{2-}$ anions. Adapted from Lin [73] and Cui et al. [23]

Figure 16. Separation of 1/99 C_2H_2/C_2H_4 mixtures at 298 K and p_t = 100 kPa using SIFSIX- (1-Cu, 2-Cu, 3-Zn, 2-Cu-i, 3-Ni), M'MOF-3a, and UTSA-100a. (a) Plot of the adsorption selectivity vs C_2H_2 uptake capacity. (b) Transient breakthrough simulations for comparison of productivities pure C_2H_4 (containing less than 40 ppm C_2H_2) in fixed bed adsorber, plotted as a function of the

separation potential $\Delta Q_{C2H4/C2H2} = Q_{C2H2}\frac{99}{1} - Q_{C2H4}$, calculated from IAST. (c) Plot of C_2H_2 captured in fixed bed as a function of the C_2H_2 uptake from IAST. The isotherm data for all the MOFs are the same as that reported in the work of Cui et al.[23] However, the transient breakthrough simulations are repeated here using parameters: adsorber length, L = 0.3 m; cross-sectional area, A = 1 m^2; superficial gas velocity in the bed, u = 0.04 m s^{-1}; voidage of the packed bed, ε = 0.4. The hierarchy of the MOFs is exactly the same as reported by Cui et al.,[23] as should be expected.

Figure 17. Separation of 50/50 C_2H_2/C_2H_4 mixtures at 298 K and p_t = 100 kPa using SIFSIX- (1-Cu, 2-Cu, 3-Zn, 2-Cu-i, 3-Ni), M'MOF-3a, and UTSA-100a. (a) Plot of the adsorption selectivity vs C_2H_2 uptake capacity. (b) Transient breakthrough simulations for comparison of productivities pure C_2H_4 (containing less than 40 ppm C_2H_2) in fixed bed adsorber, plotted as a function of the separation potential $\Delta Q_{C2H4/C2H2}$, calculated from IAST. (c) Plot of C_2H_2 captured in fixed bed as a function of the C_2H_2 uptake from IAST. The isotherm data for all the MOFs are the same as that reported in the work of Cui et al. [23] However, the transient breakthrough simulations are repeated here using parameters: adsorber length, L = 0.3 m; cross-sectional area, A = 1 m^2; superficial gas velocity in the bed, u = 0.04 m s^{-1}; voidage of the packed bed, ε = 0.4. The hierarchy of the MOFs is exactly the same as reported by Cui et al.,[23] as should be expected.

Figure 18. (a) Side-on attachment of C_2H_4 molecules to metal atoms of Fe-MOF-74, that has 1D hexagonal-shaped channels of 11 Å size. Adapted from Bloch et al.[26] (b, c) Transient breakthrough simulations for (b) adsorption, and (c) desorption phases for separation of 50/50 C_2H_4/C_2H_6 mixtures in fixed bed adsorbers packed with CoMOF-74, operating at 298 K and 100 kPa total pressure. For the transient breakthrough simulations of the desorption cycle, an inert non-adsorbing gas is injected into the equilibrated bed at time t = 0, at a total pressure of 100 kPa.

Figure 19. (a) Structure of NbOFFIVE-1-Ni (= KAUST-7), highlighting the C_3H_6 binding with $(NbOF_5)^{2-}$ anions. Adapted from Lin.[73] (b, c) Transient breakthrough simulations for (b) adsorption, and (c) desorption phases for separation of 50/50 C_3H_6/C_3H_8 mixtures in fixed bed adsorbers packed with KAUST-7, operating at 298 K and 100 kPa total pressure. For the transient breakthrough simulations of the desorption cycle, an inert non-adsorbing gas is injected into the equilibrated bed at time t = 0, at a total pressure of 100 kPa.

Figure 20. Separation of 50/50 C_2H_4/C_2H_6 mixtures at 298 K and p_t = 100 kPa using M-MOF-74 (M= Fe, Co, Mn, Mg, Zn), PAF-1-SO_3Ag (= PAF) MIL-101-Cr-SO_3Ag (= MIL), and NOTT-300 (= NOTT). (a) Plot of the adsorption selectivity vs C_2H_4 uptake capacity. (b) Transient breakthrough simulations (adsorption cycle) for comparison of productivities of 99.95% pure C_2H_6 in fixed bed adsorber, plotted as a function of the separation potential $\Delta Q_{C2H6/C2H4}$, calculated from IAST. (c) Plot of C_2H_4 captured (adsorption cycle) in fixed bed as a function of

the C_2H_4 uptake from IAST. (d) Transient breakthrough simulations (desorption cycle) for comparison of productivities of 99.95% pure C_2H_4 in fixed bed adsorber, plotted as a function of the separation potential $\Delta Q_{C2H4/C2H6}$, calculated from IAST. The unary isotherm data of C_2H_4, and C_2H_6 in the various MOFs examined are specified in Table 3, and Table 4.

Figure 21. Separation of 50/50 C_3H_6/C_3H_8 mixtures at 298 K and p_t = 100 kPa using M-MOF-74 (M= Fe, Co, Ni, Mn, Mg, Zn), 13X zeolite, LTA-5A zeolite, and KAUST-7. (a) Plot of the adsorption selectivity vs C_3H_6 uptake capacity. (b) Transient breakthrough simulations (adsorption cycle) for comparison of productivities of 99.95% pure C_3H_8 in fixed bed adsorber, plotted as a function of the separation potential $\Delta Q_{C3H8/C3H6}$, calculated from IAST. (c) Plot of C_3H_6 captured (adsorption cycle) in fixed bed as a function of the C_3H_6 uptake from IAST. The unary isotherm data of C_3H_6, and C_3H_8 used are specified in Table 5, and Table 6.

Figure 22. (a) IAST calculations of adsorption selectivity, $S_{CO2/CH4}$, vs CO_2 uptake capacity of 50/50 CO_2/CH_4 mixture at 298 K and 100 kPa using MgMOF-74, NiMOF-74, NaX zeolite, Kureha carbon and Cu-TDPAT. (b) Transient breakthrough simulations for comparison of productivities of 99.95% pure CH_4 in fixed bed adsorber operating at 0.6 MPa, plotted as a function of the separation potential $\Delta Q_{CH4/CO2}$, calculated from IAST. (c) Plot of CO_2 captured (adsorption cycle) in fixed bed as a function of the CO_2 uptake capacity from IAST. The unary isotherm data sources for CO_2, and CH_4 are specified in Table 7.

Figure 23. Schematic showing the attachment of O atoms of CO_2 molecules to the metal atoms of MgMOF-74.

Figure 24. (a) IAST calculations of adsorption selectivity, $S_{CO2/CH4}$, vs CO_2 uptake capacity of 50/50 CO_2/CH_4 mixture at 298 K and 0.6 MPa using MgMOF-74, NiMOF-74, NaX zeolite, Kureha carbon and Cu-TDPAT. (b) Transient breakthrough simulations for comparison of productivities of 99.95% pure CH_4 in fixed bed adsorber operating at 0.6 MPa, plotted as a function of the separation potential $\Delta Q_{CH4/CO2}$, calculated from IAST. (c) Plot of CO_2 captured (adsorption cycle) in fixed bed as a function of the CO_2 uptake capacity from IAST. The unary isotherm data sources for CO_2, and CH_4 are specified in Table 7.

Figure 25. (a, b, c, d, e) Experimental breakthroughs for CO_2/CH_4 mixtures in packed bed with (a) Mg_2(dobdc) (= MgMOF-74), (b) Co_2(dobdc) (= CoMOF-74), (c) Ni_2(dobdc) (= NiMOF-74), (d) MIL-100(Cr), and (e) Activated Carbon (AC) at 298 K. The experimental data, indicated by the symbols are from Li et al.[38]. The *y*-axis represents the % CH_4 in the exit gas phase, excluding the presence of inert gas. The partial pressures at the inlet are p_1 = 40 kPa; p_2 = 60 kPa; p_t = 100 kPa. The continuous solid lines are the calculations using the shock wave model. (f) Plot of the volumetric productivity of CH_4 vs the displacement time interval, Δt, for the five different adsorbent materials.

Figure 26. (a, b) Experimental data of Chen et al.[39] and Yu et al.[37] for transient breakthroughs of CO_2/CH_4/He mixtures in bed packed with (a) NiMOF-74 and (b) Kureha carbon, operating at T = 298 K. The inlet partial pressures of CO_2, CH_4, and Helium are 50 kPa, 50 kPa, and 100 kPa, respectively. The total pressure in the fixed bed is constant 200 kPa. The continuous solid lines are the calculations using the shock wave model. (c) Plot of the volumetric productivity of CH_4 vs the displacement time interval, Δt, for the two different adsorbent materials.

Figure 27. (a) IAST calculations of adsorption selectivity, $S_{CO2/N2}$, vs CO_2 uptake capacity for separation of 15/85 CO_2/N_2 mixtures at 298 K and 100 kPa using MgMOF-74, NiMOF-74, NaX zeolite, Kureha carbon and NOTT-300. (b) Transient breakthrough simulations for comparison of productivities of 99.95% pure N_2 in fixed bed adsorber operating at 100 kPa, plotted as a function of the separation potential $\Delta Q_{N2/CO2} = Q_{CO2}\dfrac{0.85}{0.15} - Q_{N2}$, calculated from IAST. The unary isotherm data sources for CO_2, and N_2 are specified in Table 8.

Figure 28. (a) IAST calculations of adsorption selectivity, $S_{CO2/H2}$, vs CO_2 uptake capacity for separation of 20/80 CO_2/H_2 mixtures at 298 K and 7 MPa, using MgMOF-74, 13X zeolite, LTA-5A, CuTDPAT, and MIL-101. (b) Transient breakthrough simulations for comparison of productivities of 99.95% pure H_2 in fixed bed adsorber operating at 7 MPa, plotted as a function

of the separation potential $\Delta Q_{H2/CO2} = Q_{CO2}\frac{0.8}{0.2} - Q_{H2}$, calculated from IAST. The unary isotherm data sources for CO_2, and H_2 are specified in Table 9. The transient breakthrough simulation data are the same as those published in earlier work.[51]

Figure 29. (a) Transient breakthrough simulations for separation of 40/10/50 $CO_2/CH_4/H_2$ mixtures at 298 K and 7 MPa in fixed bed adsorber packed with CuTDPAT. (b) Comparison of productivities of 99.95% pure H_2, plotted as a function of the separation potential $\Delta Q_{H2/[CH4+CO2]} = \left(Q_{CO2} + Q_{CH4}\right)\frac{y_{H2}}{\left(1-y_{H2}\right)} - Q_{H2}$, calculated from IAST. The unary isotherm data sources for CO_2, CH_4, and H_2 are specified in Table 9. The transient breakthrough simulation data are the same as those published in earlier work.[51]

Figure 30. (a) Transient breakthrough simulations for separation of 40/5/5/50 $CO_2/CO/CH_4/H_2$ mixtures at 298 K and 6 MPa in fixed bed adsorber packed with CuTDPAT. (b) Comparison of productivities of 99.95% pure H_2, plotted as a function of the separation potential, $\Delta Q_{H2/(CO+CH4+CO2)} = \left(Q_{CO2} + Q_{CO} + Q_{CH4}\right)\frac{y_{H2}}{\left(1-y_{H2}\right)} - Q_{H2}$, calculated from IAST and equation (43). The unary isotherm data sources for CO_2, CO, CH_4, and H_2 are specified in Table 9. The transient breakthrough simulation data are the same as those published in earlier work.[51]

Figure 31. Separation of binary 50/50 n-pentane(nC5)/2-methylbutane (2MB) mixtures at 433 K and p_t = 100 kPa using $Fe_2(BDP)_3$, MFI zeolite, ZIF-8, ZIF-77. (a) Plot of adsorption selectivity vs 2MB uptake capacity. (b) Plot of the 99% pure 2MB productivity as a function of the separation potential $\Delta Q_{2MB/nC5}$, calculated from IAST. The isotherm data for the four adsorbents and the transient breakthrough simulations are the same as that reported in earlier work; [54] the fit parameters are specified in Tables 10, 11, 12, and 13.

Figure 32. The triangular channel framework topology of $Fe_2(BDP)_3$; from Herm et al.;[53] reprinted with permission from AAAS. Snapshots of nC5, 2MB, and neo-P within the triangular channels of $Fe_2(BDP)_3$. Also shown are the snapshots of the hexane isomers: n-hexane (nC6), 2-methylpentane (2MP), 3-methylpentane (3MP), 2,2-dimethylbutane (22DMB) and 2,3-dimethylbutane (23DMB).

Figure 33. (a) Currently employed processing scheme for nC6 isomerization and subsequent separation step using LTA-5A zeolite. (b) Improved processing scheme for the nC6 isomerization process.

Figure 34. Simulations of breakthrough characteristics for 5-component nC6/2MP/3MP/22DMB/23DMB mixture in a fixed bed adsorber packed with $Fe_2(BDP)_3$, (framework density ρ = 1.145 kg L^{-1}), operating at a total pressure of 100 kPa and 433 K. The partial pressures of the components in the bulk gas phase at the inlet are $p_1 = p_2 = p_3 = p_4 = p_5 =$

20 kPa. The CBMC simulated pure component isotherms are fitted with the parameters specified in Table 10.

Figure 35. Simulations of breakthrough characteristics for 5-component nC6/2MP/3MP/22DMB/23DMB mixture in a fixed bed adsorber packed with ZIF-77 (framework density ρ = 1.552 kg L^{-1}) operating at a total pressure of 100 kPa and 433 K. The simulation details are the same as the ones provided by Herm et al.[53] The partial pressures of the components in the bulk gas phase at the inlet are $p_1 = p_2 = p_3 = p_4 = p_5$ = 20 kPa. The CBMC simulated pure component isotherms are fitted with the parameters specified in Table 13.

Figure 36. Simulations of breakthrough characteristics for 5-component nC6/2MP/3MP/22DMB/23DMB mixture in a fixed bed adsorber packed with MFI (framework density ρ = 1.796 kg L^{-1}) operating at a total pressure of 100 kPa and 433 K. The partial pressures of the components in the bulk gas phase at the inlet are $p_1 = p_2 = p_3 = p_4 = p_5$ = 20 kPa. The CBMC simulated pure component isotherms are fitted with the parameters specified in Table 11.

Figure 37. Simulations of breakthrough characteristics for 5-component nC6/2MP/3MP/22DMB/23DMB mixture in a fixed bed adsorber packed with Co(BDP). The CBMC simulated pure component isotherms are fitted with the parameters specified in Table 14.

Figure 38. Simulations of breakthrough characteristics for 5-component nC6/2MP/3MP/22DMB/23DMB mixture in a fixed bed adsorber packed with MgMOF-74. The CBMC simulated pure component isotherms are fitted with the parameters specified in Table 15.

Figure 39. Simulations of breakthrough characteristics for 5-component nC6/2MP/3MP/22DMB/23DMB mixture in a fixed bed adsorber packed with ZnMOF-74. The CBMC simulated pure component isotherms are fitted with the parameters specified in Table 16.

Figure 40. Simulations of breakthrough characteristics for 5-component nC6/2MP/3MP/22DMB/23DMB mixture in a fixed bed adsorber packed with ZIF-8. The CBMC simulated pure component isotherms are fitted with the parameters specified in Table 17.

Figure 41. Simulations of breakthrough characteristics for 5-component nC6/2MP/3MP/22DMB/23DMB mixture in a fixed bed adsorber packed with BEA. The pure component isotherms are fitted with the parameters specified in Table 18.

.

Figure 42. Simulations of breakthrough characteristics for 5-component nC6/2MP/3MP/22DMB/23DMB mixture in a fixed bed adsorber packed with with Zn(bdc)dabco. The CBMC simulated pure component isotherms are fitted with the parameters specified in Table 19.

Figure 43. Simulations of breakthrough characteristics for 5-component nC6/2MP/3MP/22DMB/23DMB mixture in a fixed bed adsorber packed with ZnHBDC,

Figure 44. Simulations of breakthrough characteristics for 5-component nC6/2MP/3MP/22DMB/23DMB mixture in a fixed bed adsorber packed with UiO-66. The simulation data are the same as those presented in the Supplementary material accompanying the paper by Krishna.[1]

Figure 45. Simulations of breakthrough characteristics for 5-component nC6/2MP/3MP/22DMB/23DMB mixture in a fixed bed adsorber packed with CFI. The simulation data are the same as those presented in the Supplementary material accompanying the paper by Krishna.[1]

Figure 46. Simulations of breakthrough characteristics for 5-component nC6/2MP/3MP/22DMB/23DMB mixture in a fixed bed adsorber packed with ATS. The simulation data are the same as those presented in the Supplementary material accompanying the paper by Krishna.[1]

Figure 47. Transient breakthrough simulations for separation of equimolar nC6/2MP/3MP/22DMB/23DMB mixtures at 433 K and 100 kPa in fixed bed adsorber. Comparison of 92+ RON productivity for operation at total pressure of 100 kPa, plotted as a function of the separation potential

$$\Delta Q_{(22DMB+23DMB)/(nC6+2MP+3MP)} = \left(Q_{nC6} + Q_{2MP} + Q_{3MP}\right)\frac{y_{22MB} + y_{23DMB}}{1 - y_{22MB} - y_{23DMB}} - \left(Q_{22DMB} + Q_{23DMB}\right),$$

calculated using IAST. The unary isotherm data are specified in Tables 10, 11, 12, 13, 14, 16, 17, 18, and 15.

Figure 48. (a, b) Transient breakthrough simulations for separation of equimolar nC6/3MP/22DMB mixtures at 433 K in fixed bed adsorber packed with (a) ZIF-77, and (b) ZnMOF-74. The plots also show the RON of the product at the outlet of the fixed bed. (c) Comparison of 90+ RON productivity for operation at total pressure of 300 kPa, plotted as a function of the separation potential $\Delta Q_{22DMB/(3MP+nC6)} = \left(Q_{nC6} + Q_{3MP}\right)\frac{y_{22DMB}}{\left(1 - y_{22DMB}\right)} - Q_{22DMB}$, calculated from IAST. (d) Plot of 90+ RON productivity vs $\Delta Q_{22DMB/(3MP+nC6)}$ for operations at

total pressure of 100 kPa. The unary isotherm data are specified in Tables 10, 11, 12, 13, 14, 16, 17, 18, and 15.

Figure 49. Schematic showing the separations of the oX/mX/pX/EthBz mixtures in a Simulated Moving Bed (SMB) unit.

Figure 50. (a) IAST calculations for p-xylene adsorption selectivity for 4-component o-xylene/m-xylene/p-xylene/ethylbenzene mixture in MAF-X8, JUC-77, Co(BDP), MIL-125, MIL-125-NH_2, and BaX zeolite, plotted against the volumetric uptake of p-xylene; these data are culled from Figure 5 of Torres-Knoop et al.[58] (b) Commensurate stacking of p-xylene within 10 Å channels of MAF-X8.[58] (c) Schematic representation of the framework flexibility of DynaMOF-100 with selective accommodation of p-xylene from xylenes mixture.[59] The unary isotherm data sources are provided in Table 23.

Figure 51. The separation potential, $\Delta Q_{(oX+mX+EthBz)/pX}$ for separation of 4-component o-xylene/m-xylene/p-xylene/ethylbenzene mixtures plotted against the volumetric uptake of p-xylene.

Figure 52. (a) Current processing scheme for styrene production by vacuum fractionation of styrene/ethylbenzene mixtures. (b) Schematic representation of the framework flexibility of DynaMOF-100 with selective accommodation of styrene from mixtures with ethylbenzene.[60]

Figure 53. (a, b) IAST calculations for (a) adsorption selectivity, and (b) uptake capacity of equimolar styrene/ethylbenzene mixtures in MIL-47(V), MIL-53(Al), and DynaMOF-100. The *x*-axis is fractional occupancy, θ_t, within the pores of the MOFs. (c) Plot of selectivity vs styrene uptake capacity at $\theta_t \approx 1$. (d) (c) Plot of the separation potential, $\Delta Q_{EthBz/Sty} = Q_{St} - Q_{EthBz}$, vs styrene uptake capacity at $\theta_t \approx 1$. The unary isotherm data sources are provided in Table 24.

Figure S1

Fixed bed adsorber

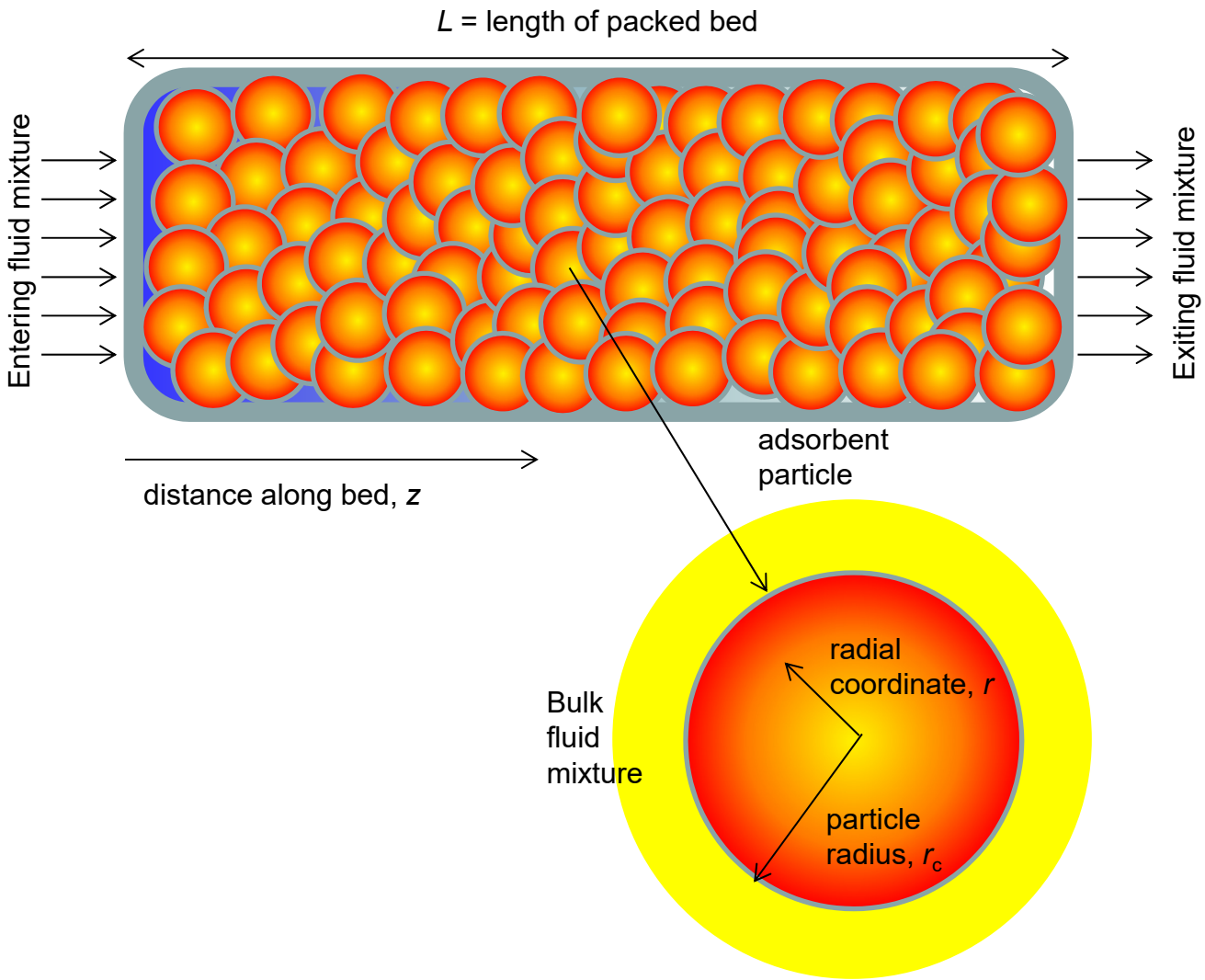

Numerical solutions vs Shock wave solution

Figure S2

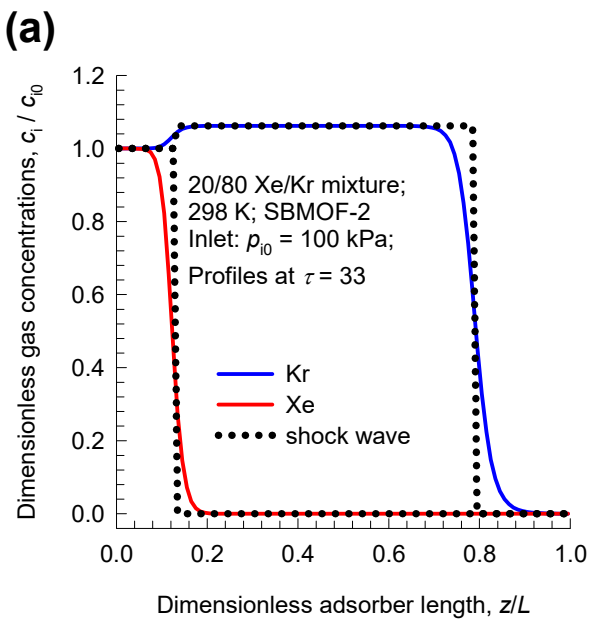

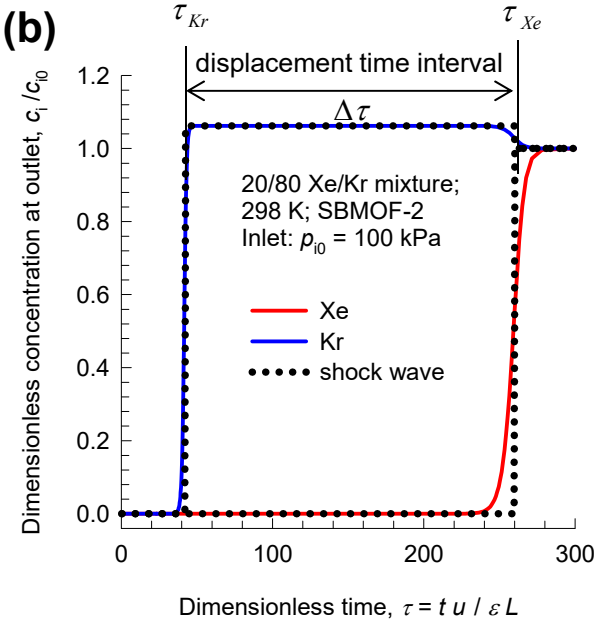

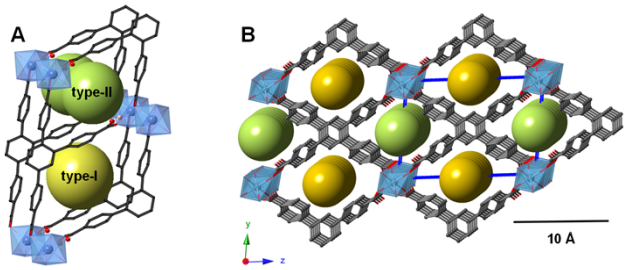

Structure of SBMOF-2

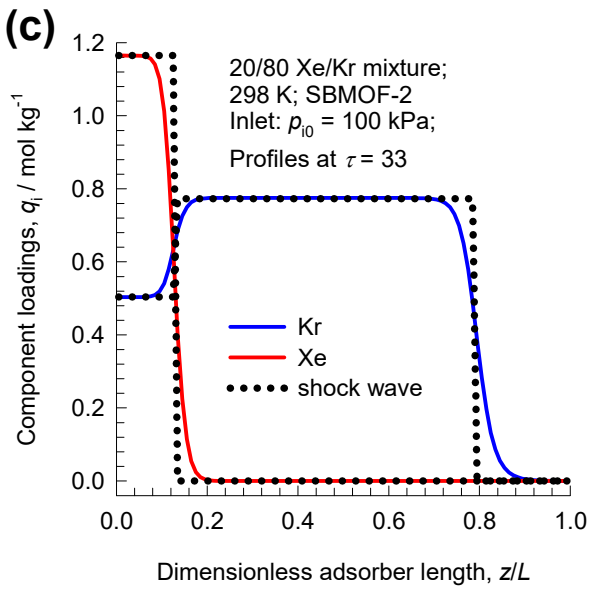

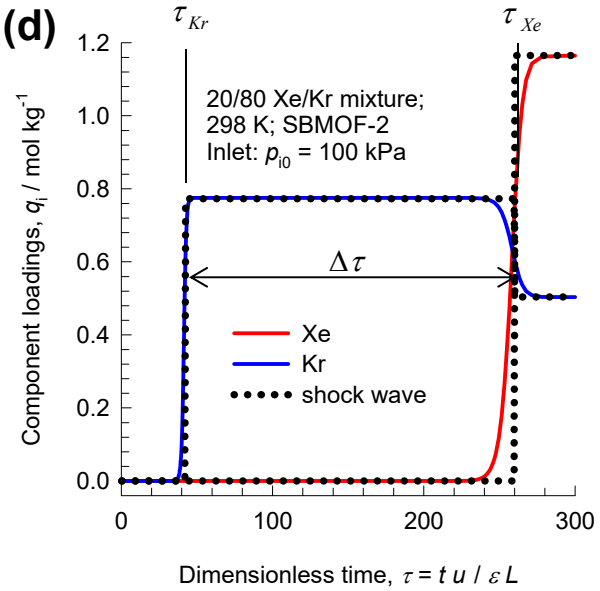

Xe/Kr adsorption/desorption Cycles

Figure S3

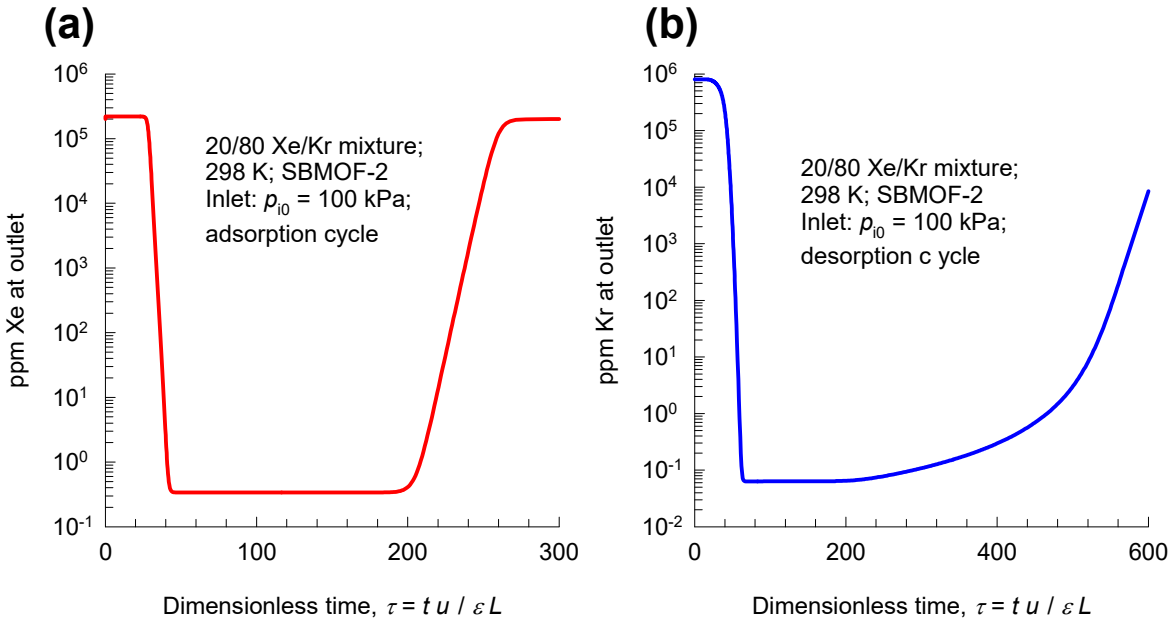

Breakthrough Expt vs Shock wave solution

Figure S4

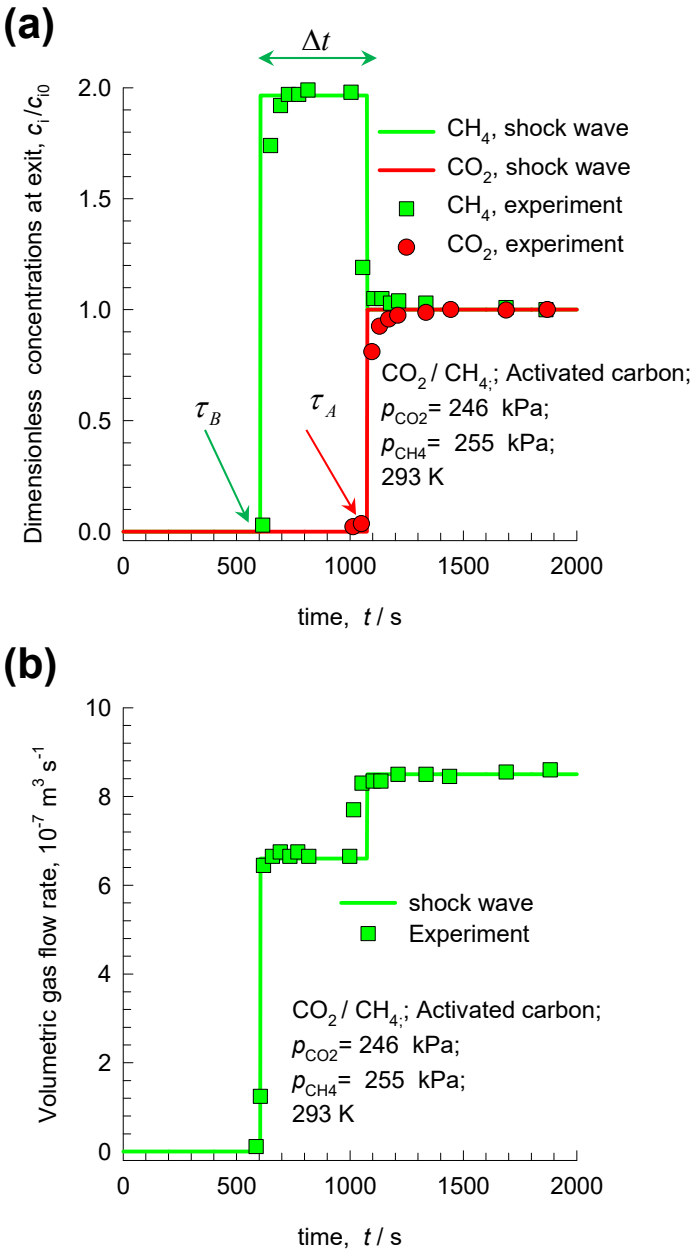

Figure S5

Separating A/B mixture

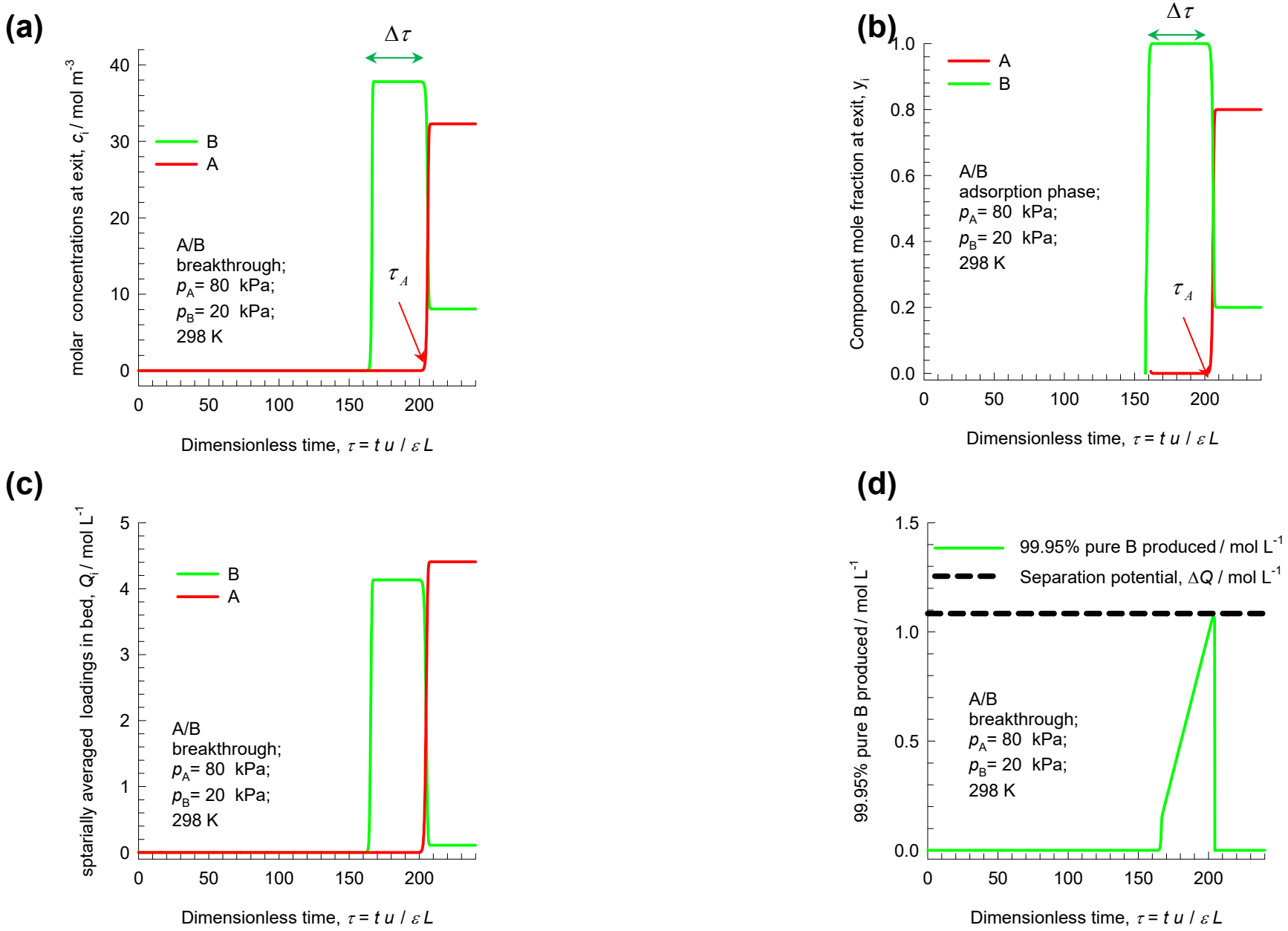

Figure S6

Separating A/B mixture

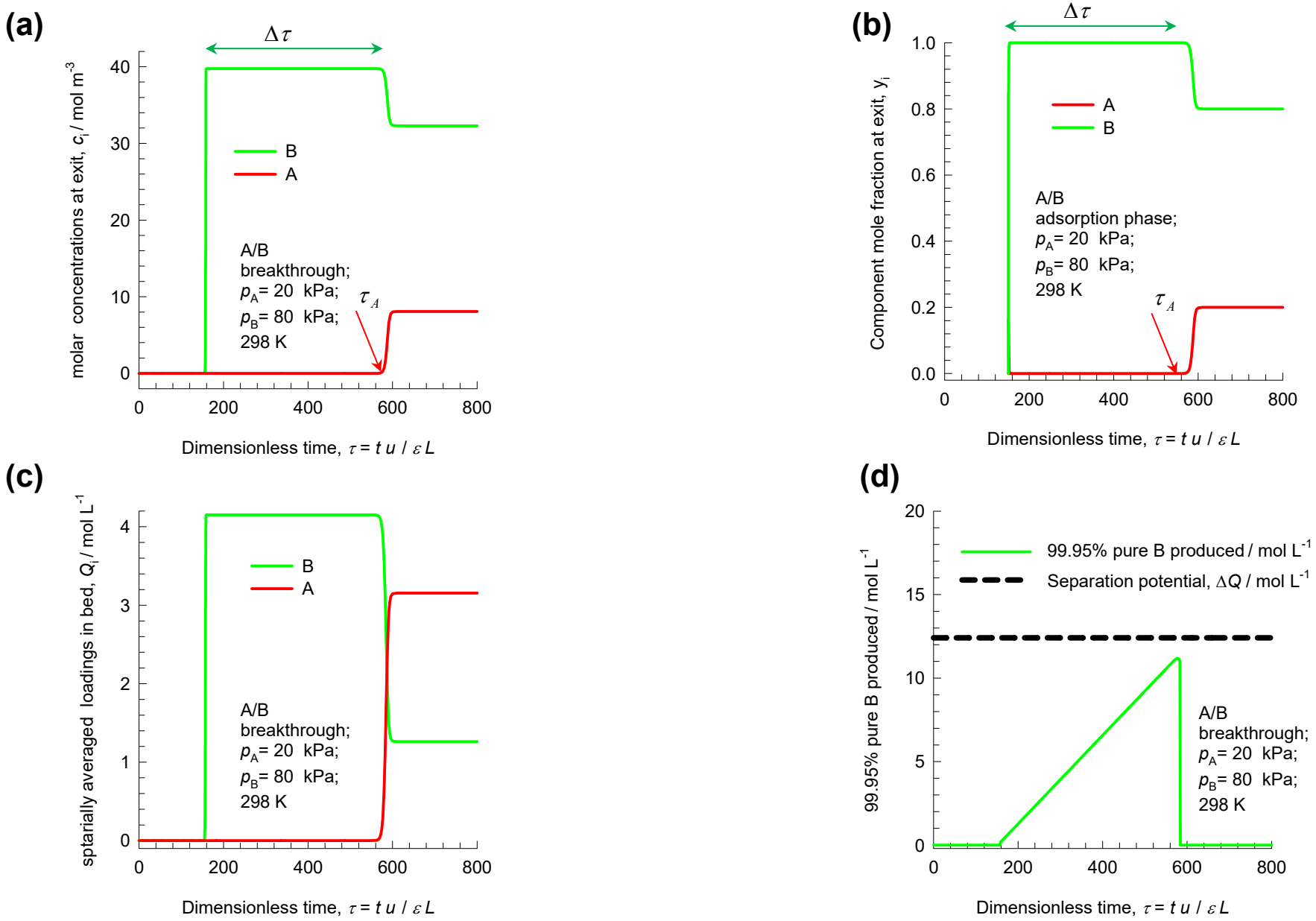

Figure S7

Separating A/B mixture

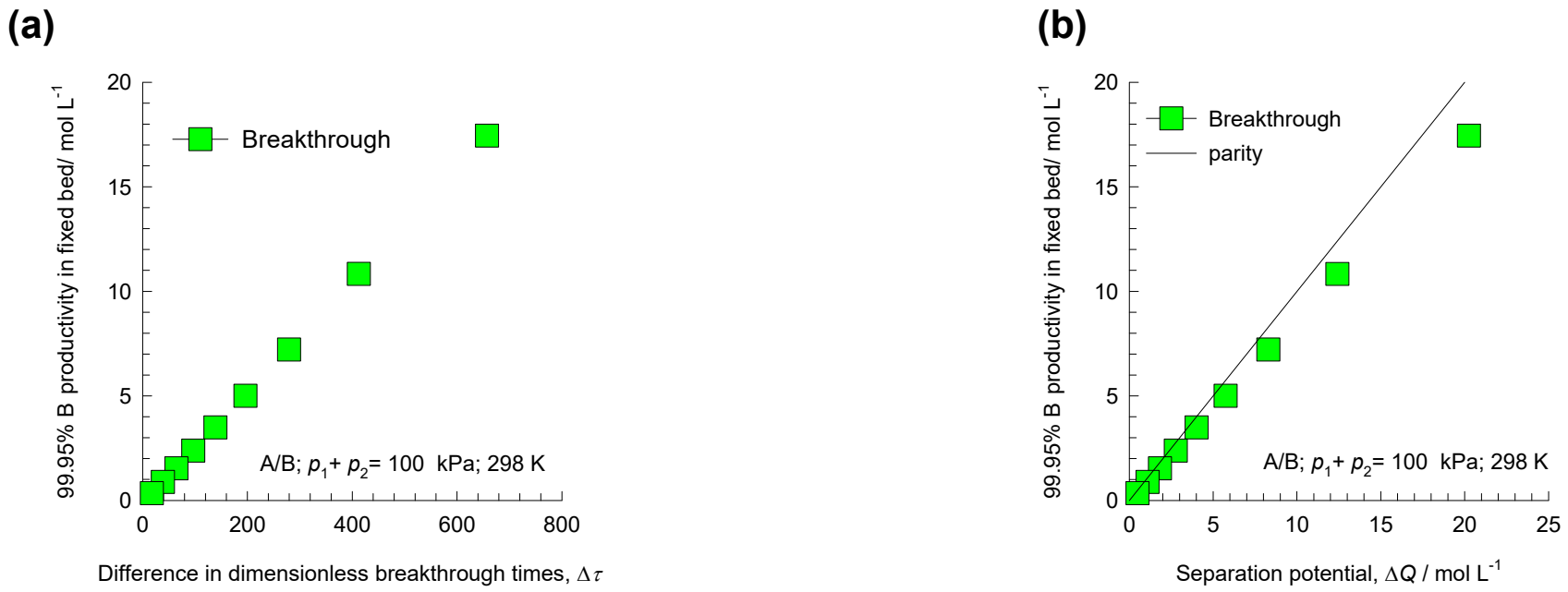

Figure S8

Separating A/B mixture

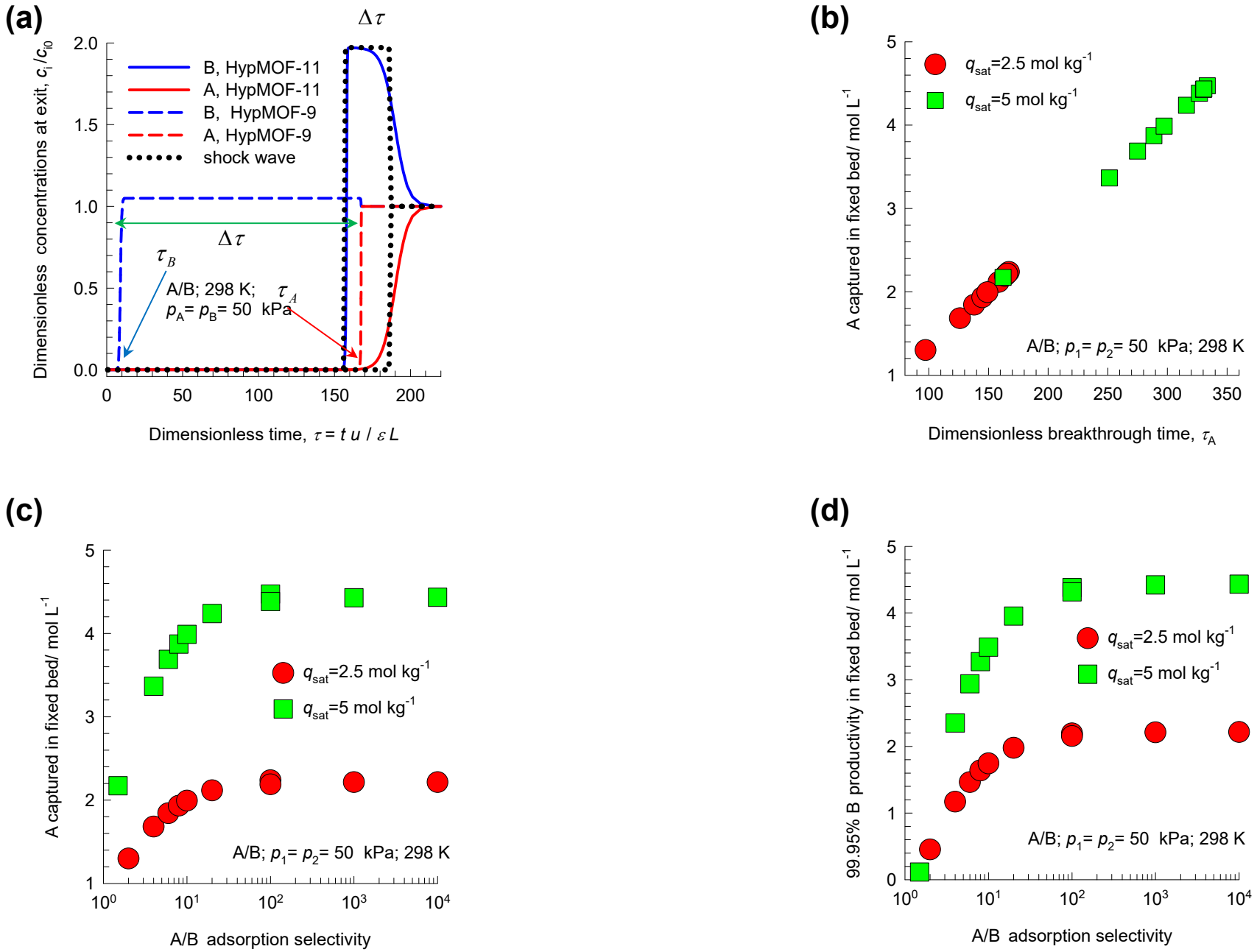

Figure S9

Separating A/B mixture

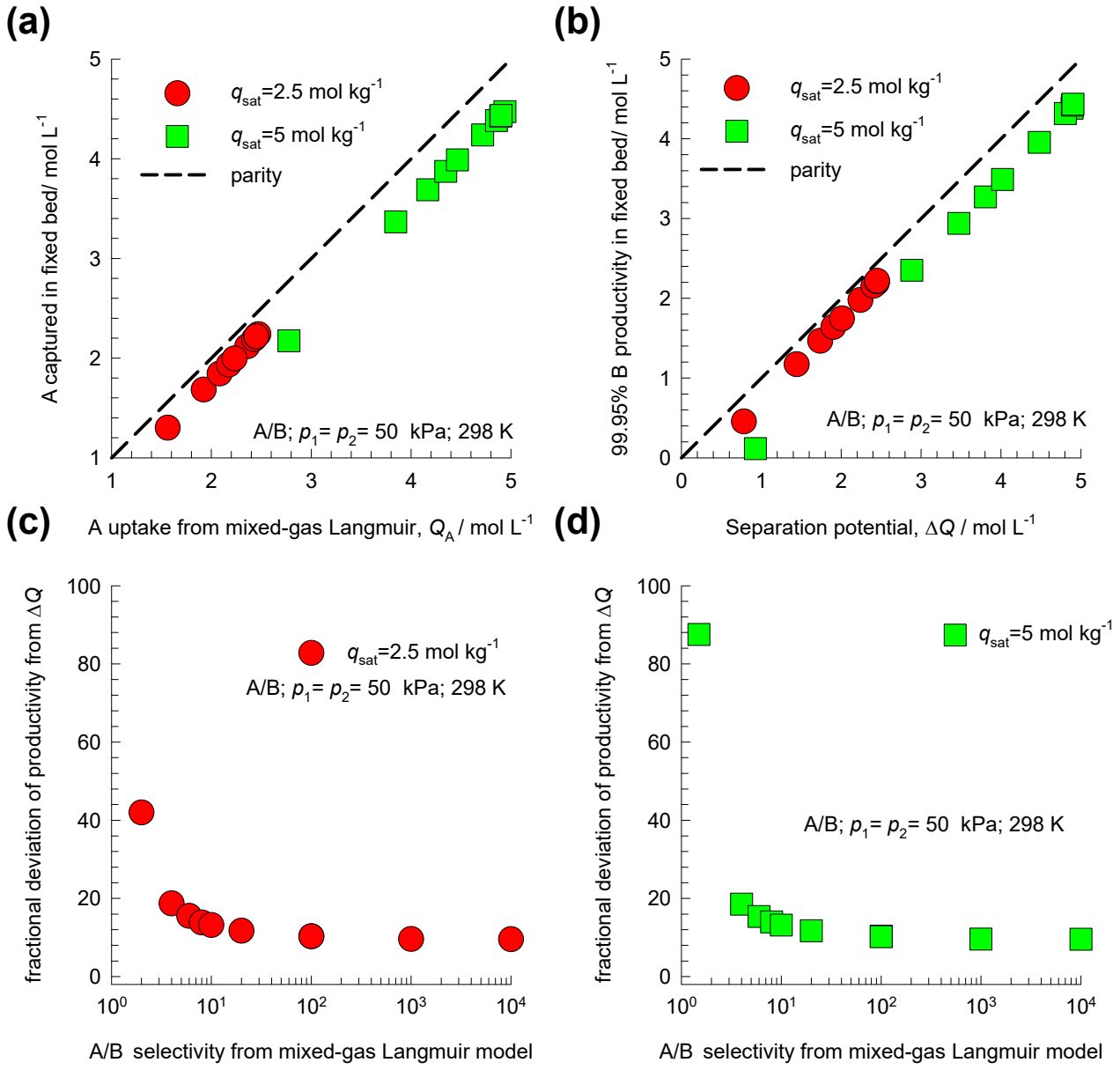

Figure S10

Separating A/B mixture

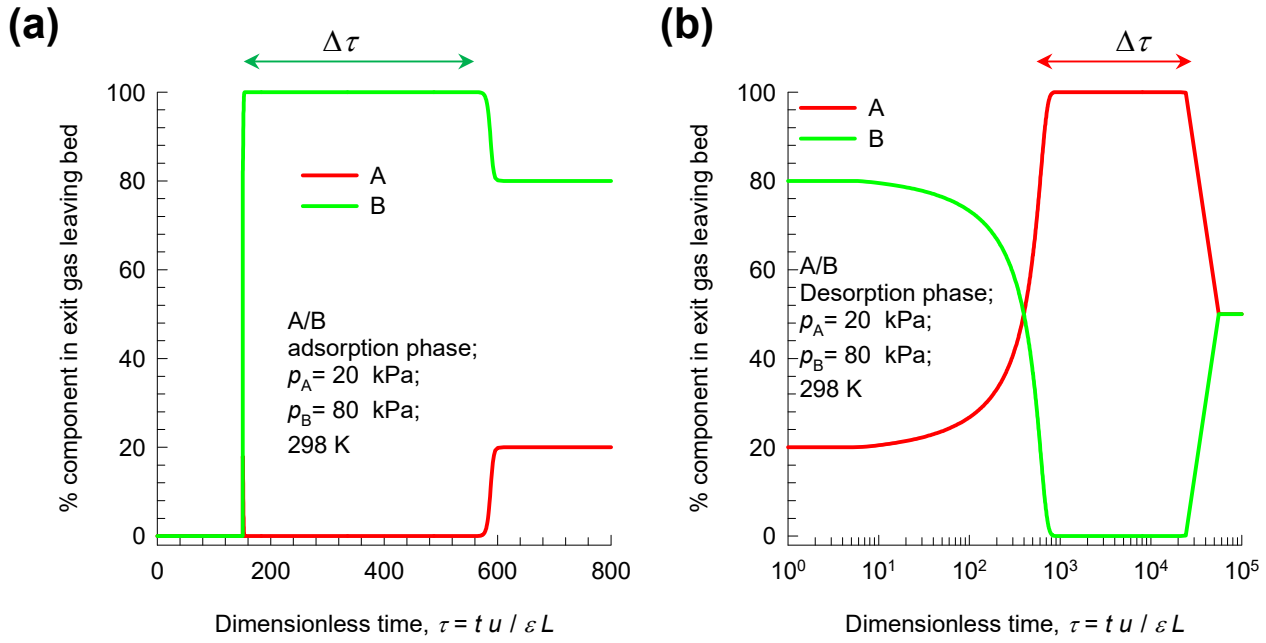

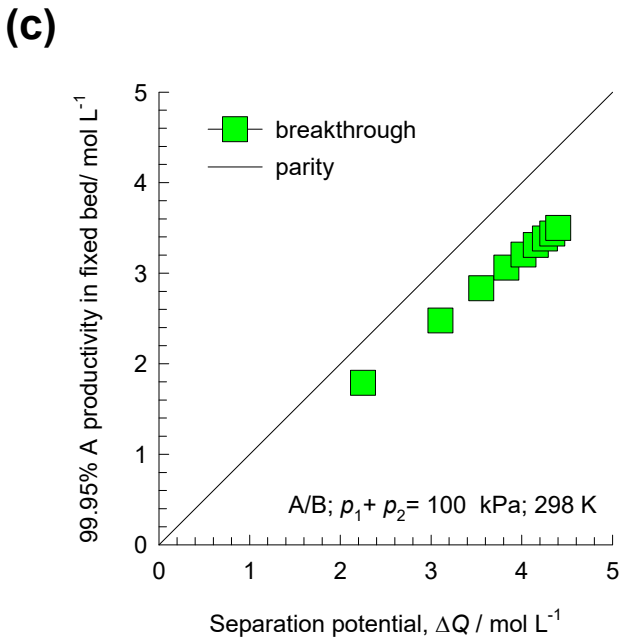

Separating A/B/C mixture

Figure S11

(a)

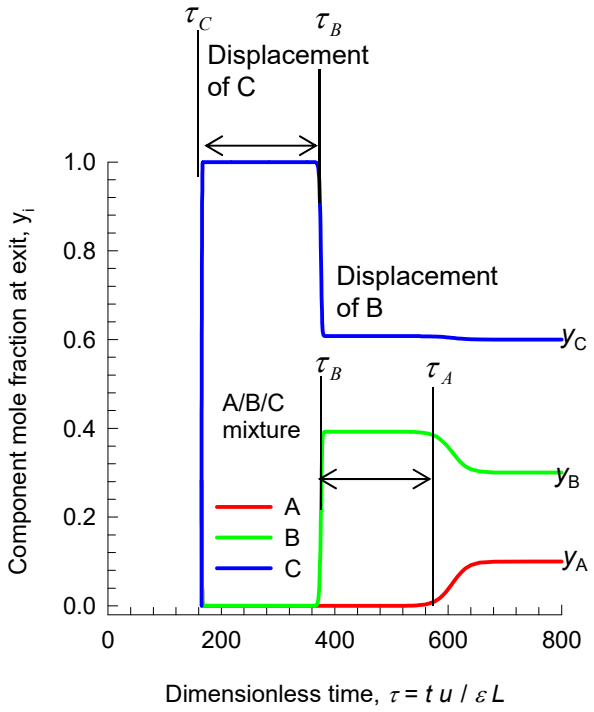

(b)

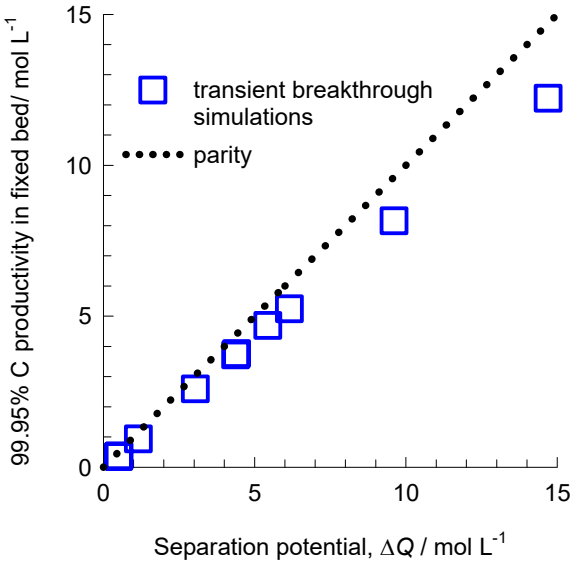

Separating A/B/C/D mixture

Figure S12

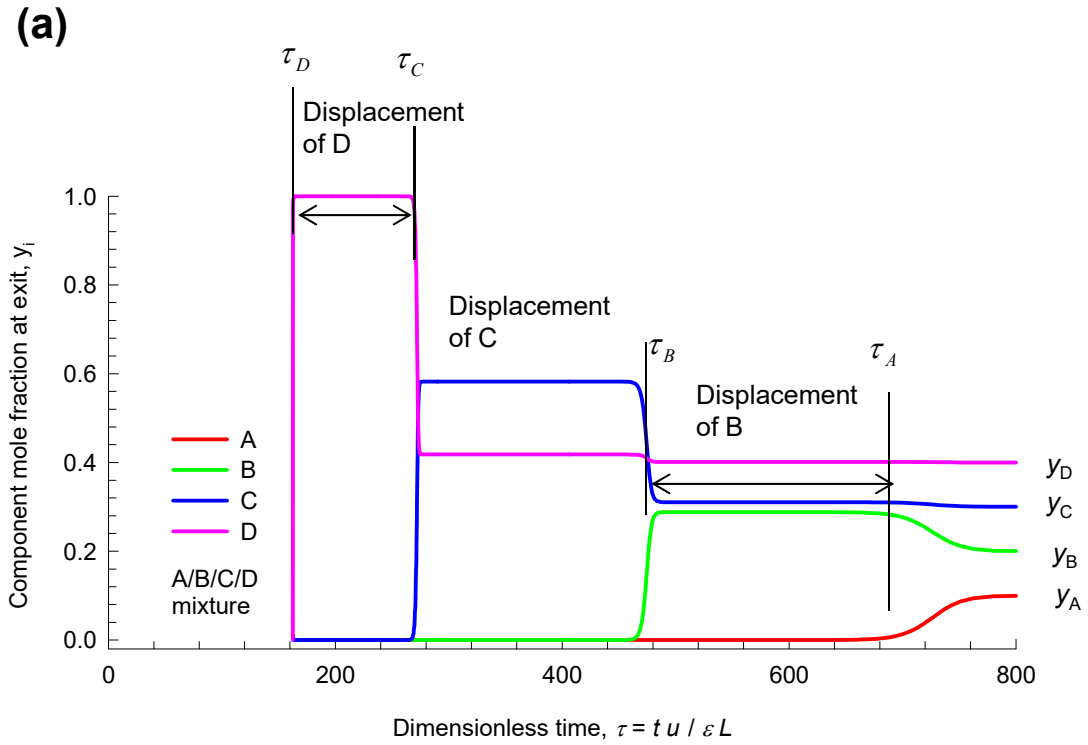

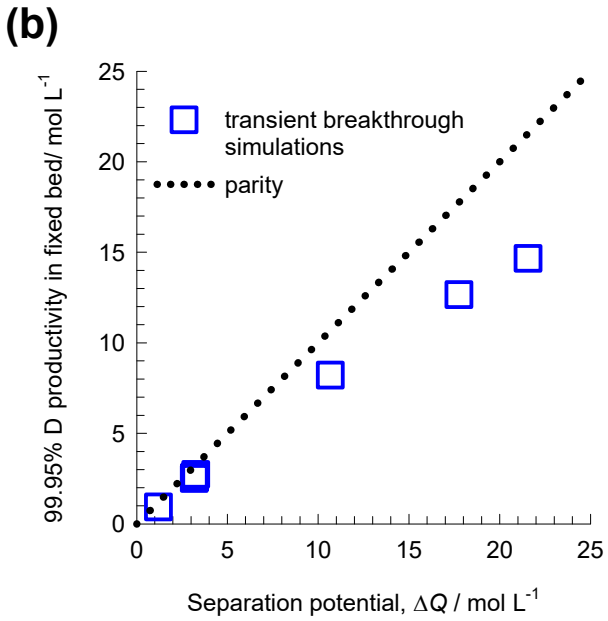

Figure S13

Separating 20/80 Xe/Kr

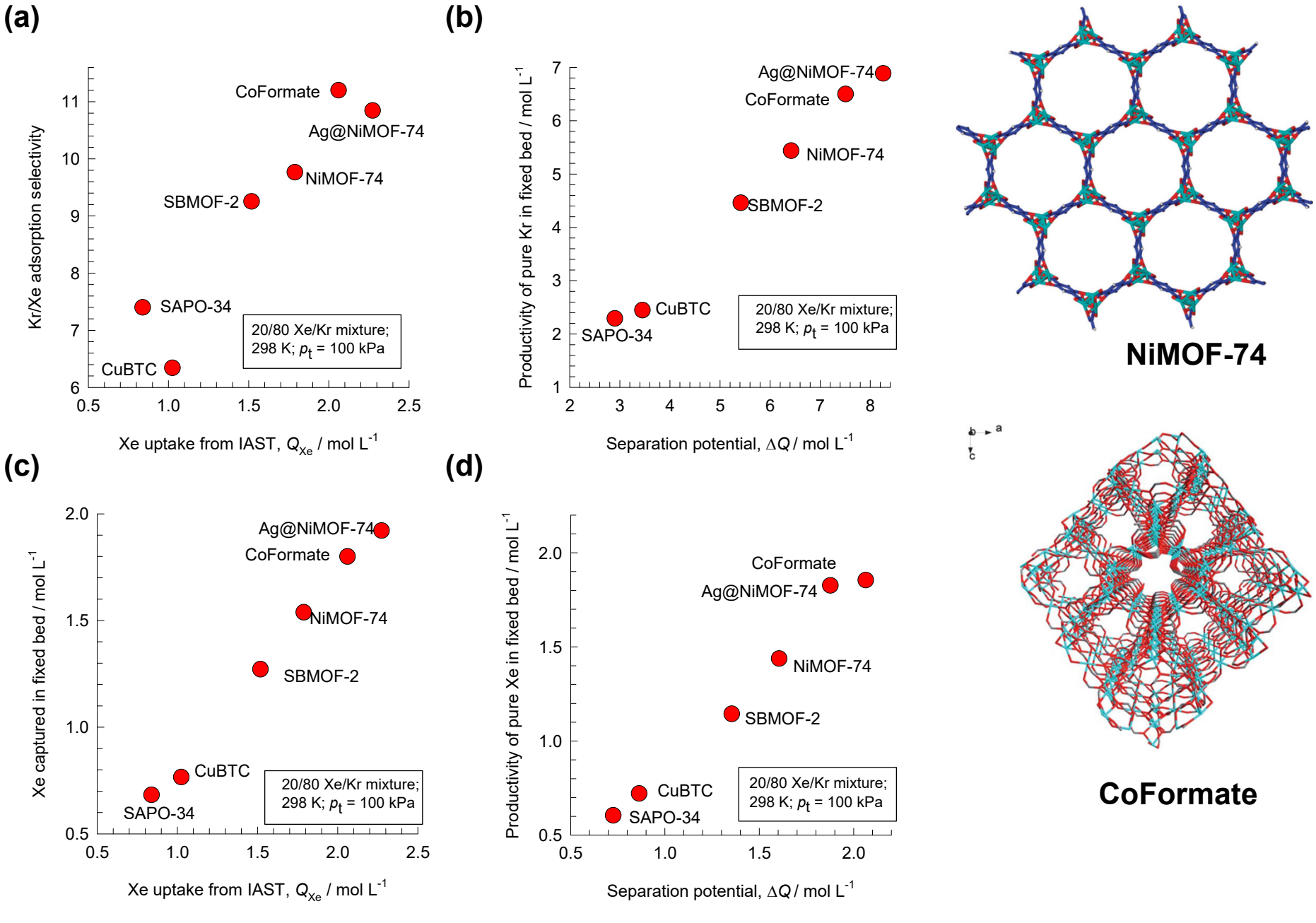

Figure S14

Separating 50/50 C_2H_2/CO_2

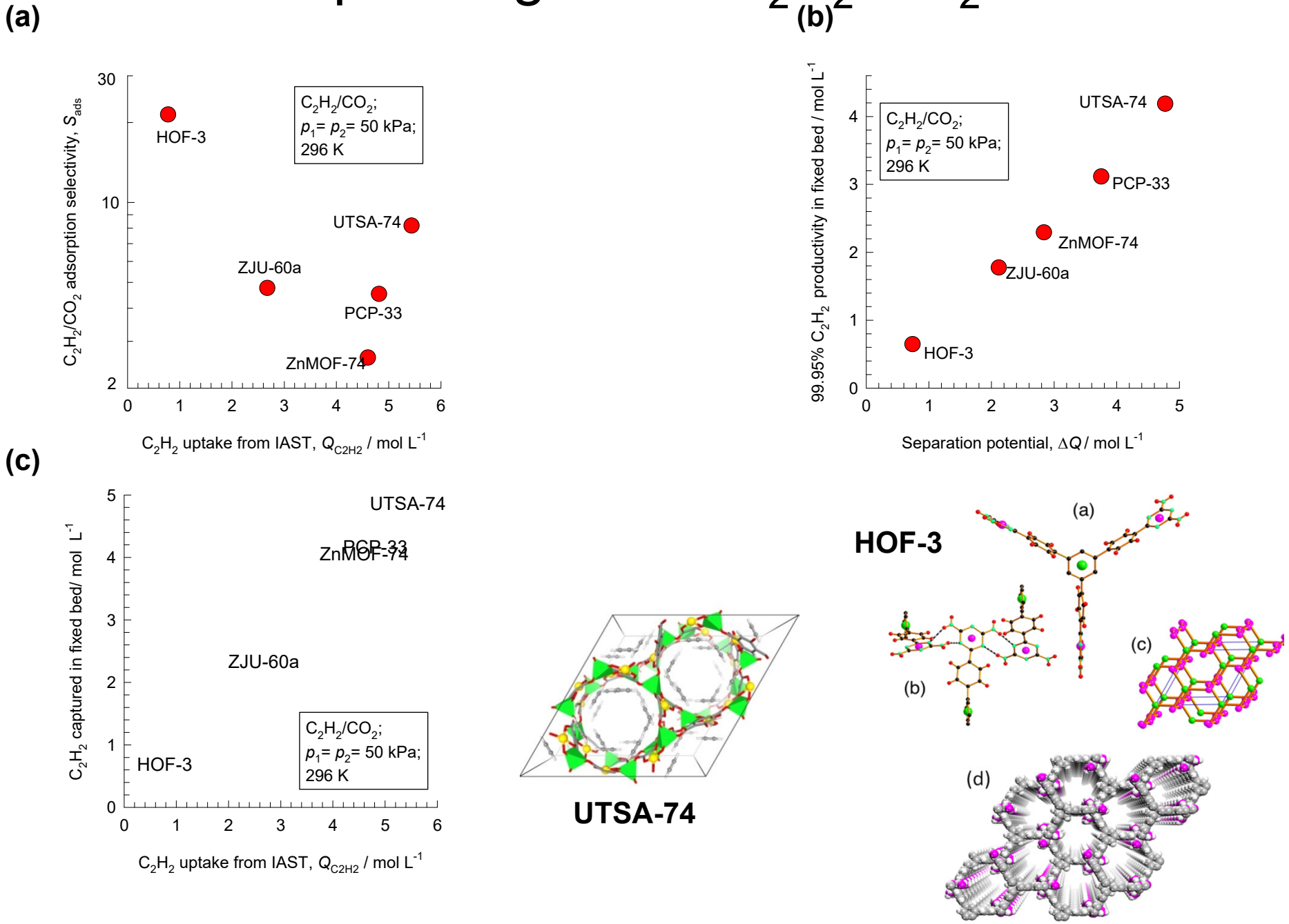

SIFSIX for separation of C_2H_2/C_2H_4

Figure S15

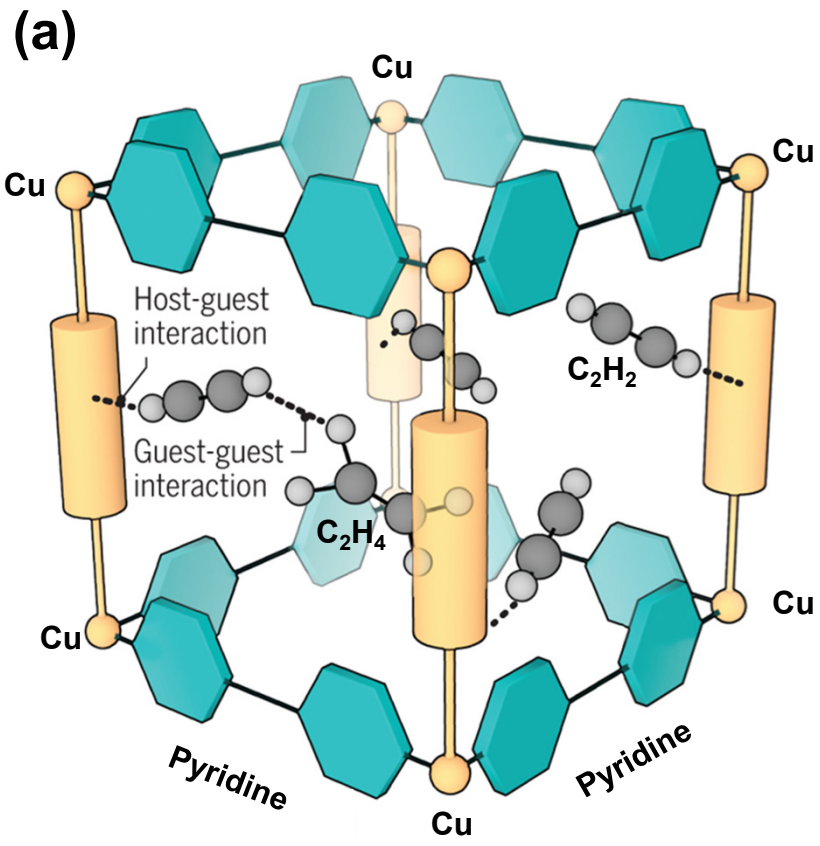

SIFSIX-1-Cu

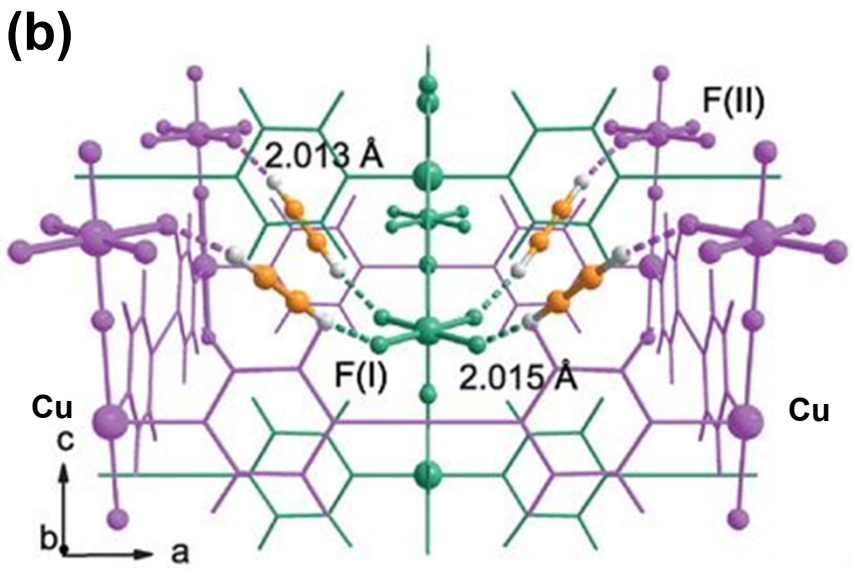

SIFSIX-2-Cu-i

Figure S16

Separating 1/99 C_2H_2/C_2H_4

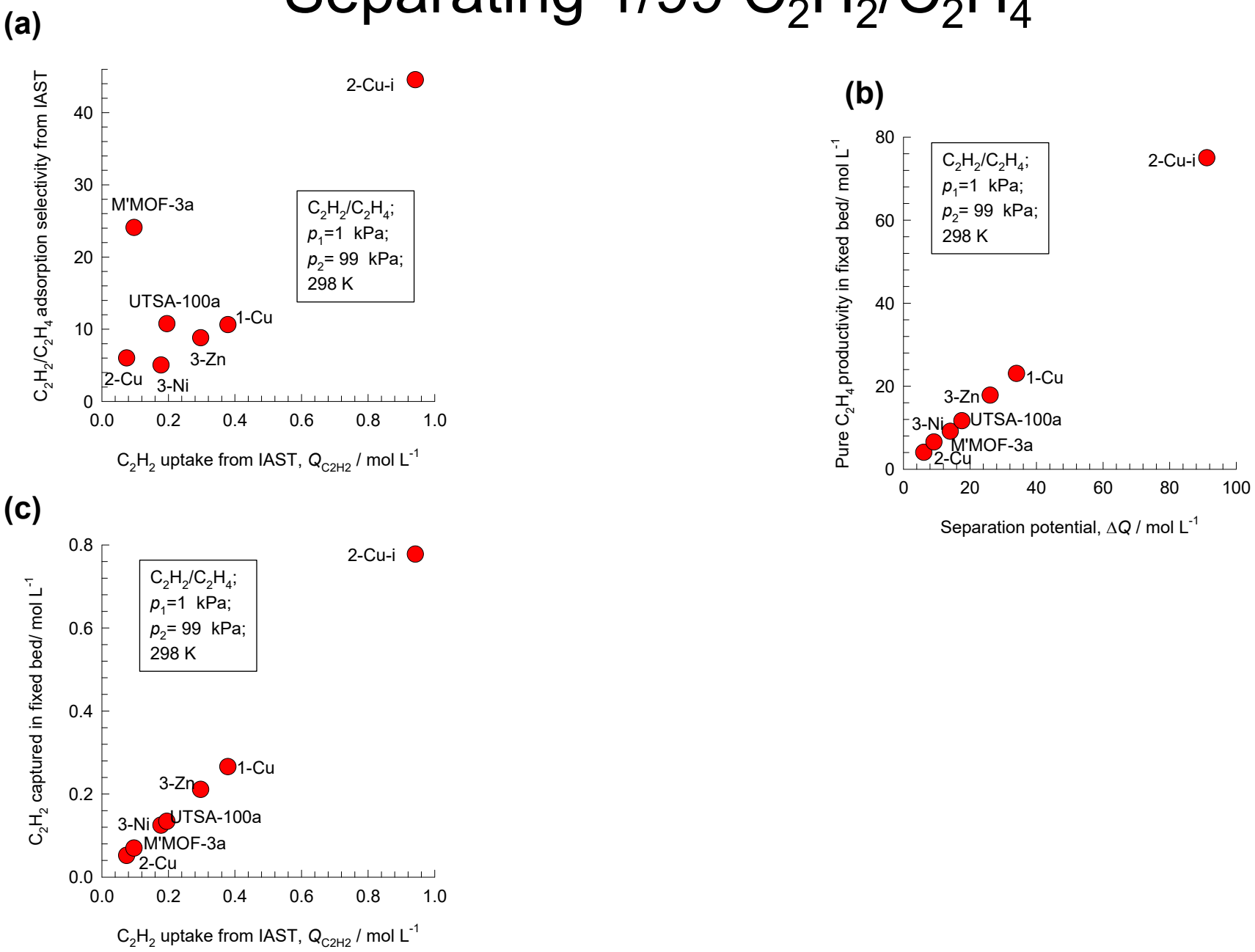

Figure S17

Separating 50/50 C_2H_2/C_2H_4

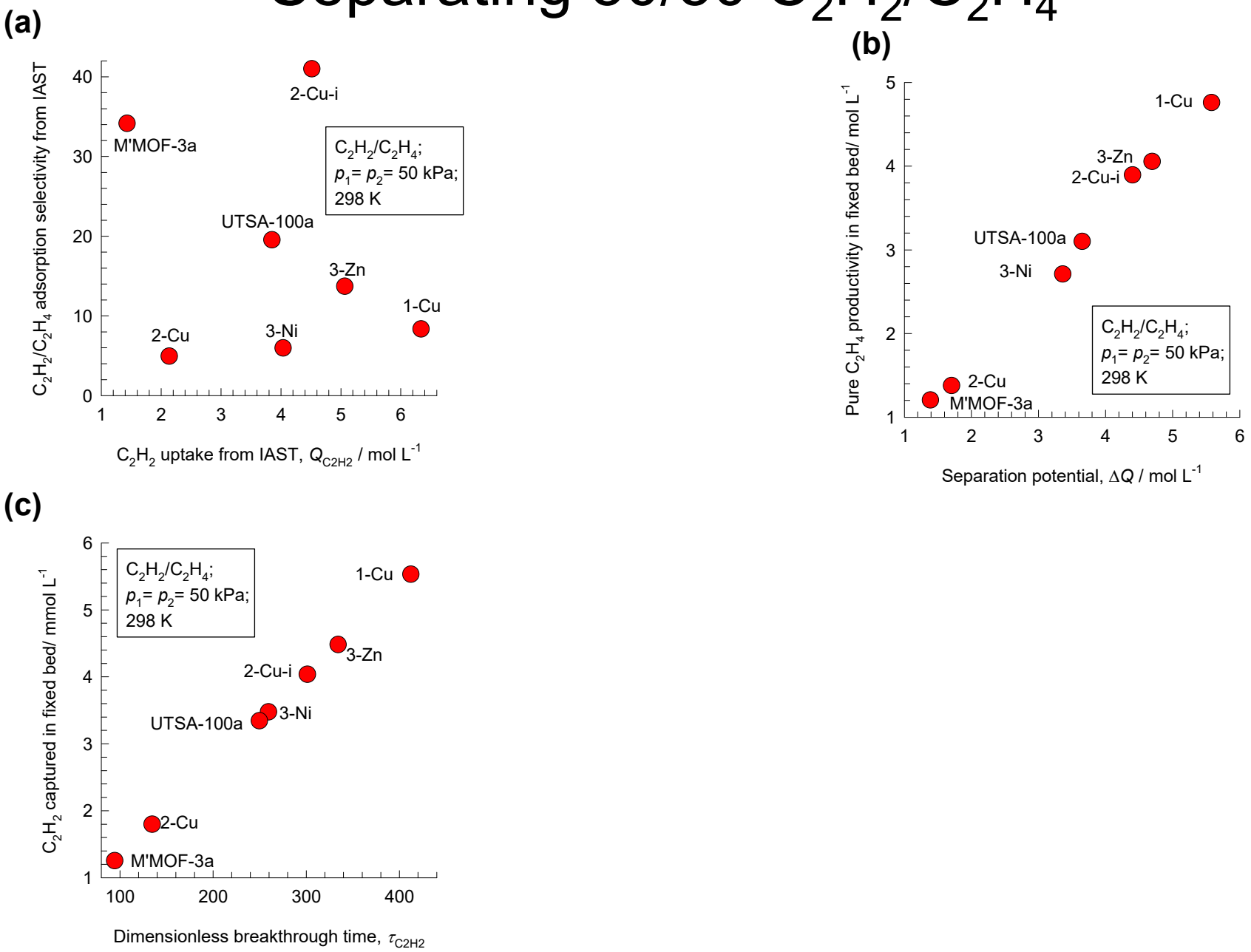

Figure S18

C_2H_4/C_2H_6 with CoMOF-74

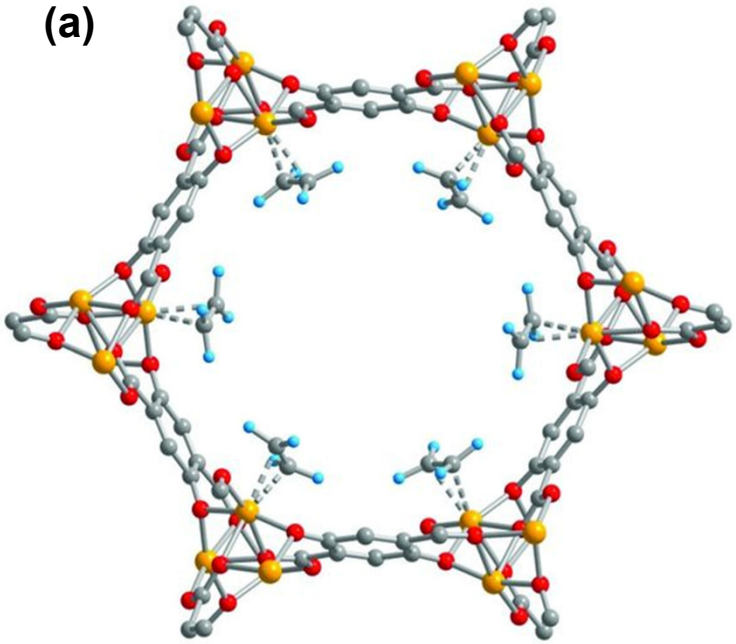

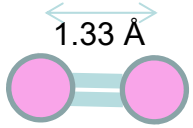

ethene
bp = 169.5 K

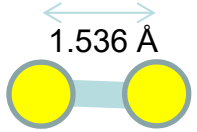

ethane
bp = 184.6 K

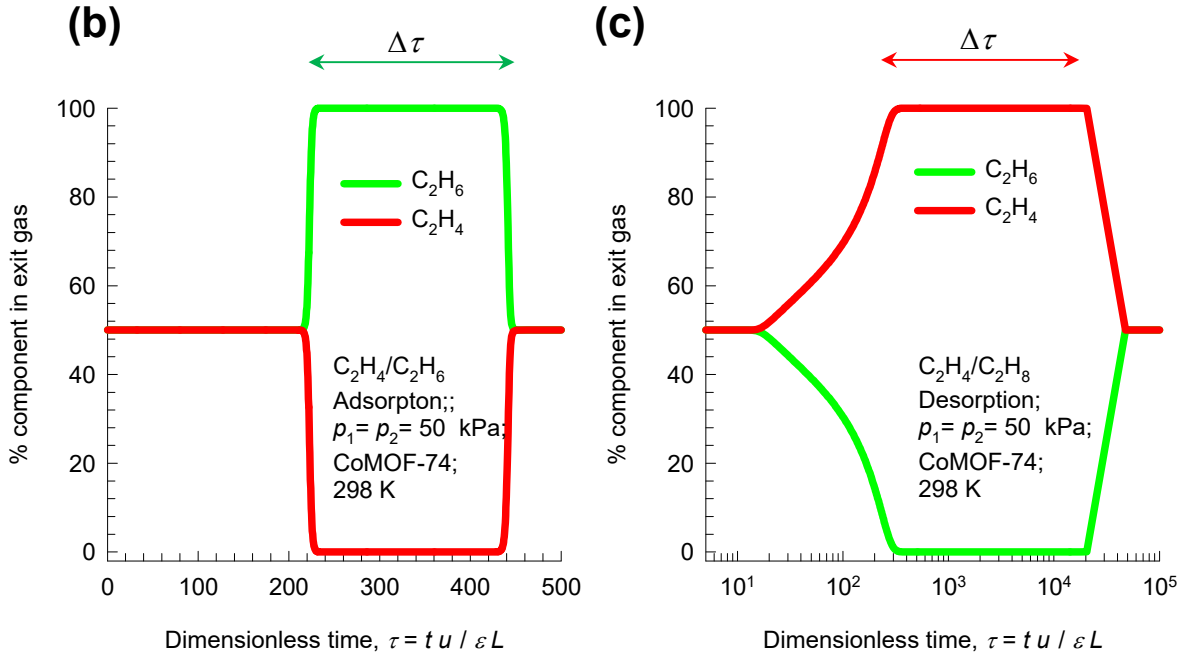

Figure S19

C_3H_6/C_3H_8 with KAUST-7

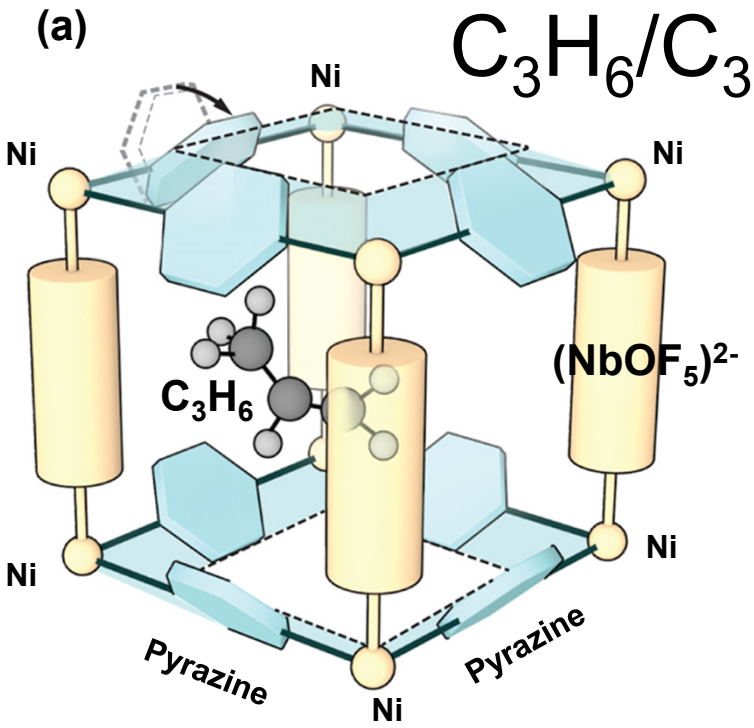

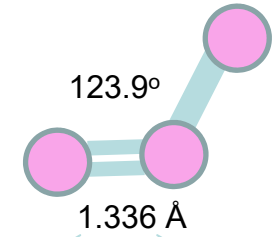

propene
bp = 226 K

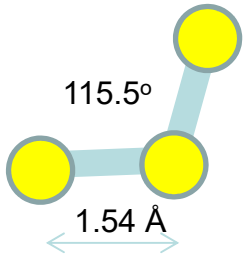

propane
bp = 231.3 K

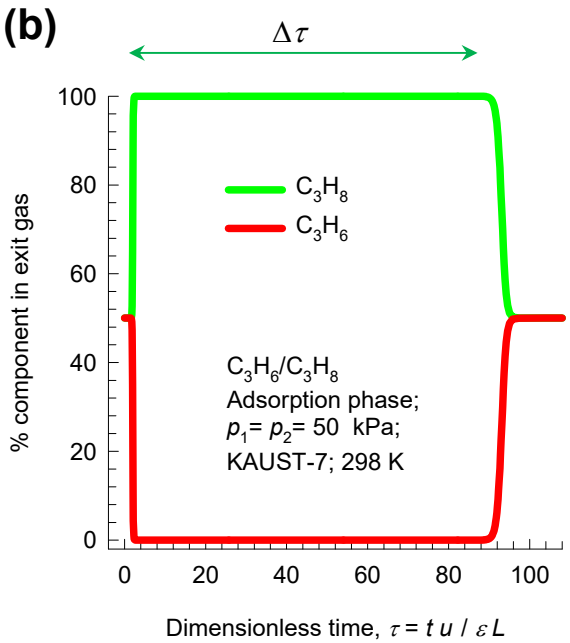

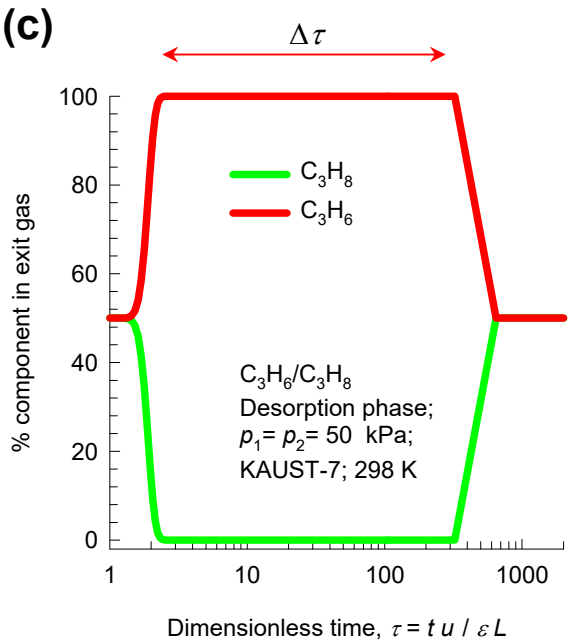

Figure S20

C_2H_4/C_2H_6 separations

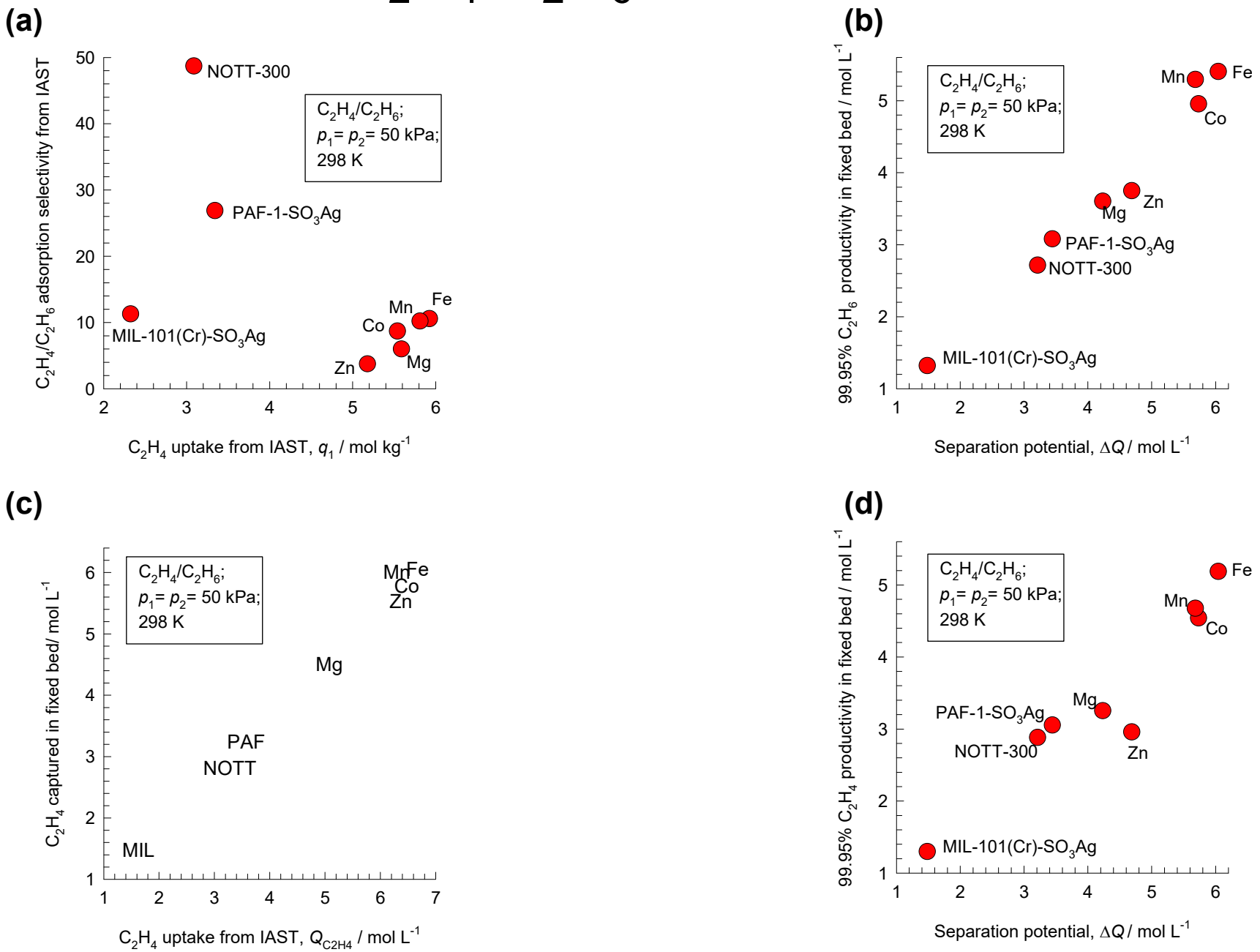

Figure S21

C_3H_6/C_3H_8 separations

(a)

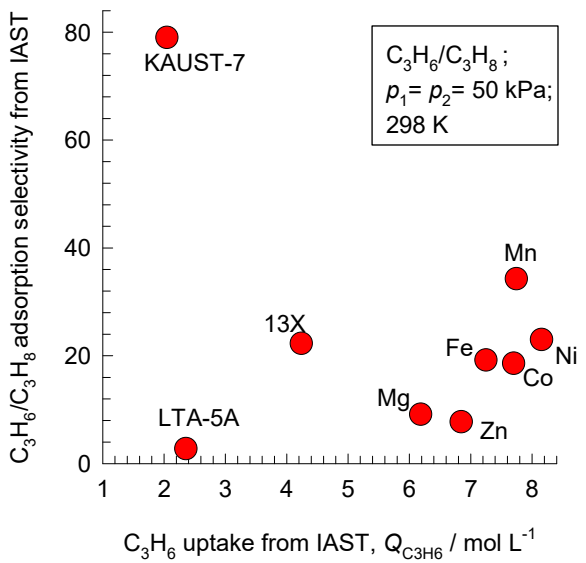

(b)

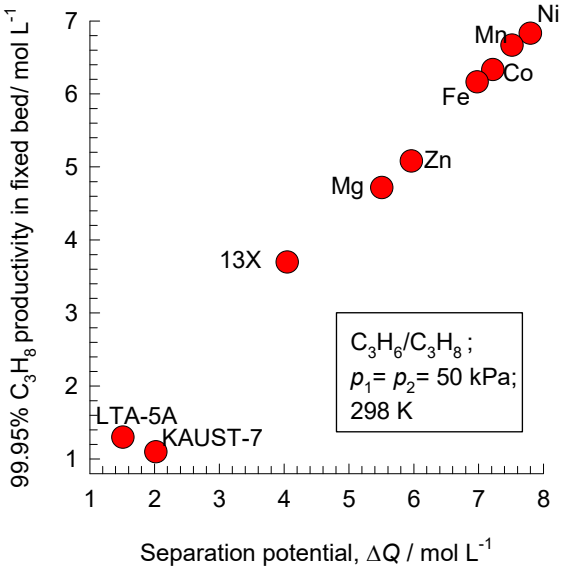

(c)

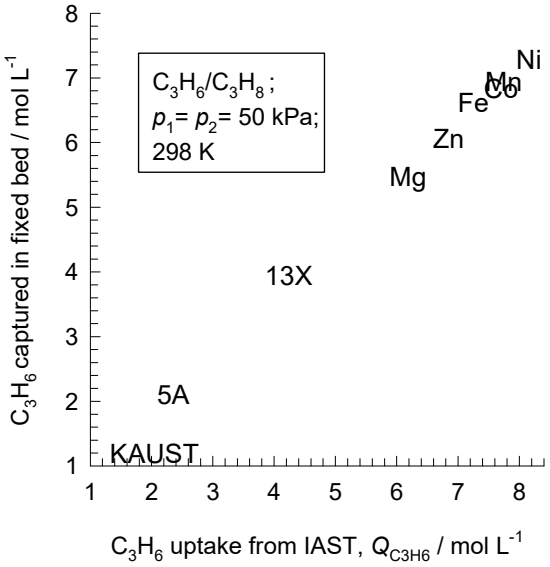

Figure S22

CO_2/CH_4 separations

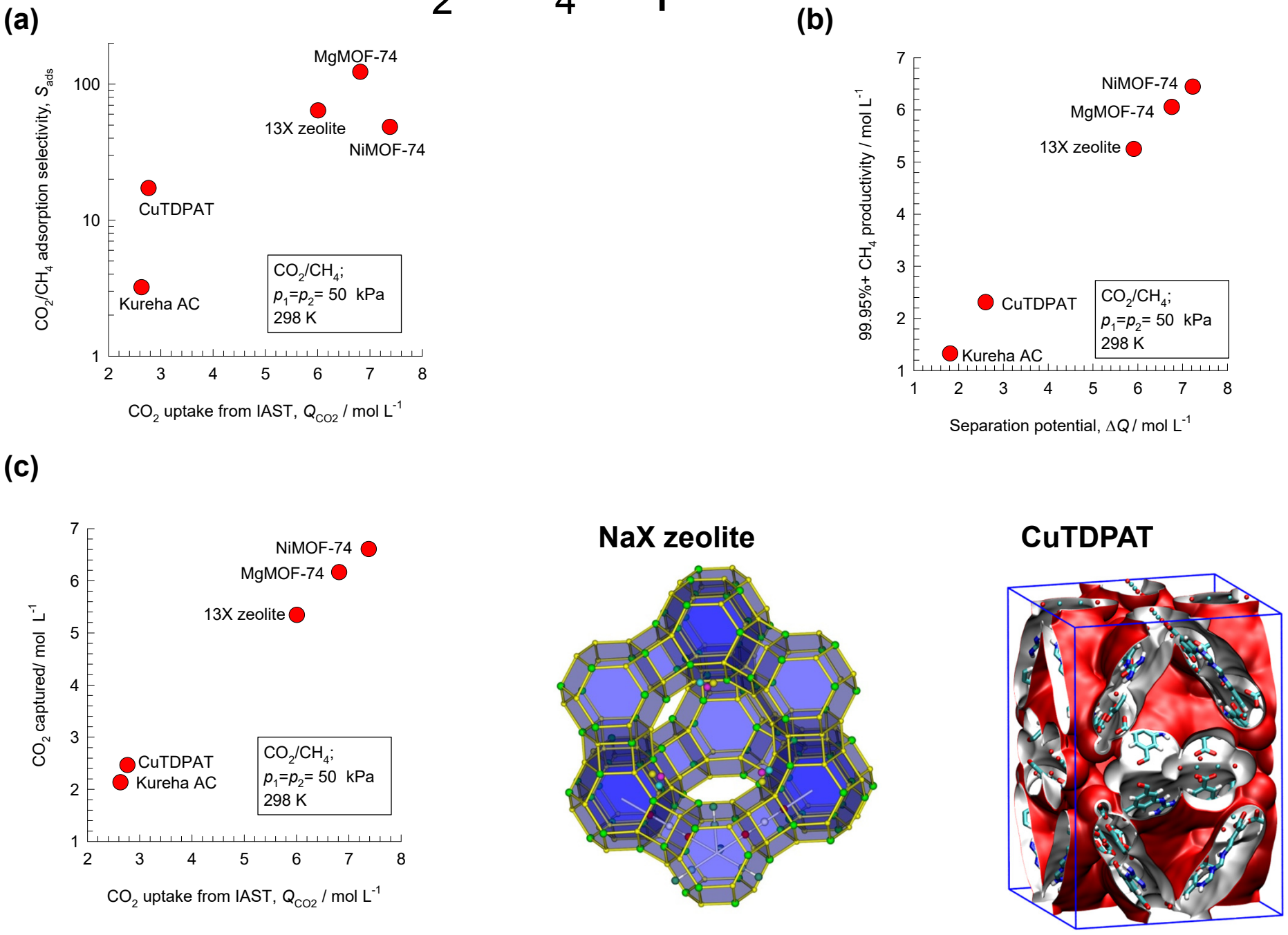

Figure S23

CO_2 attaches to Mg in MgMOF-74 via one O atom

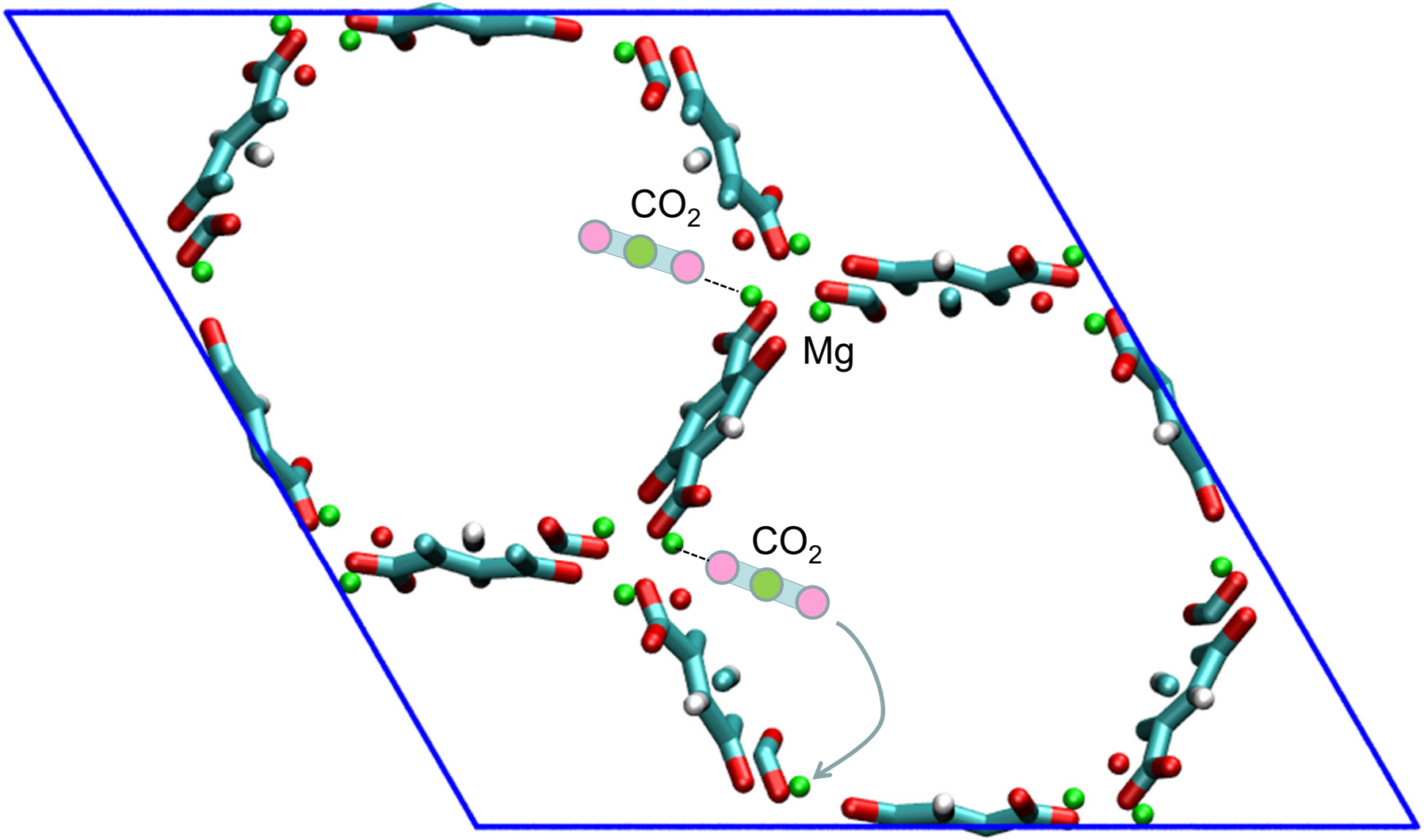

Figure S24

CO_2/CH_4 separations

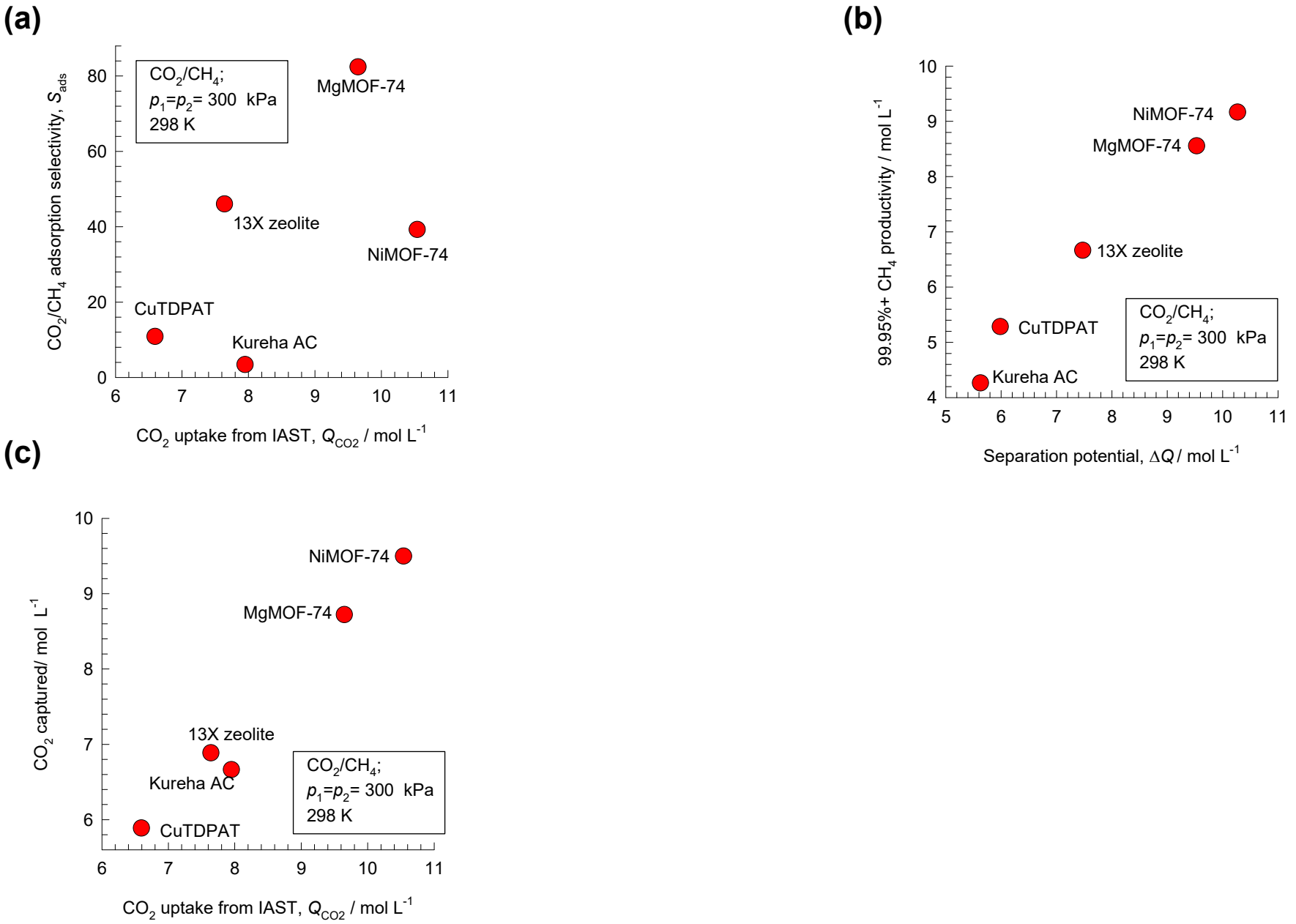

Productivity vs Displacement Interval

Figure S25

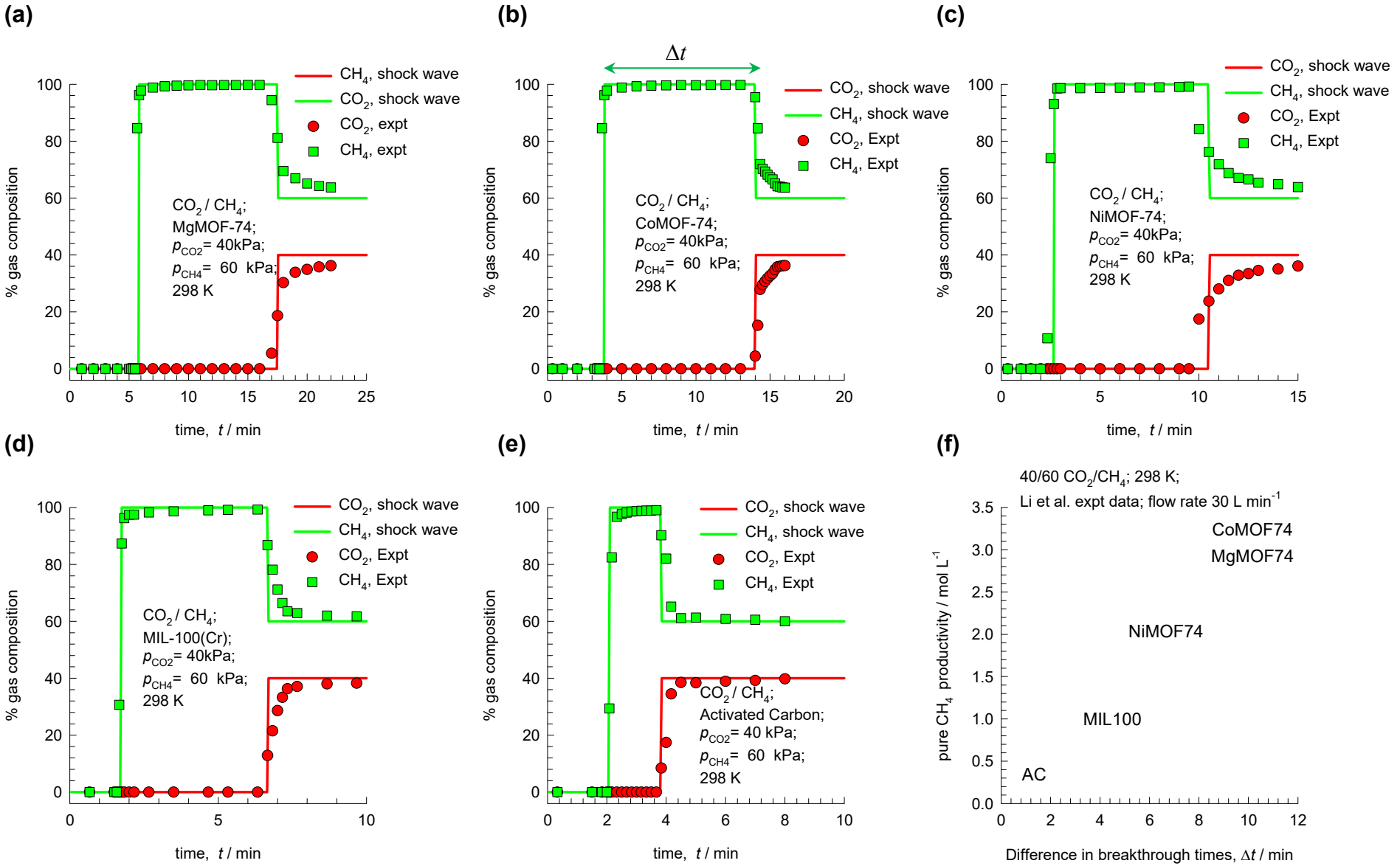

Productivity vs Displacement Interval

Figure S26

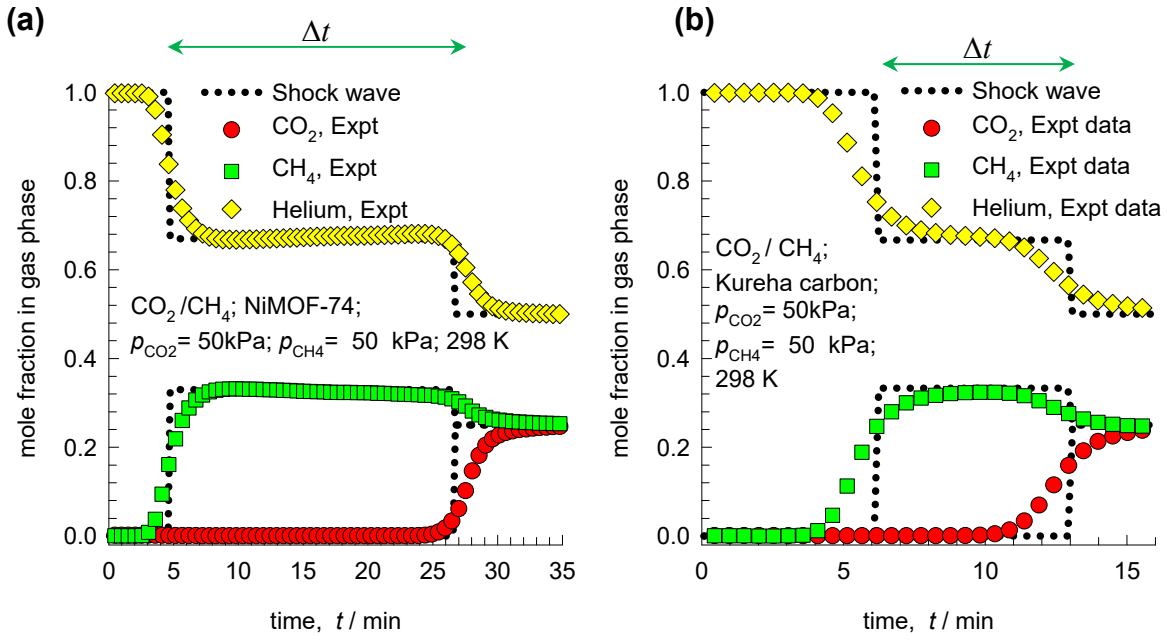

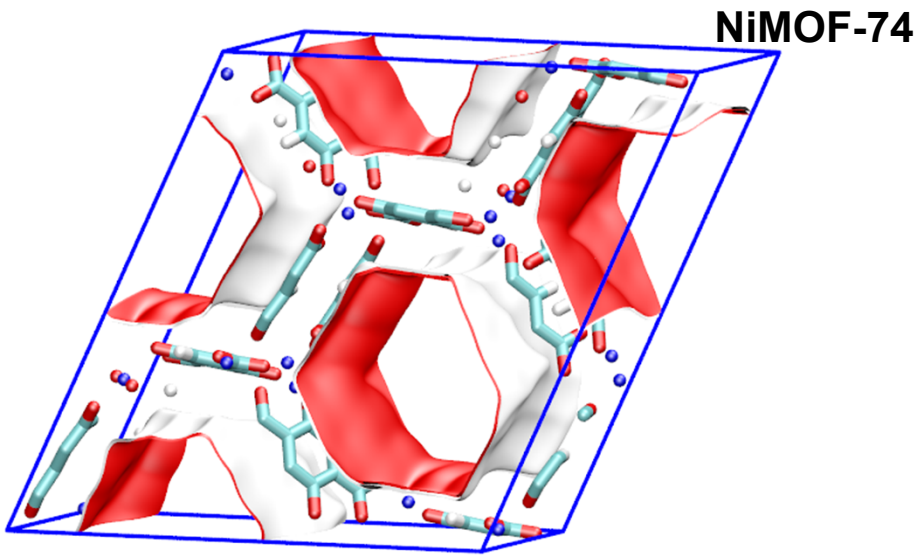

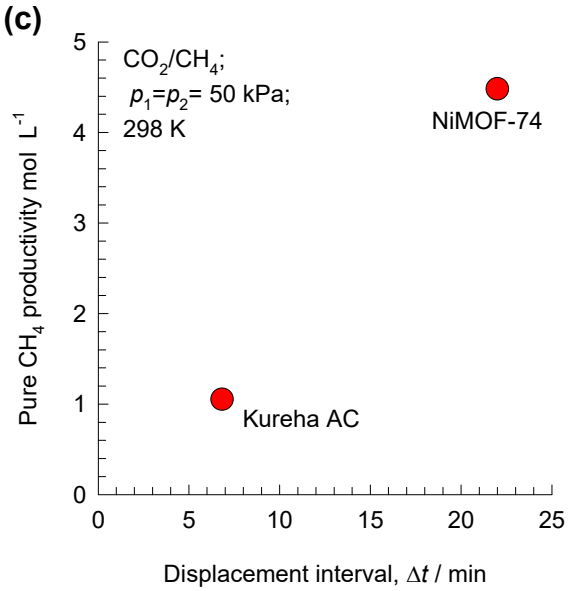

Figure S27

15/85 CO_2/N_2 separations

(a)

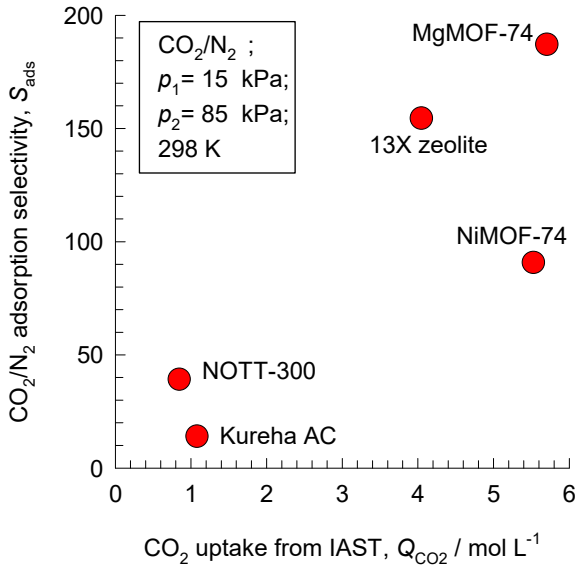

(b)

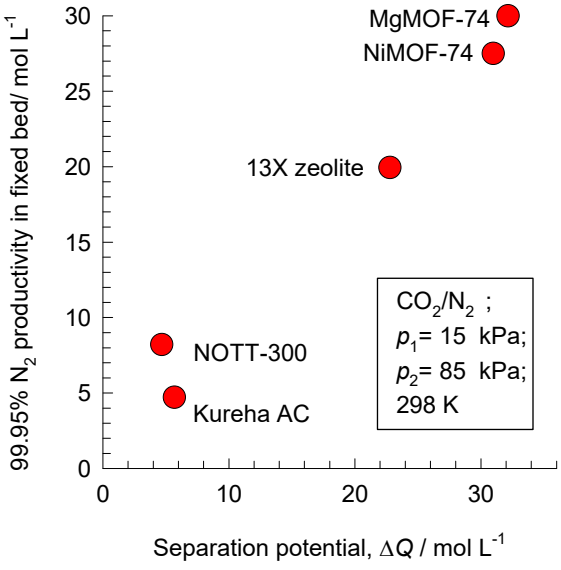

13X= NaX zeolite

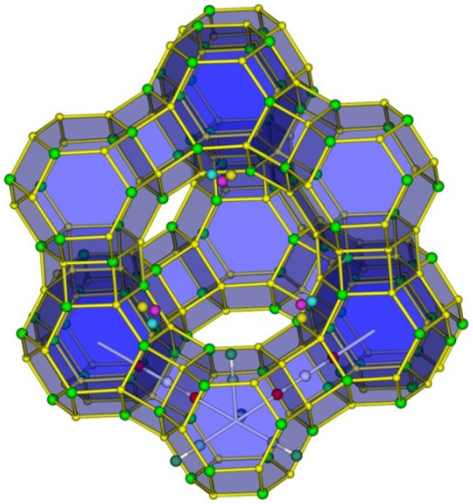

MgMOF-74

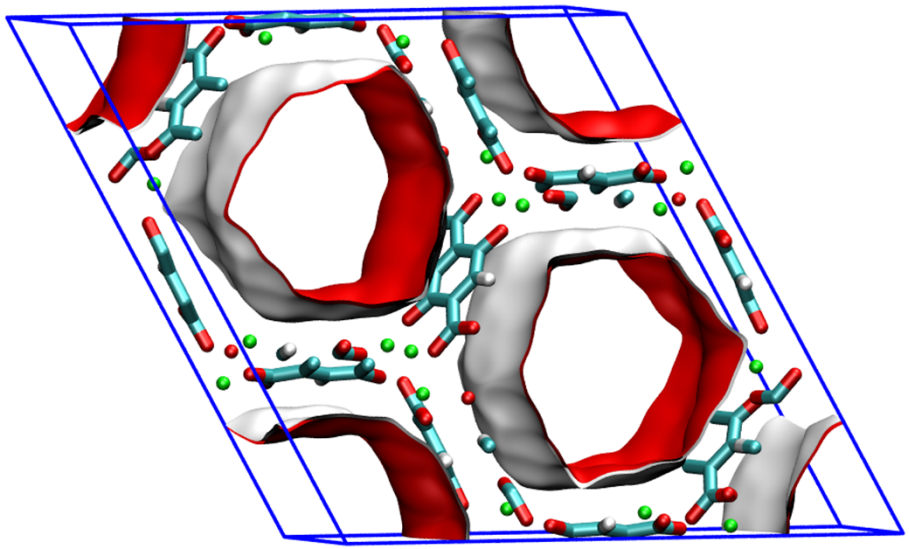

20/80 CO_2/H_2 separations

Figure S28

(a)

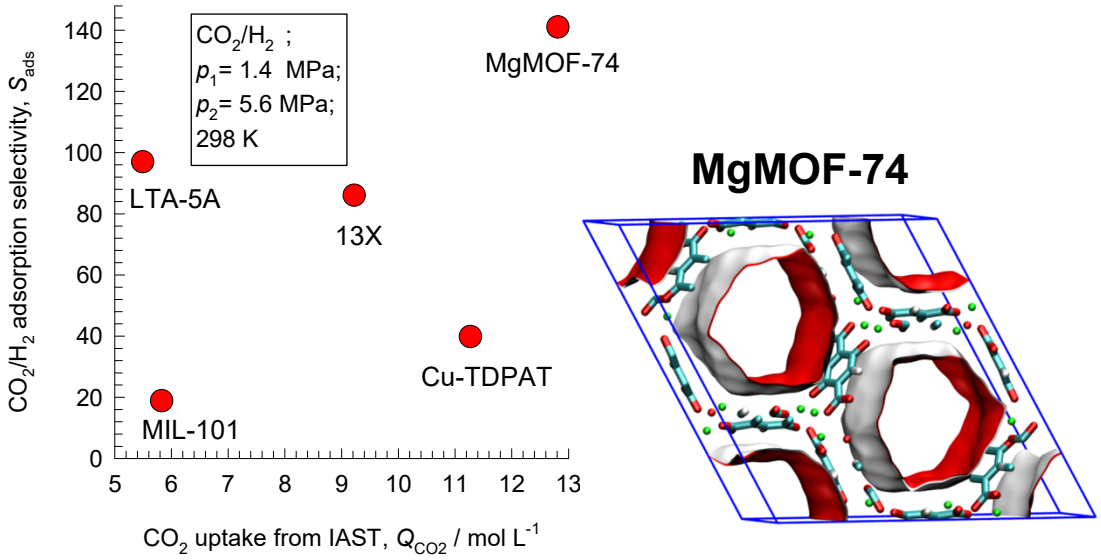

MgMOF-74

(b)

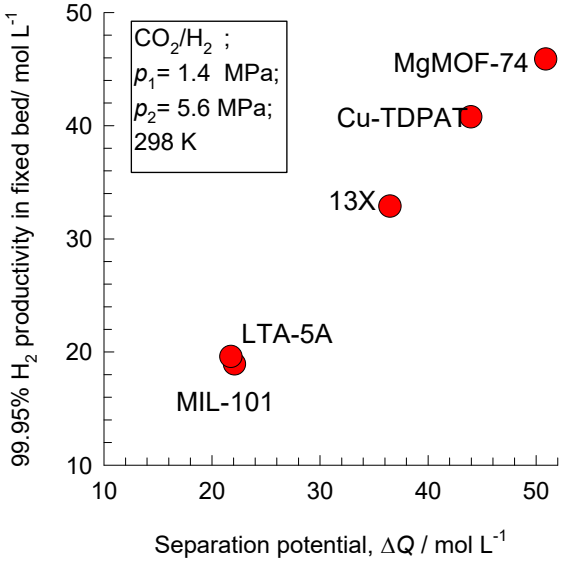

LTA-5A zeolite

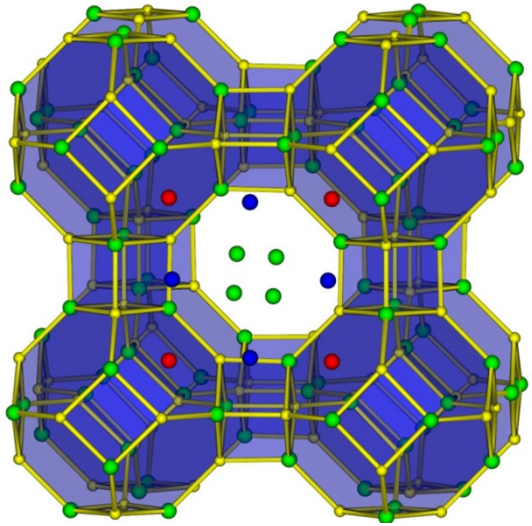

13X= NaX zeolite

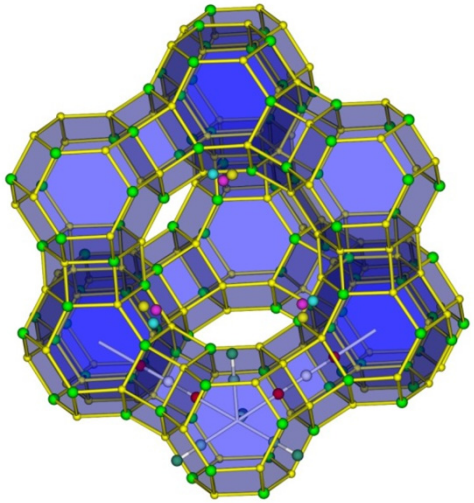

Cu-TDPAT

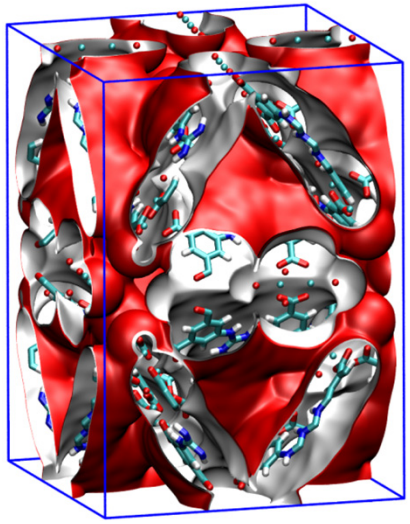

40/10/50 $CO_2/CH_4/H_2$ separations

Figure S29

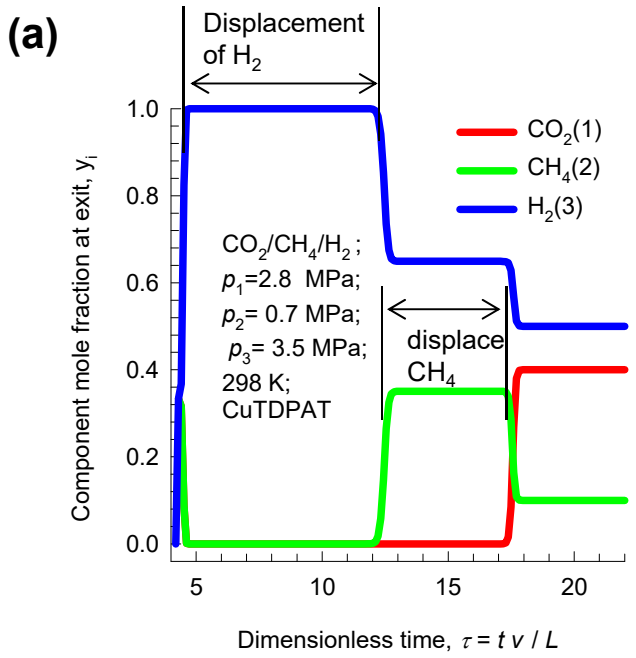

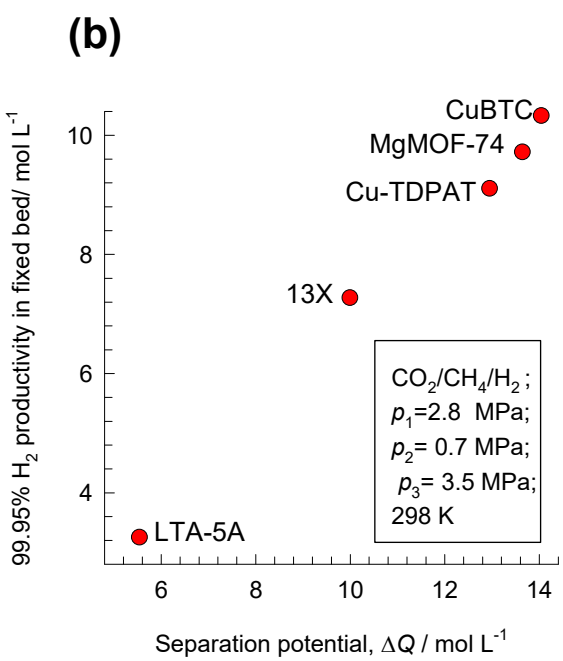

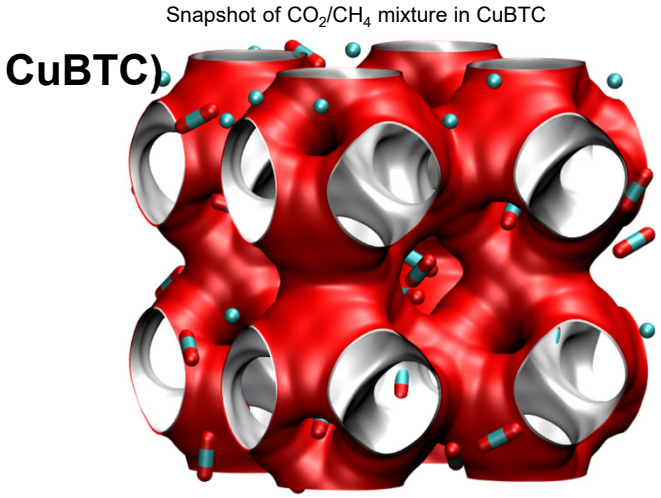

40/5/5/50 $CO_2/CO/CH_4/H_2$ separations

Figure S30

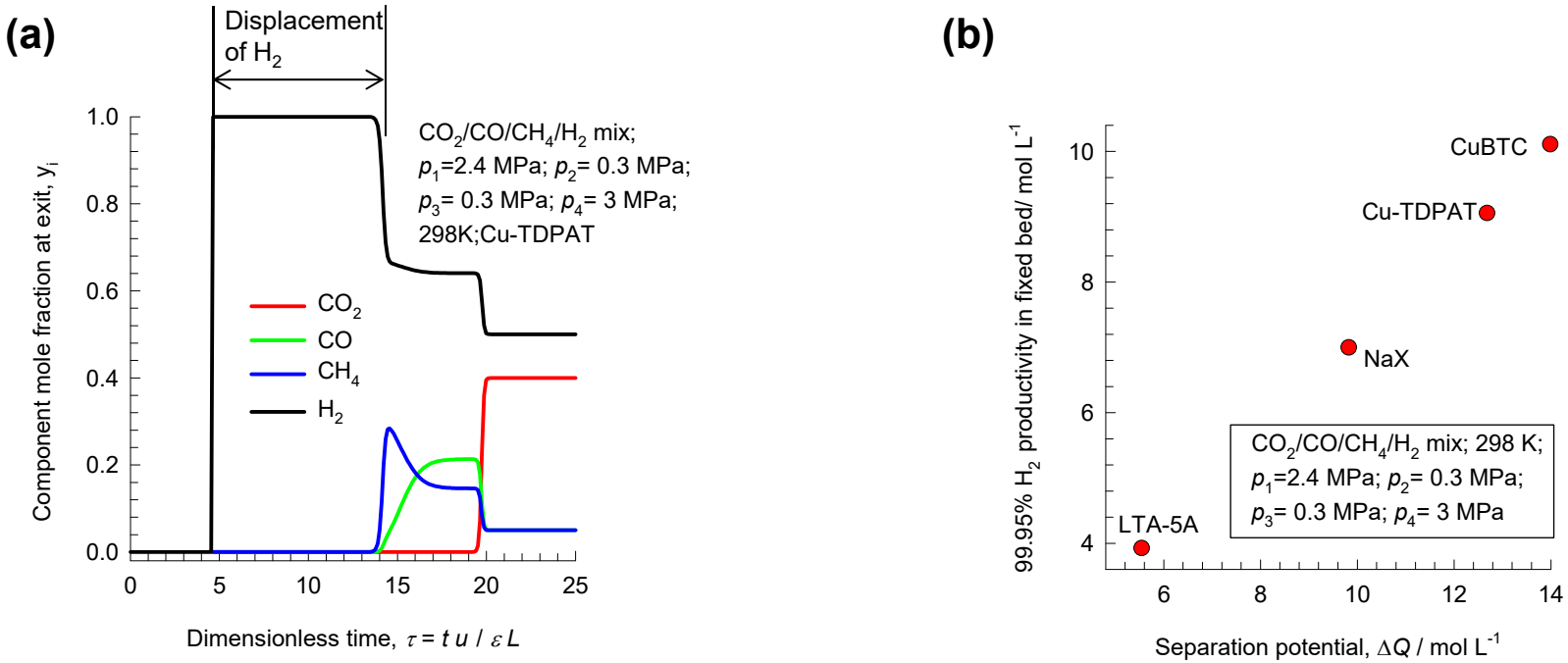

Figure S31

Separating pentane isomers

(a)

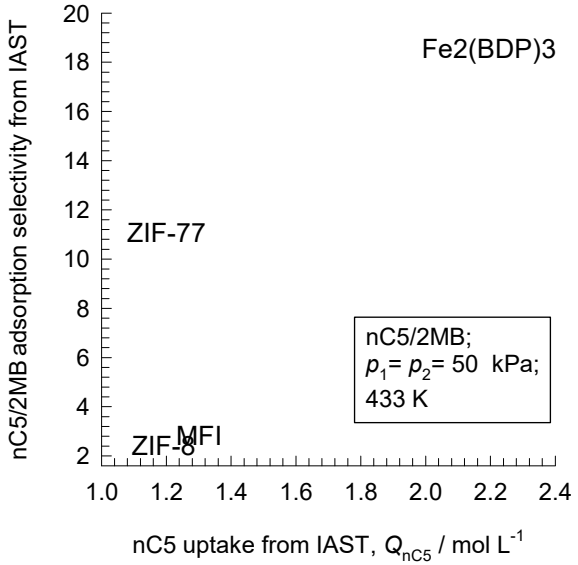

Intersecting channels of MFI zeolite.

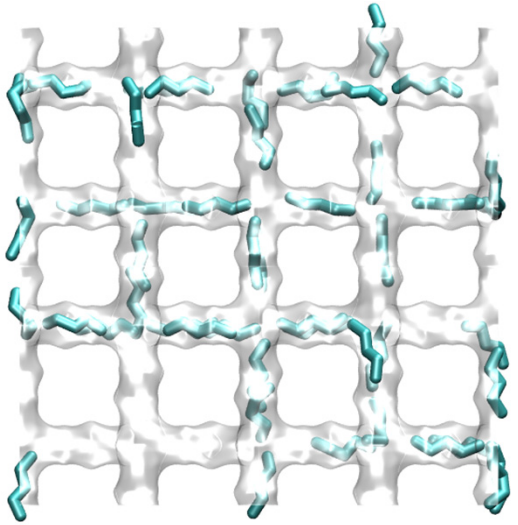

ZIF-8

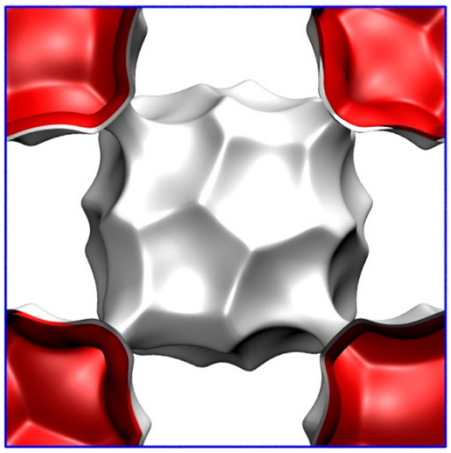

$Fe_2(BDP)_3$

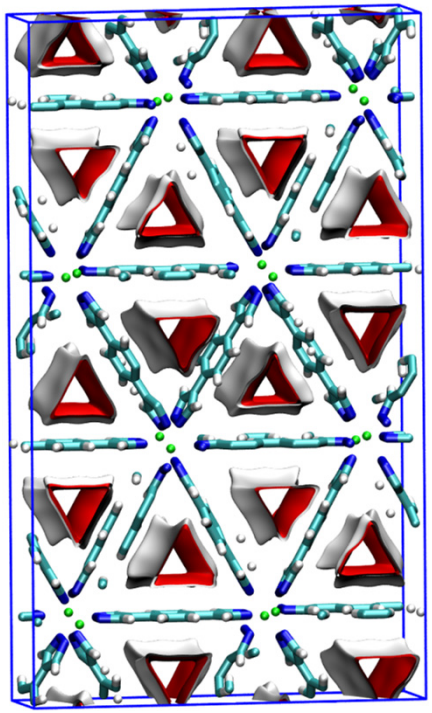

(b)

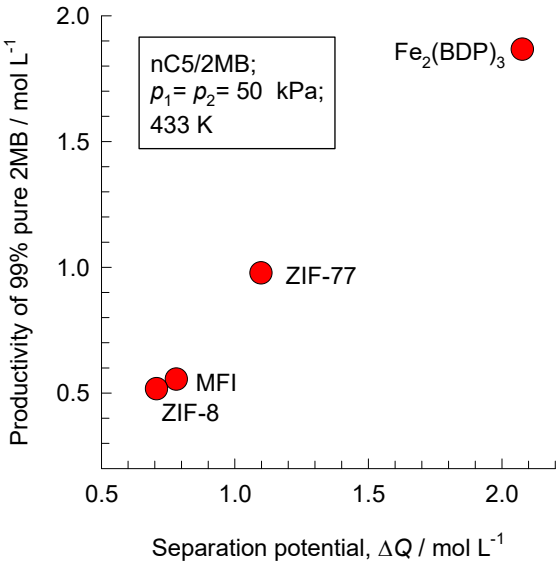

Figure S32

$Fe_2(BDP)_3$ snapshots of C5, C6 isomers

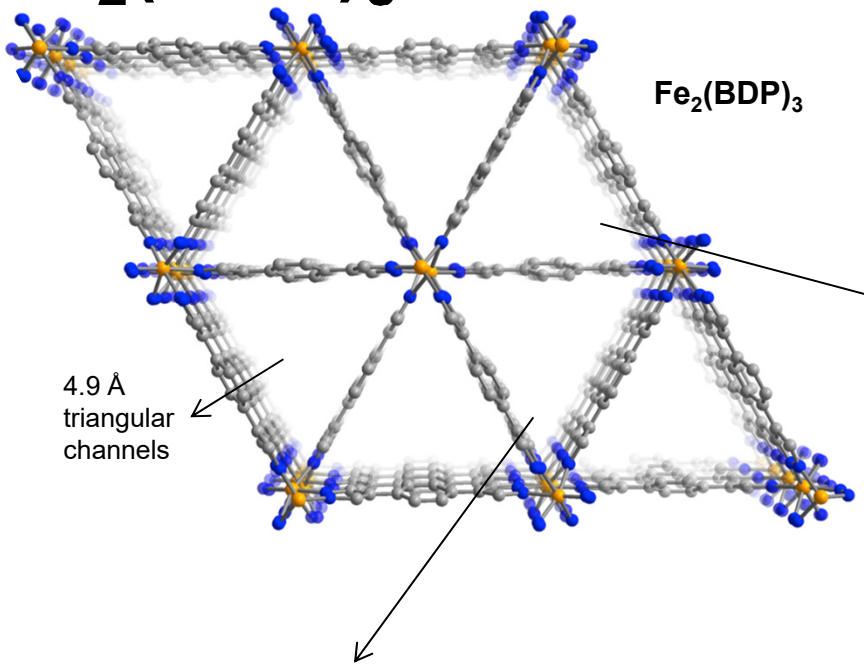

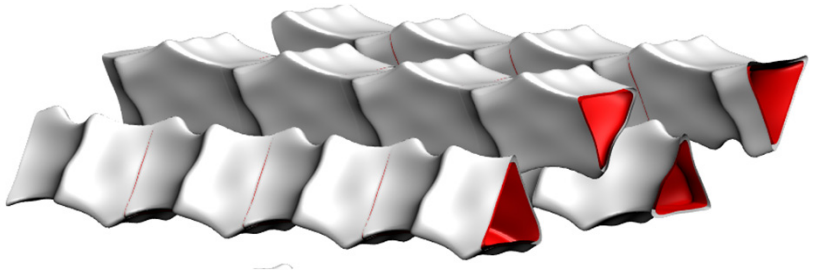

Side-view of C6 isomers in the gutters

Side-view of C5 isomers in the gutters

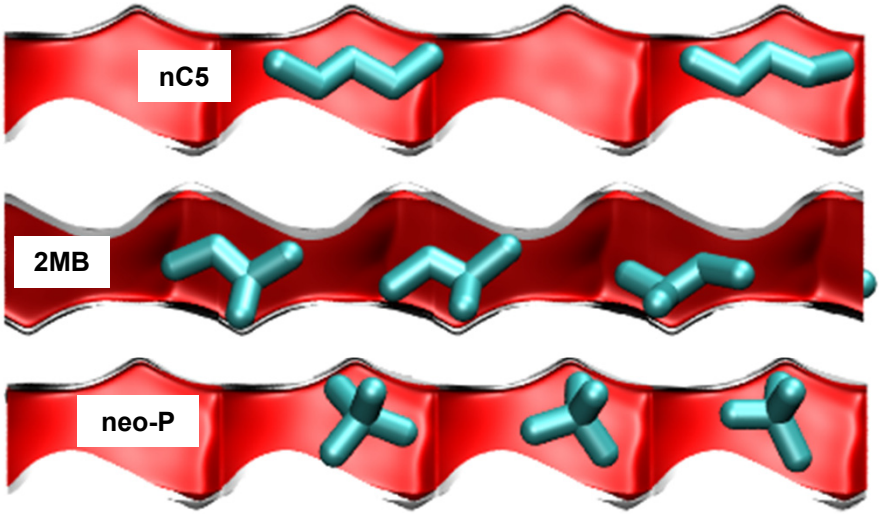

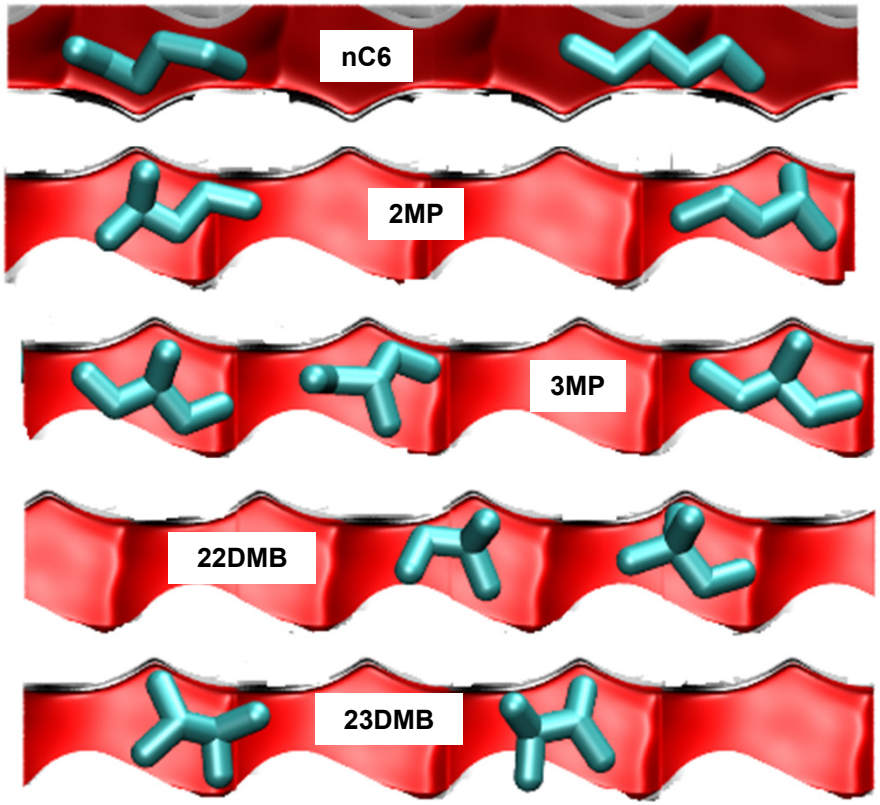

Figure S33

Separating hexanes

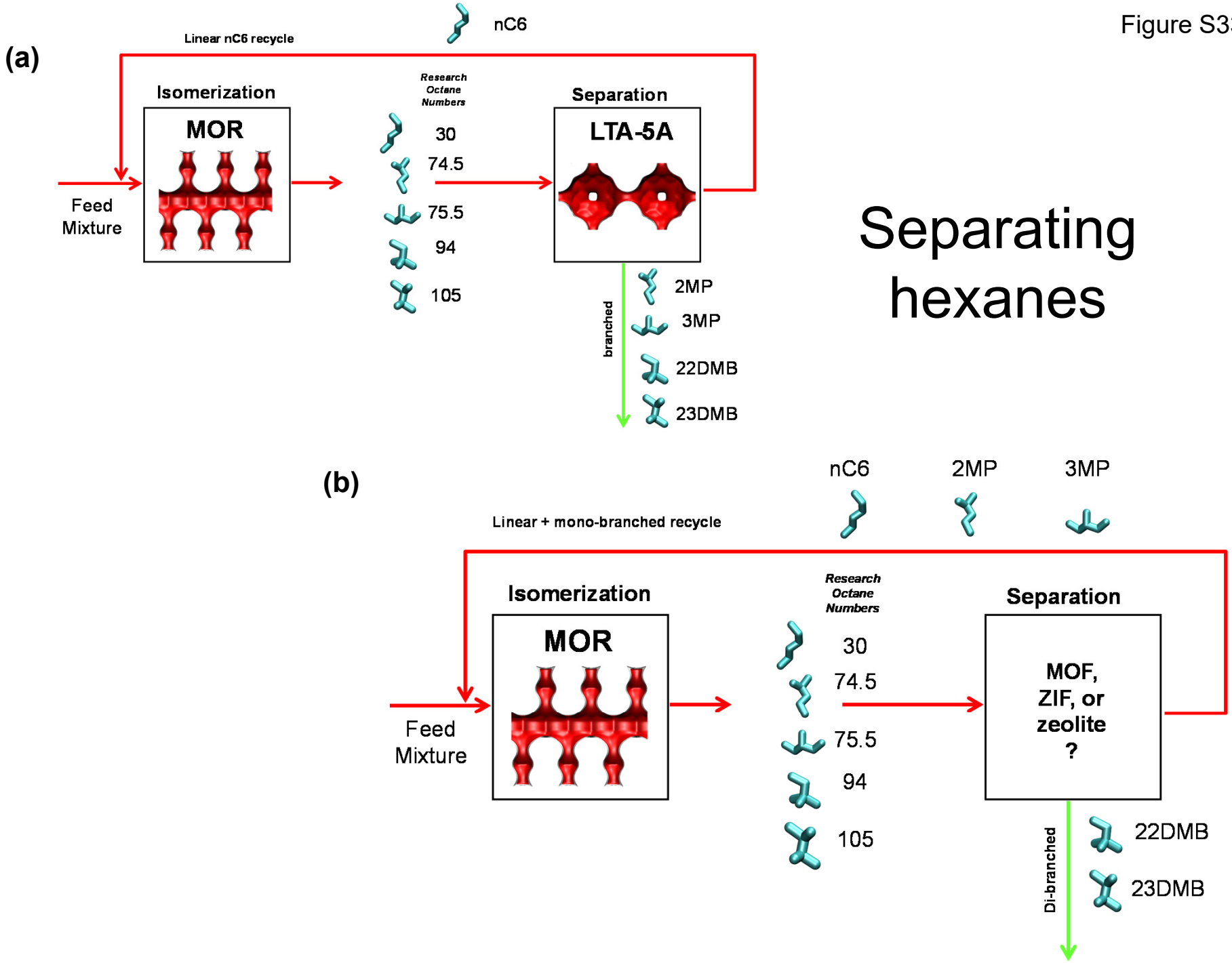

Figure S34

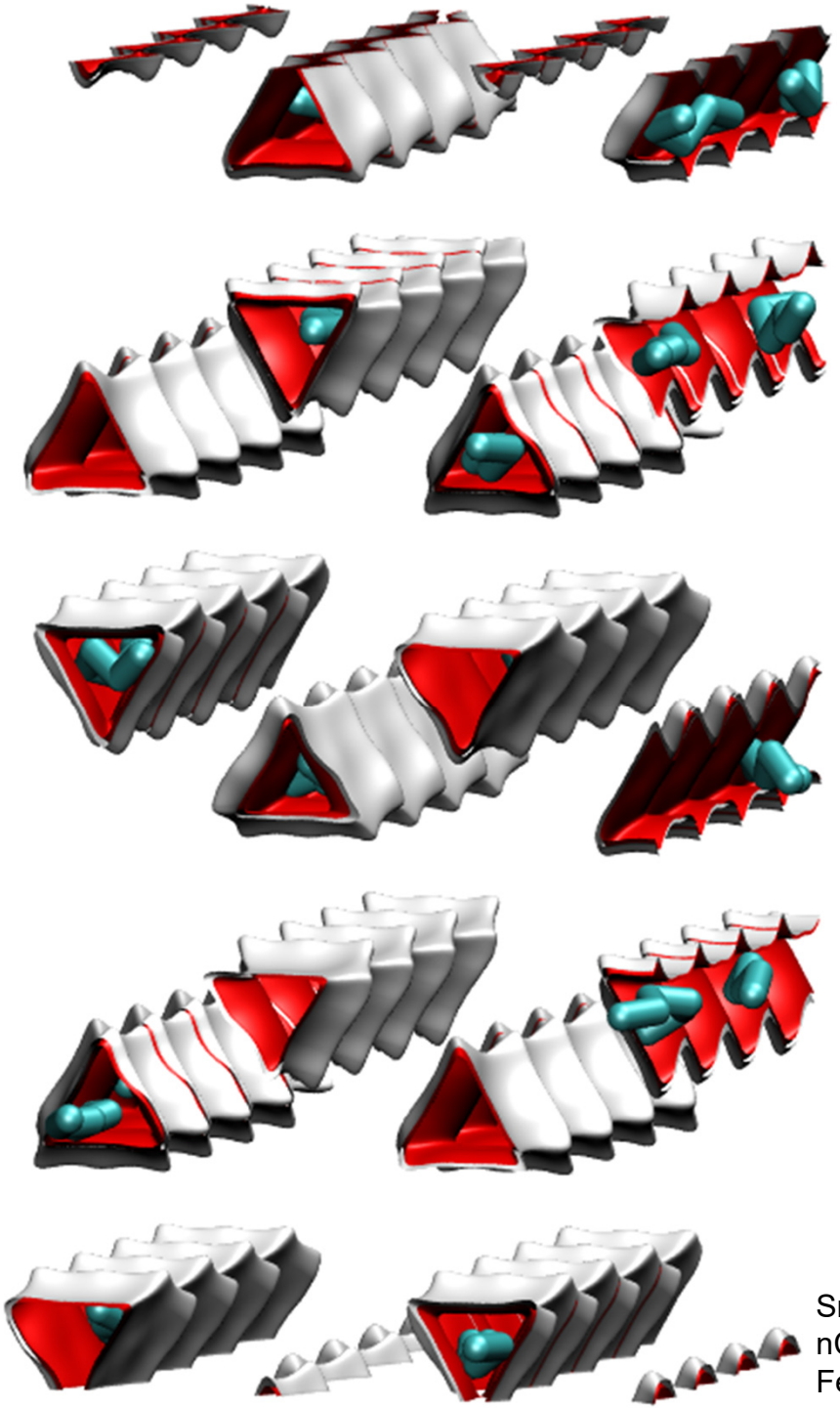

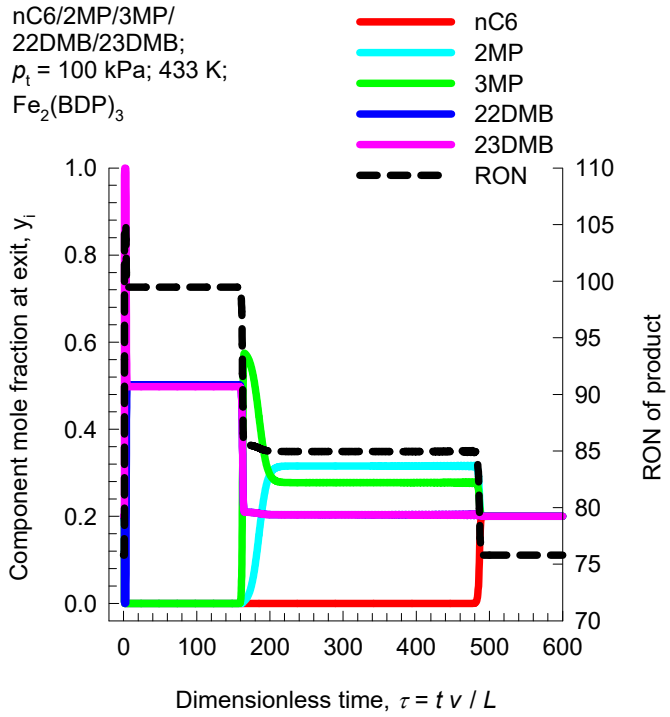

Snapshots showing the location of nC6 within the triangular channels of $Fe_2(BDP)_3$.

Figure S35

Hexane isomers breakthrough in ZIF-77

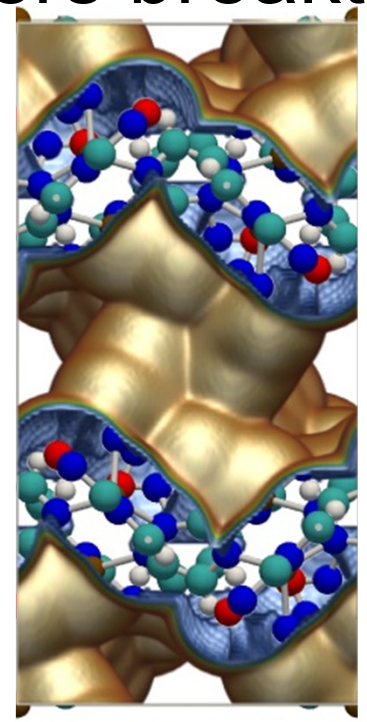

Pore landscape of ZIF-77

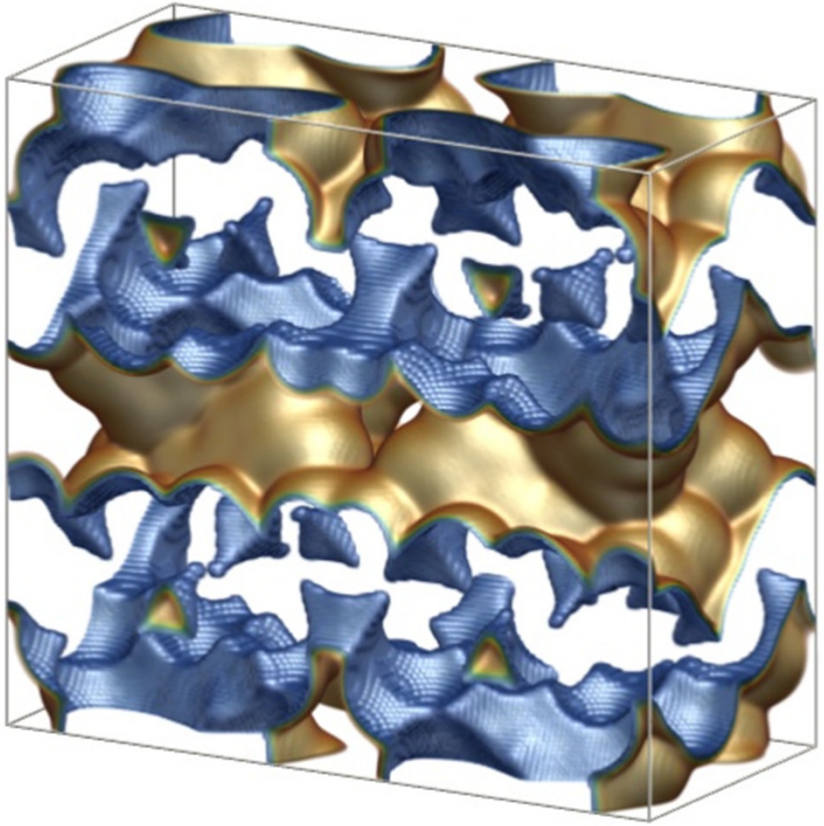

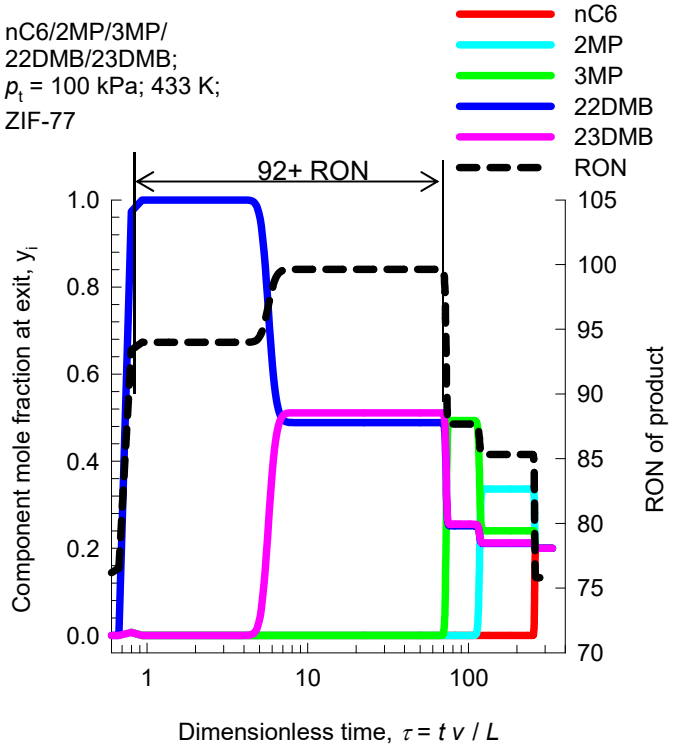

Figure S36

Hexane isomers breakthrough in MFI

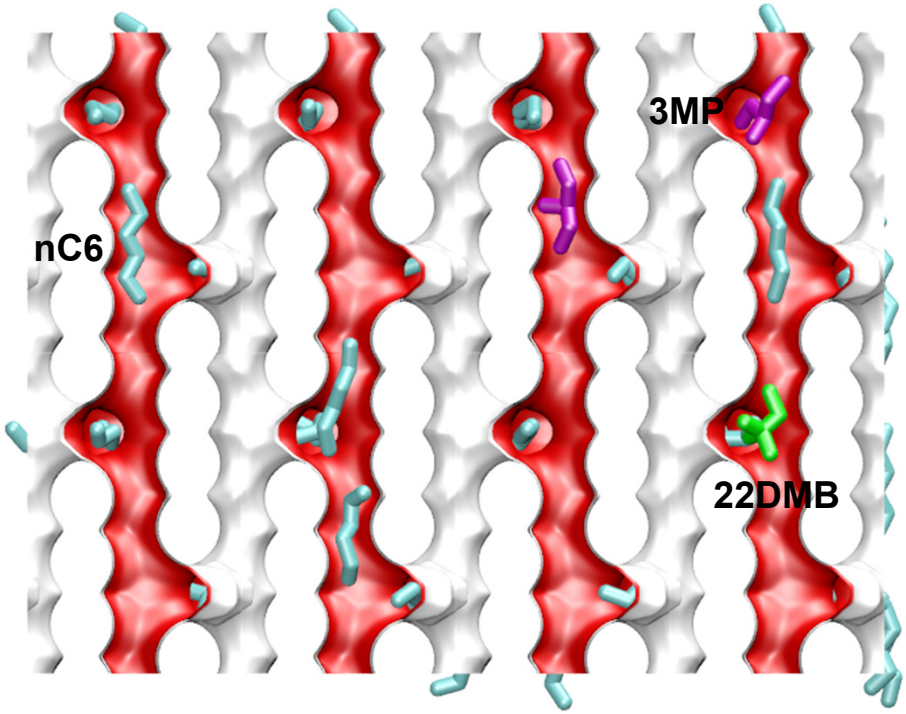

Snapshots showing the location of nC6, 3MP, and 22DMB within the intersecting channels of MFI.

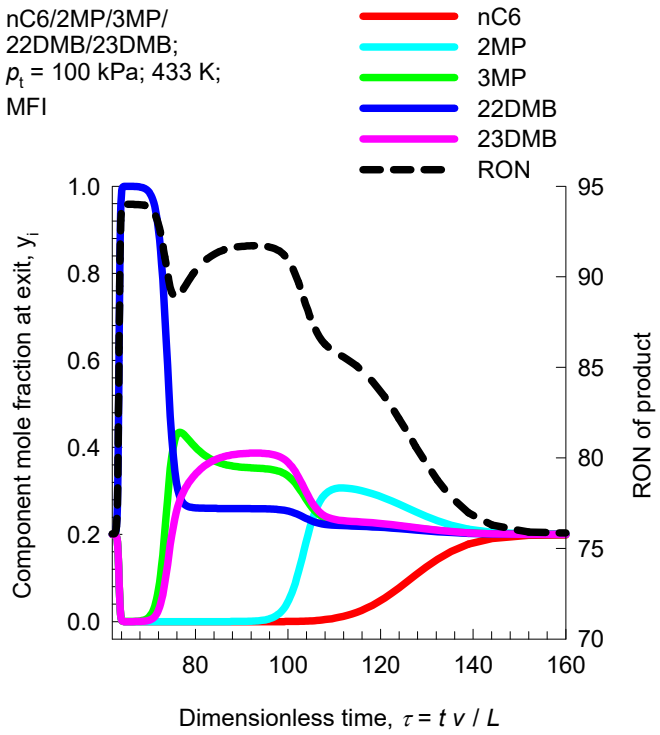

Breakthrough simulations for Co(BDP)

Figure S37

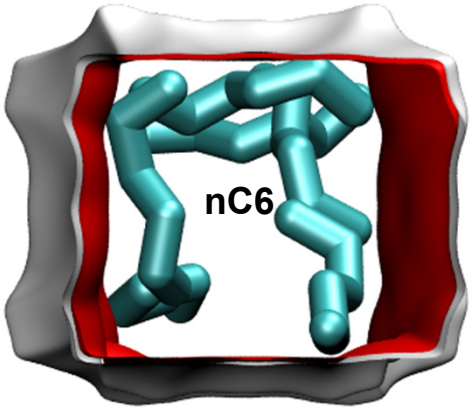

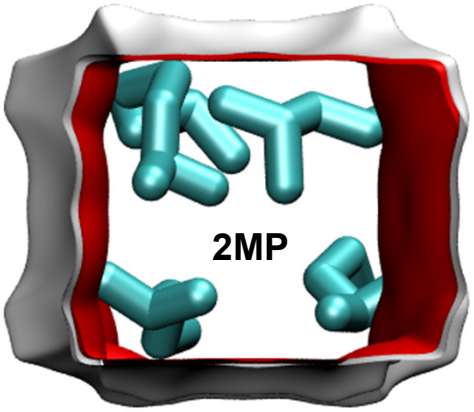

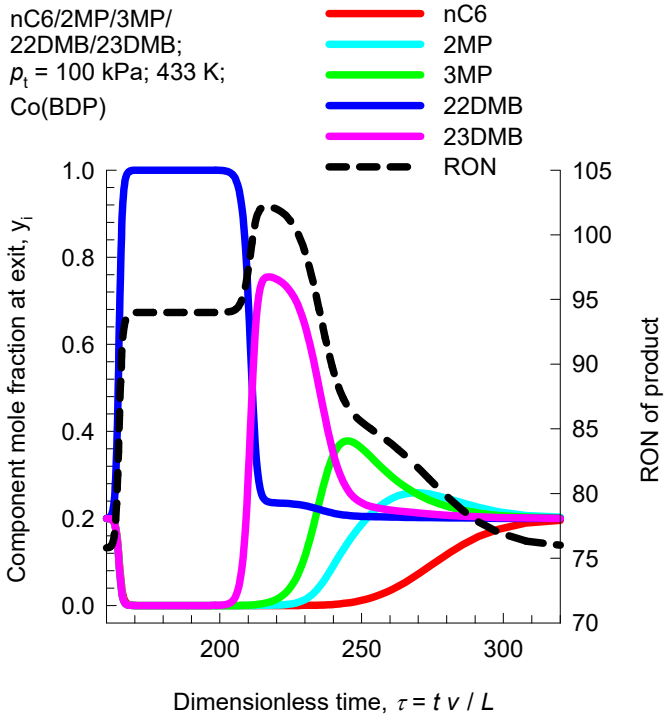

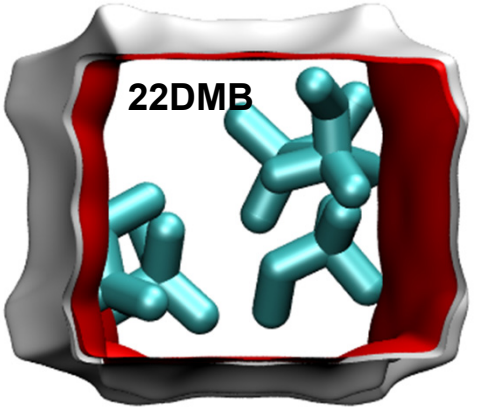

Breakthrough simulations for MgMOF-74

Figure S38

nC6

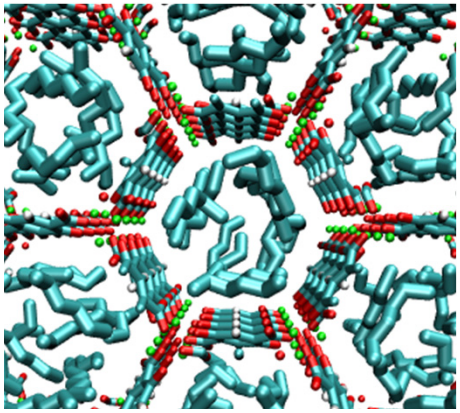

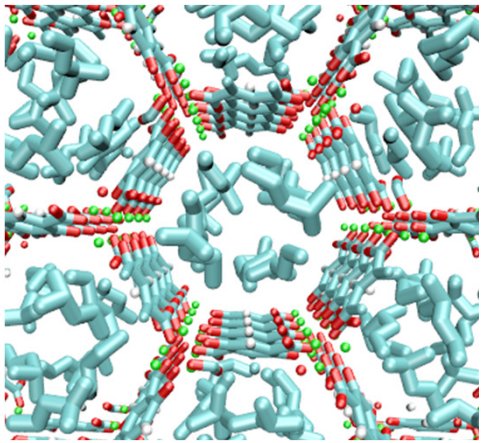

2MP

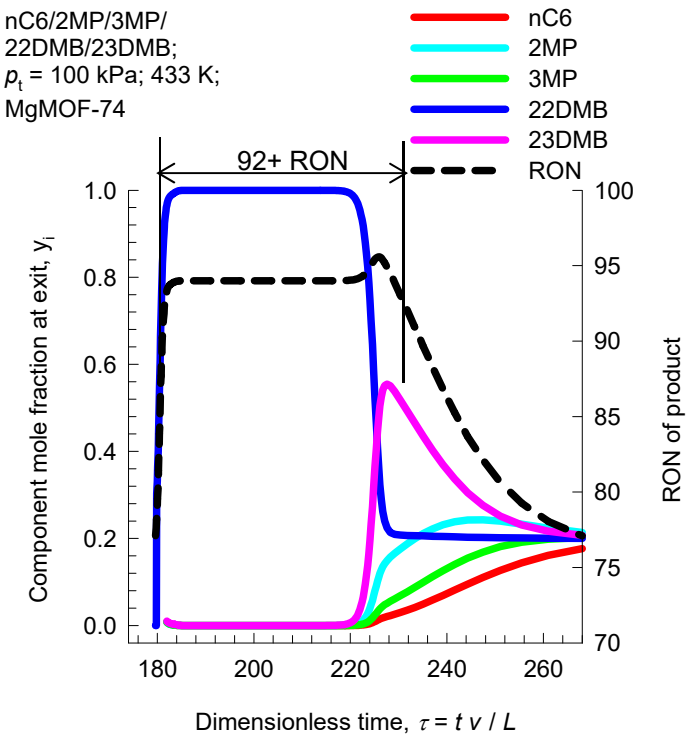

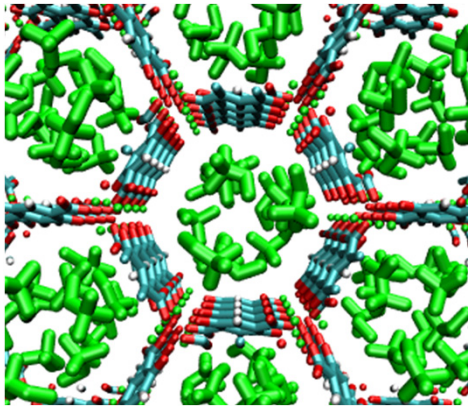

22DMB

Breakthrough simulations for ZnMOF-74

Figure S39

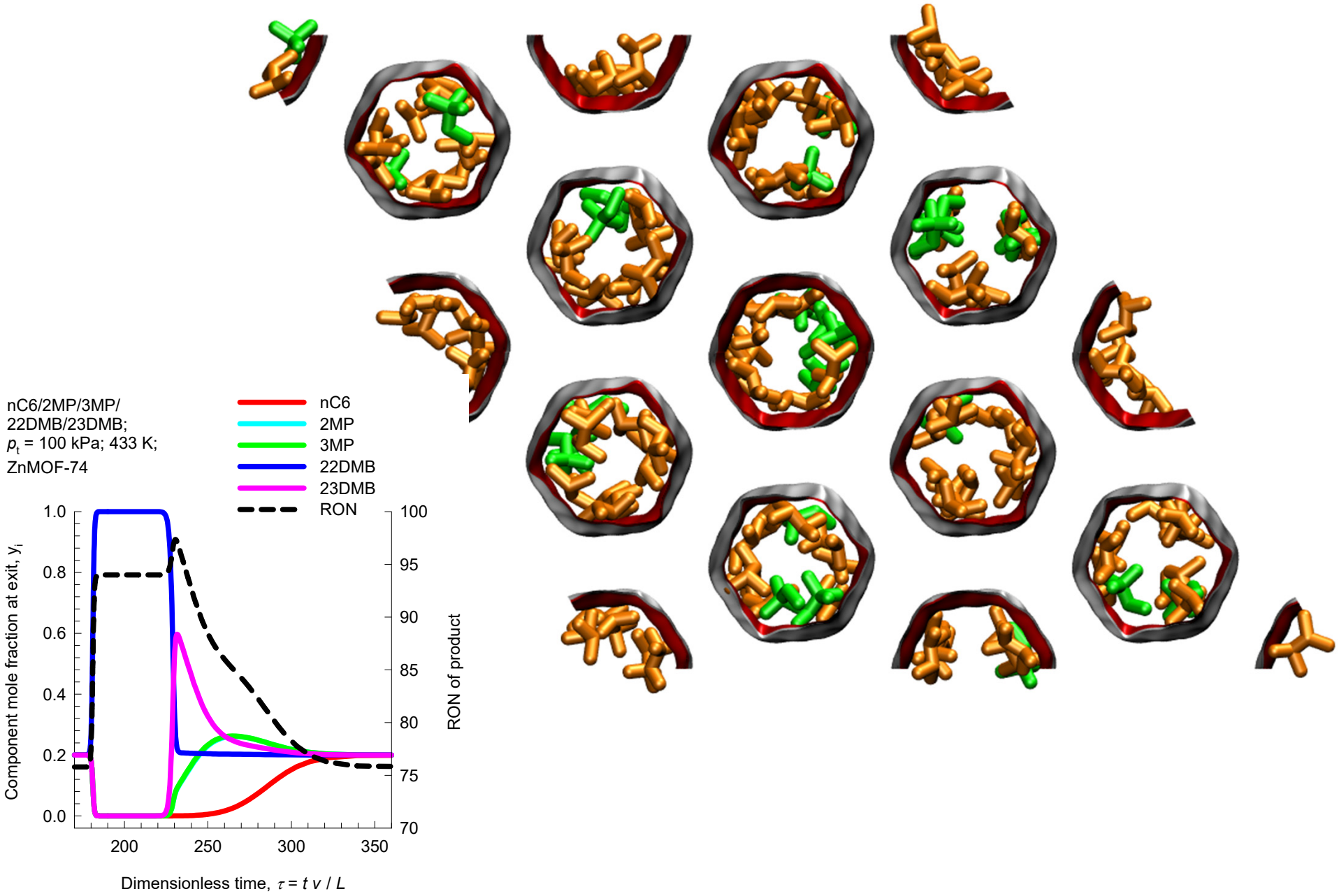

Breakthrough simulations for ZIF-8

Figure S40

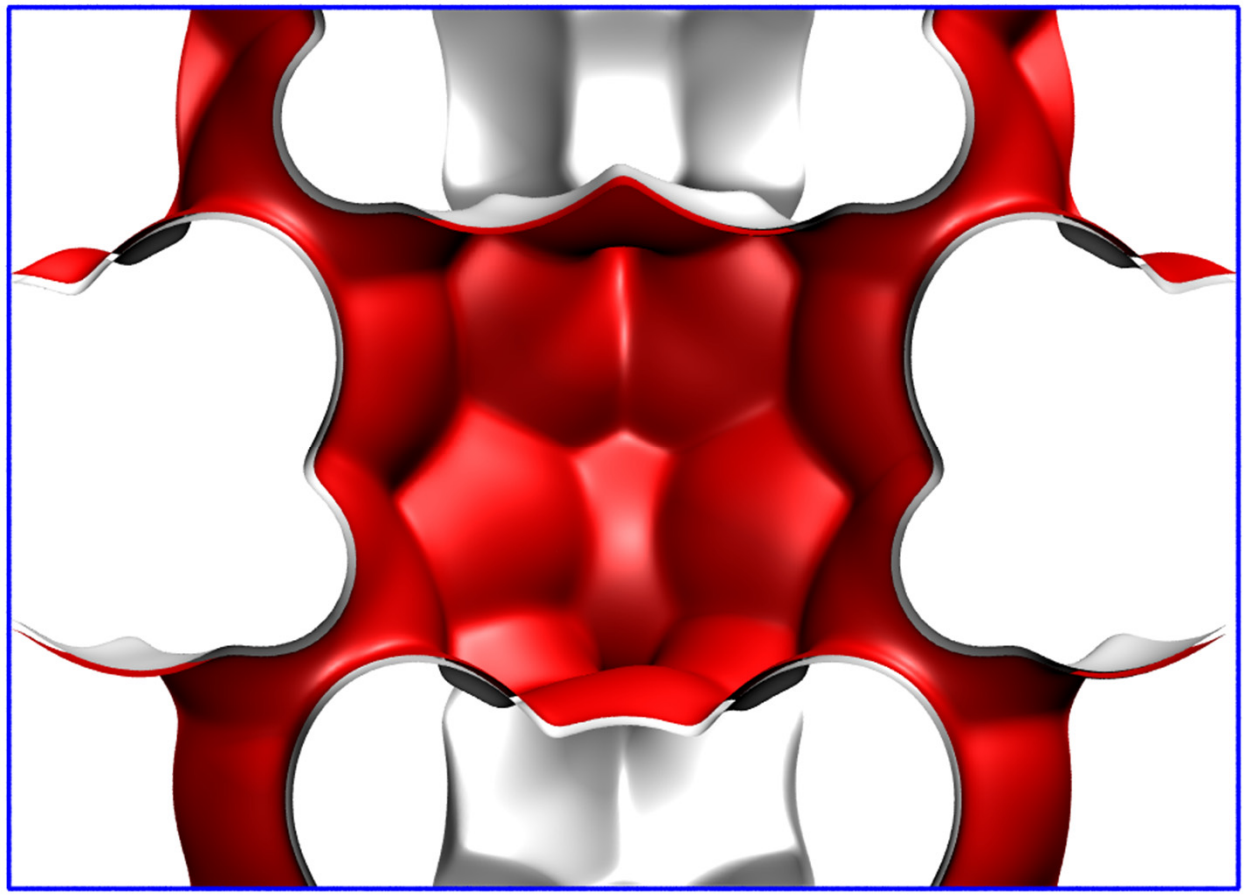

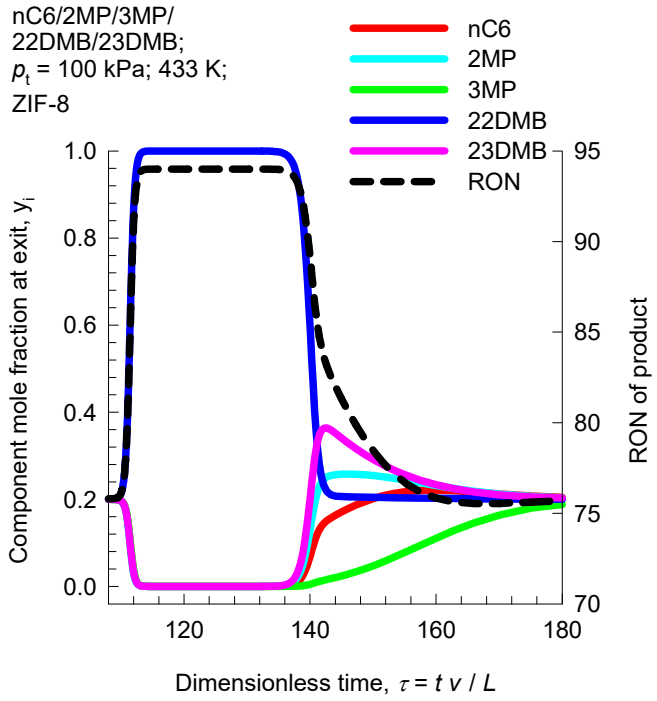

Breakthrough simulations for BEA

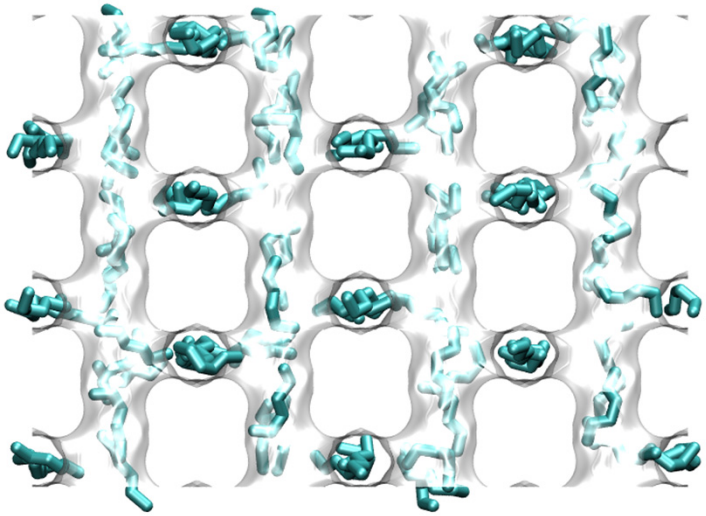

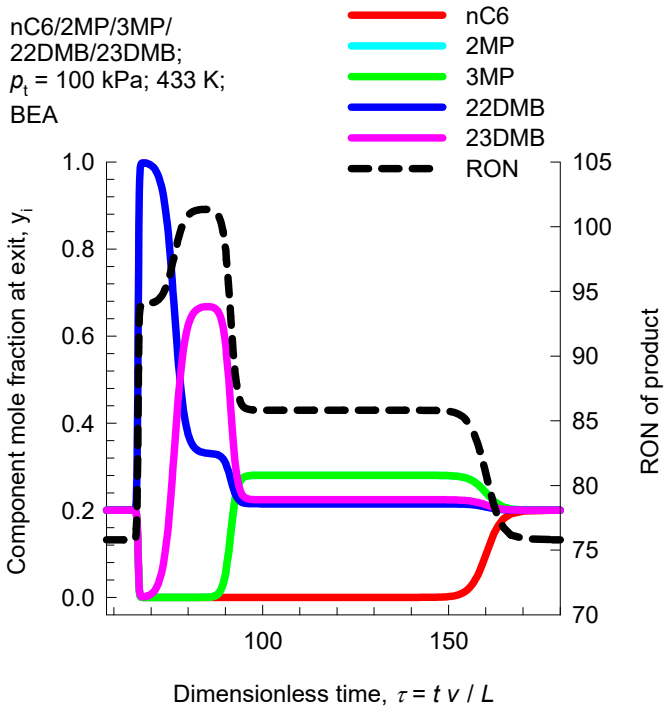

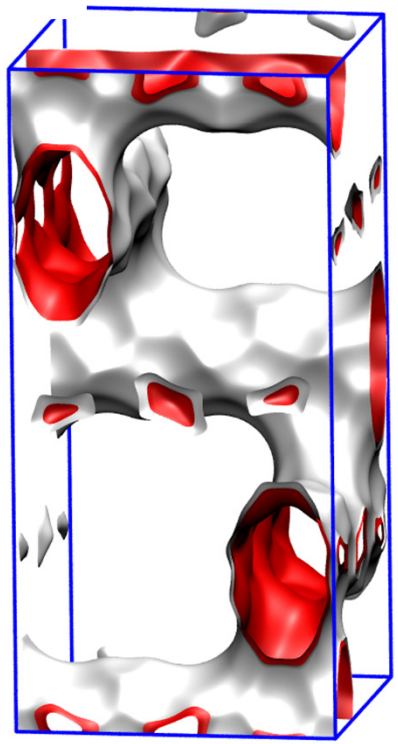

Figure S42

Breakthrough simulations for ZnHBDC

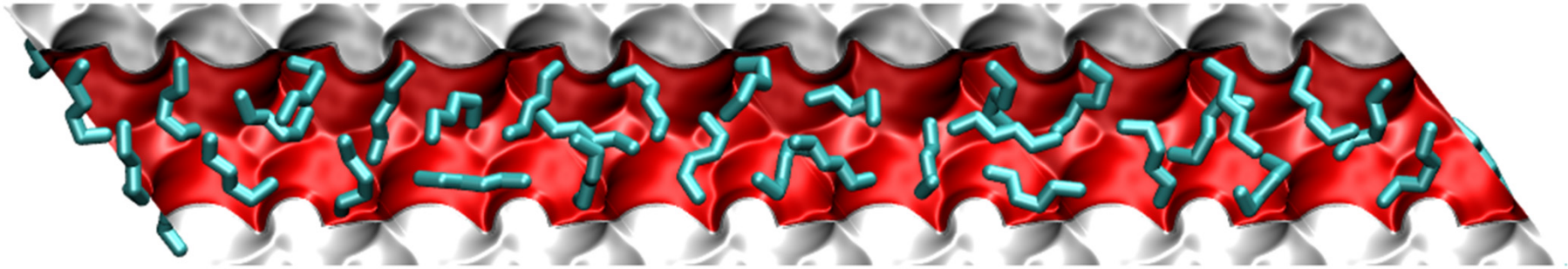

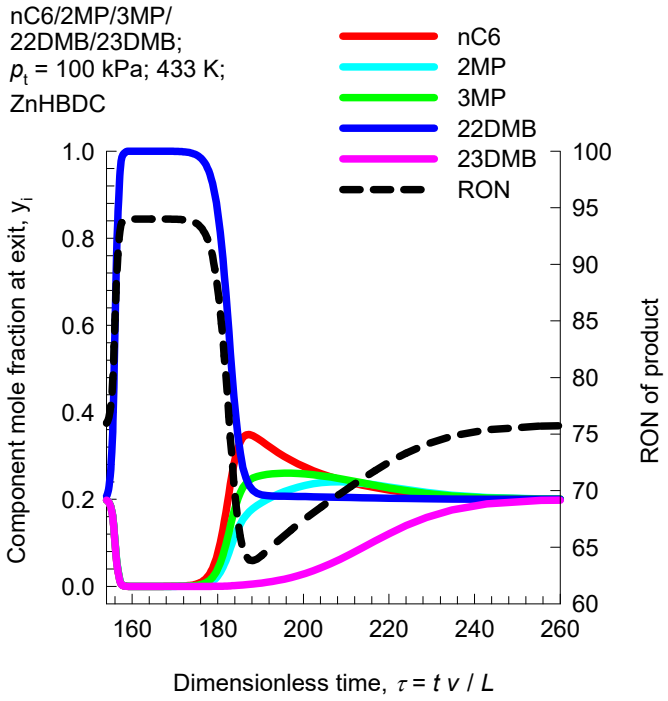

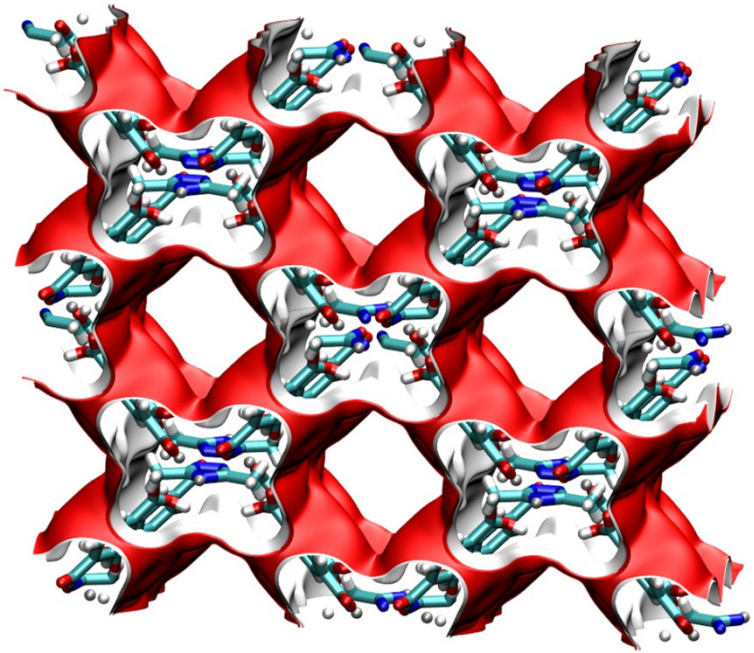

Breakthrough simulations for Zn(bdc)dabco

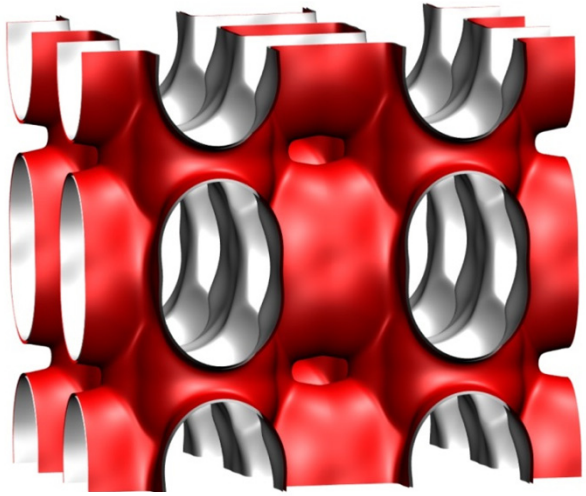

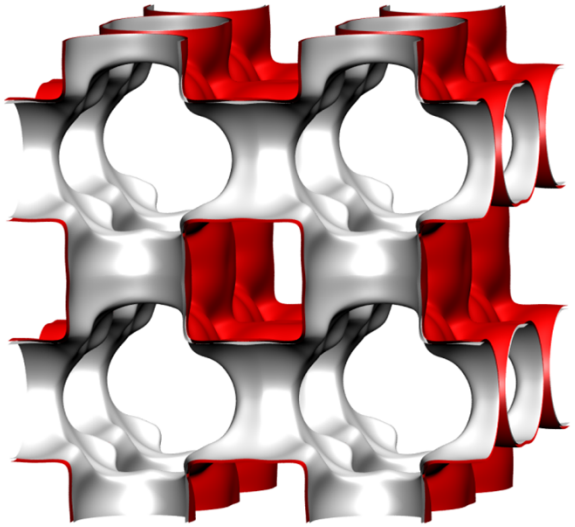

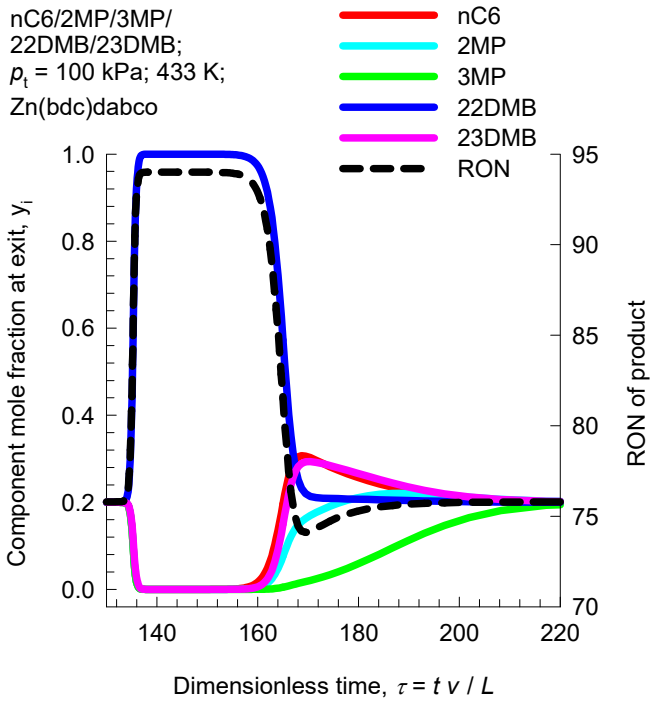

Figure S44

Adsorption/desorption cycles for UiO-66

Equilibrium breakthrough simulations

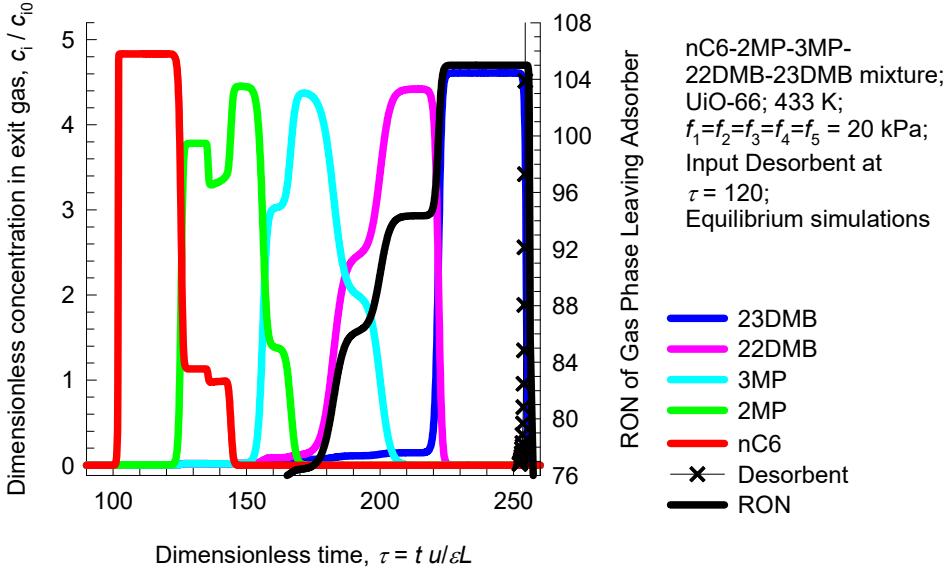

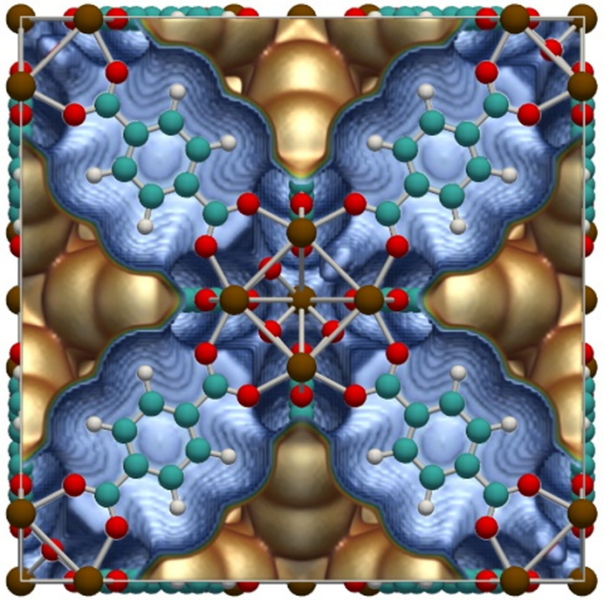

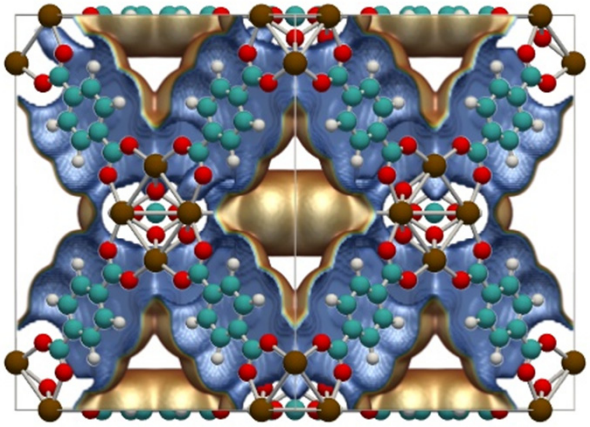

Breakthroughs with diffusional limitations

Adsorption/desorption cycles for CFI

Figure S45

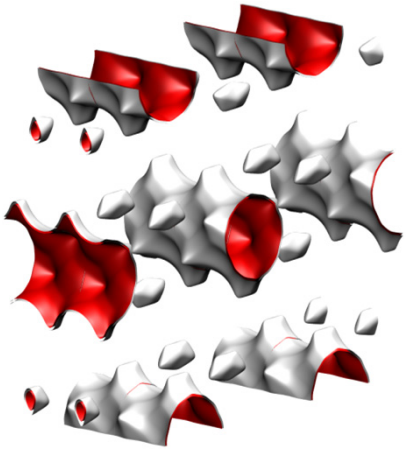

Length entropy effects cause the reverse adsorption hierarchy

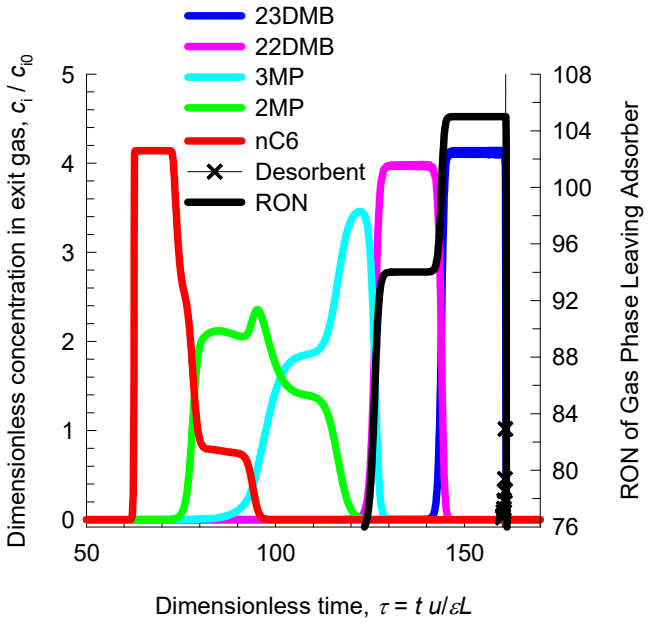

nC6-2MP-3MP-22DMB-23DMB mixture; CFI; 433 K; $f_1=f_2=f_3=f_4=f_5$ = 20 kPa; Input Desorbent at τ = 70; Equilibrium simulations

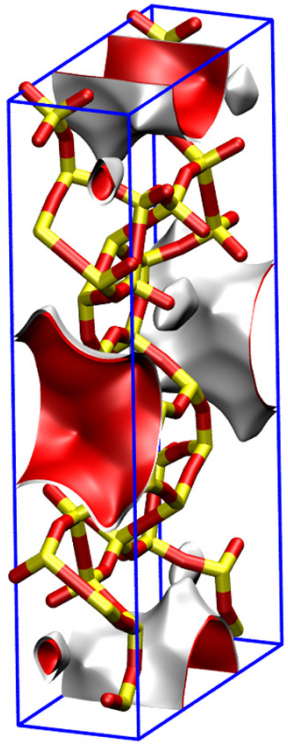

Adsorption/desorption cycles for ATS

Figure S46

Length entropy effects cause the reverse adsorption hierarchy

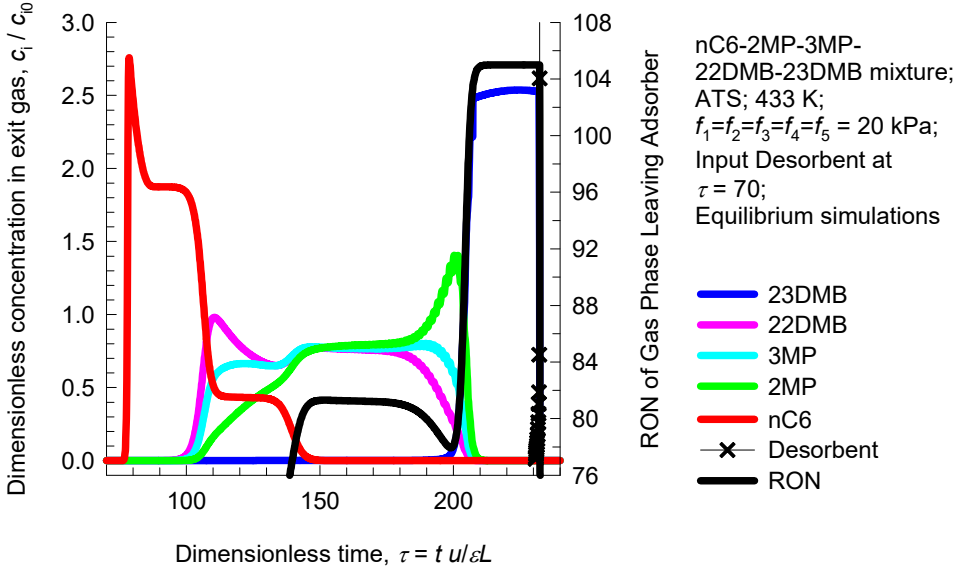

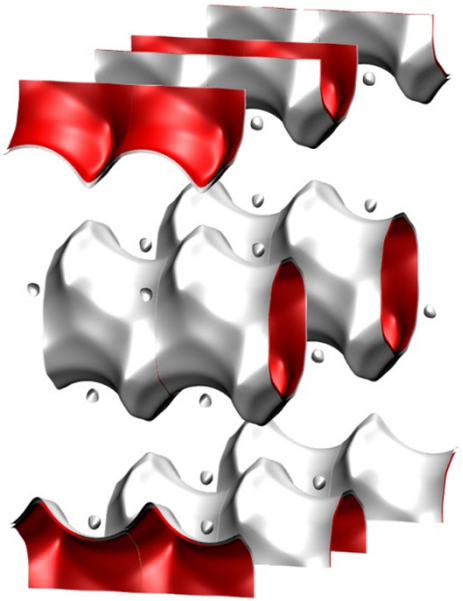

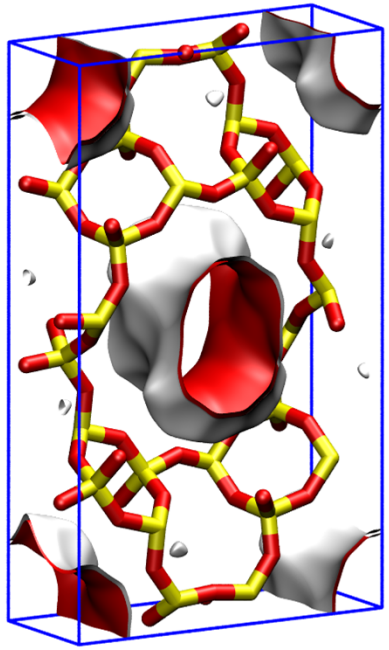

Figure S47

Separating nC6/2MP/3MP/22DMB/23DMB mixtures

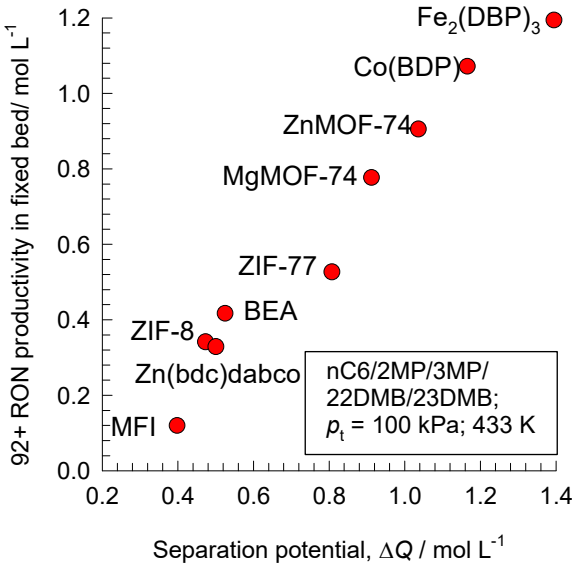

Figure S48

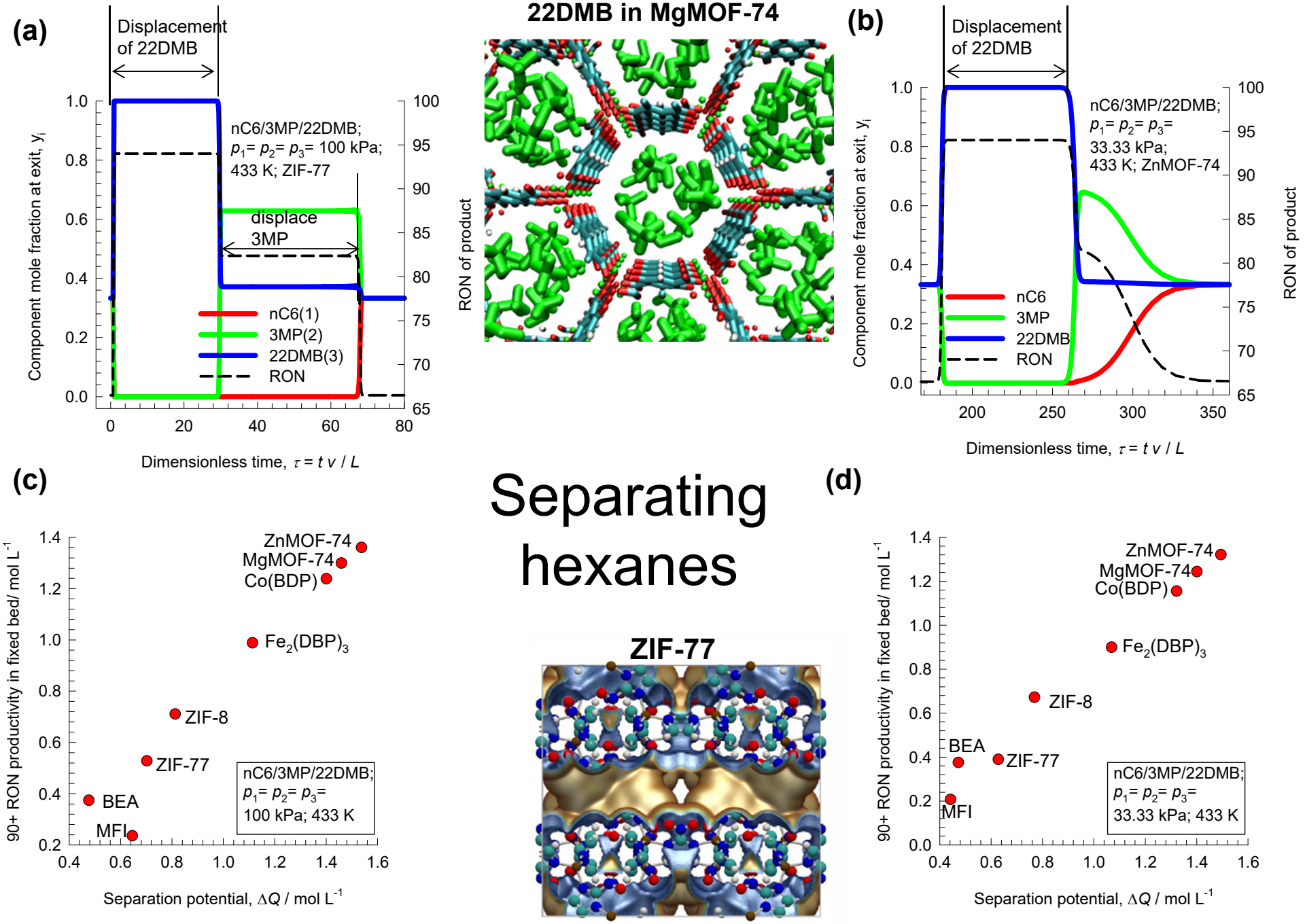
(a)
Displacement of 22DMB
displace 3MP
nC6/3MP/22DMB; p_1= p_2= p_3= 100 kPa; 433 K; ZIF-77
nC6(1)
3MP(2)
22DMB(3)
RON
Component mole fraction at exit, y_i
RON of product
Dimensionless time, $\tau = t\,v\,/\,L$
22DMB in MgMOF-74
(b)
Displacement of 22DMB
nC6/3MP/22DMB; p_1= p_2= p_3= 33.33 kPa; 433 K; ZnMOF-74
nC6
3MP
22DMB
RON
Component mole fraction at exit, y_i
RON of product
Dimensionless time, $\tau = t\,v\,/\,L$
Separating hexanes
(c)
ZnMOF-74
MgMOF-74
Co(BDP)
$Fe_2(DBP)_3$
ZIF-8
ZIF-77
BEA
MFI
nC6/3MP/22DMB; p_1= p_2= p_3= 100 kPa; 433 K
90+ RON productivity in fixed bed/ mol L^{-1}
Separation potential, ΔQ / mol L^{-1}
ZIF-77
(d)
ZnMOF-74
MgMOF-74
Co(BDP)
$Fe_2(DBP)_3$
ZIF-8
BEA
ZIF-77
MFI
nC6/3MP/22DMB; p_1= p_2= p_3= 33.33 kPa; 433 K
90+ RON productivity in fixed bed/ mol L^{-1}
Separation potential, ΔQ / mol L^{-1}

Figure S49

Separating Xylene isomers

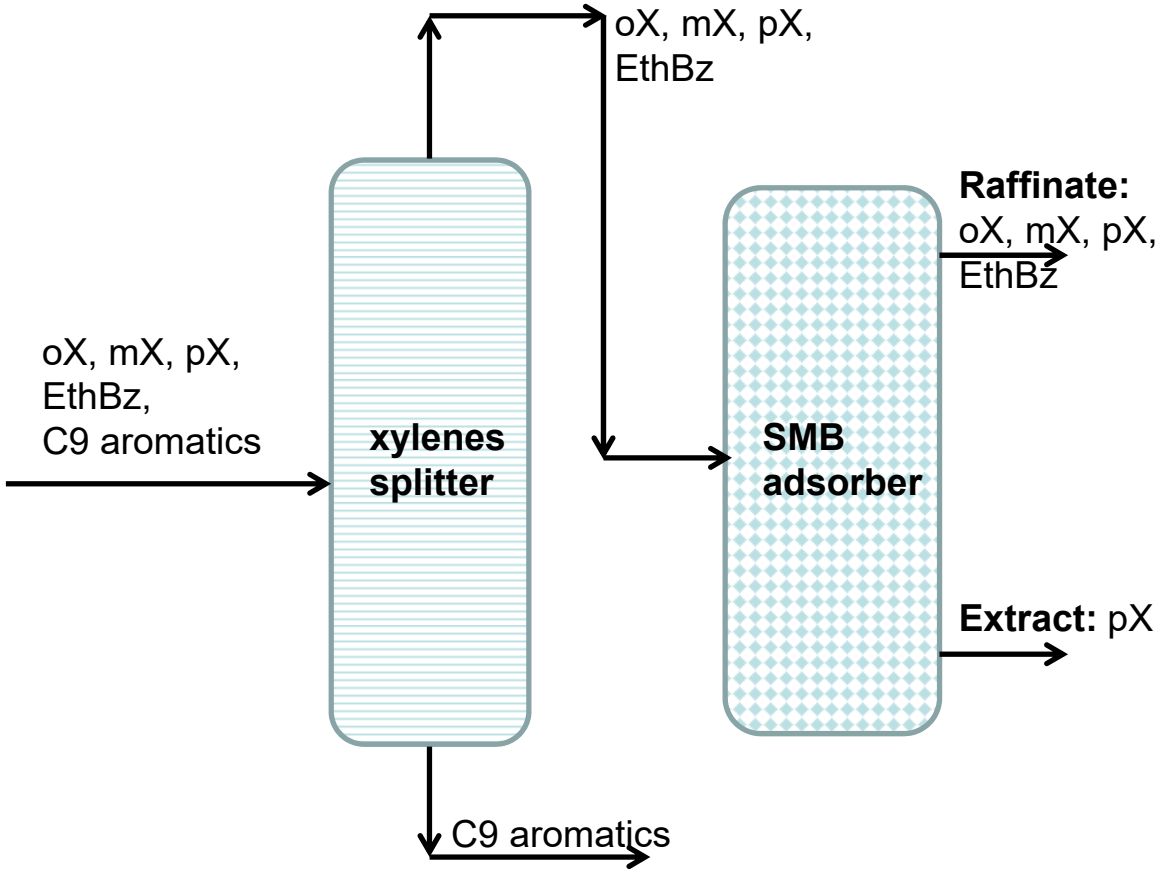

Figure S50

Separating Xylene isomers

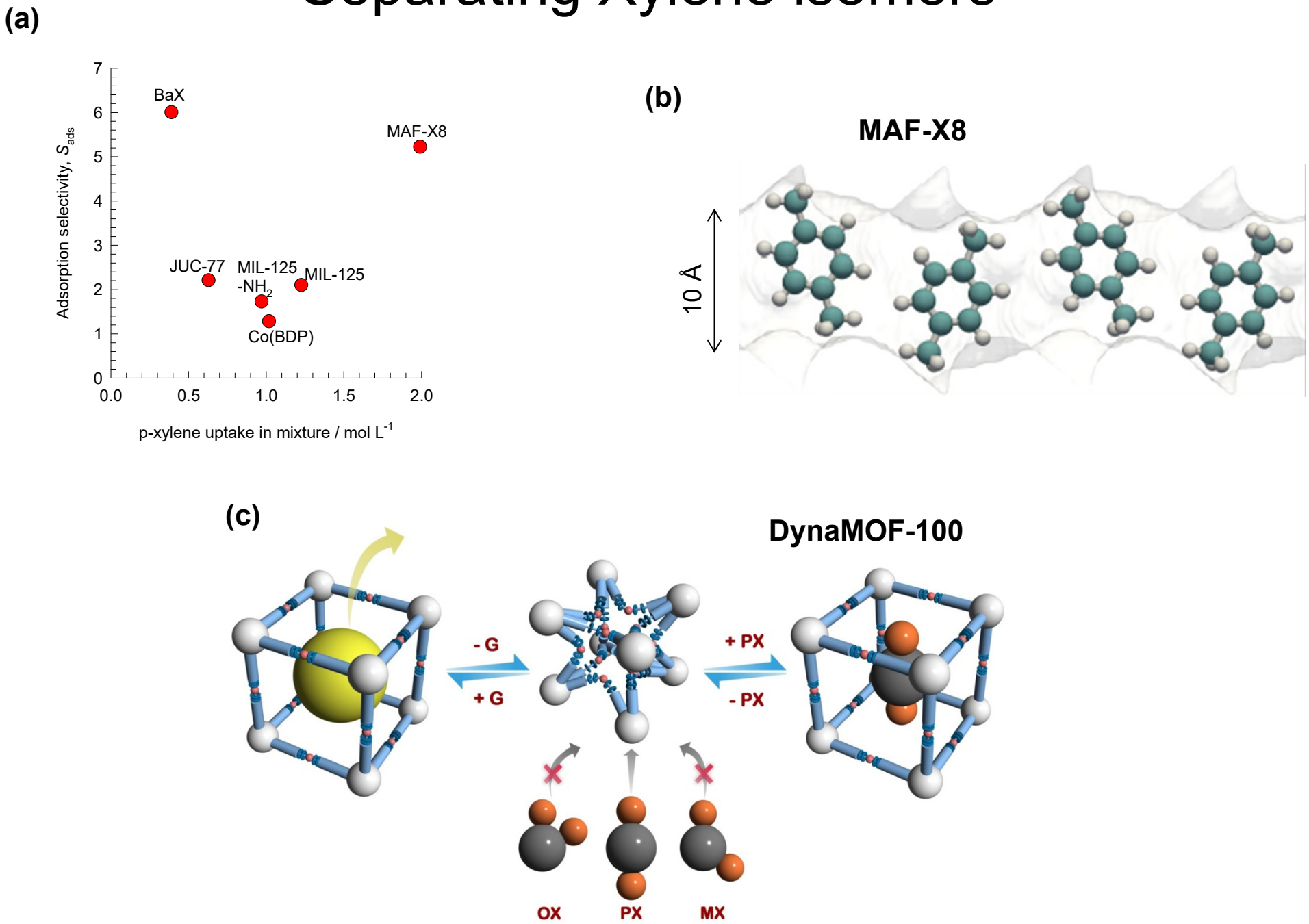

Separating Xylene isomers

Figure S51

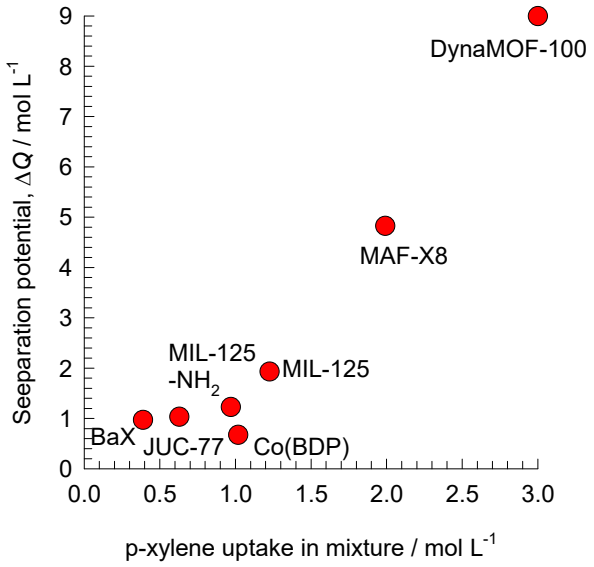

Figure S52

Separating Ethylbenzene/Styrene

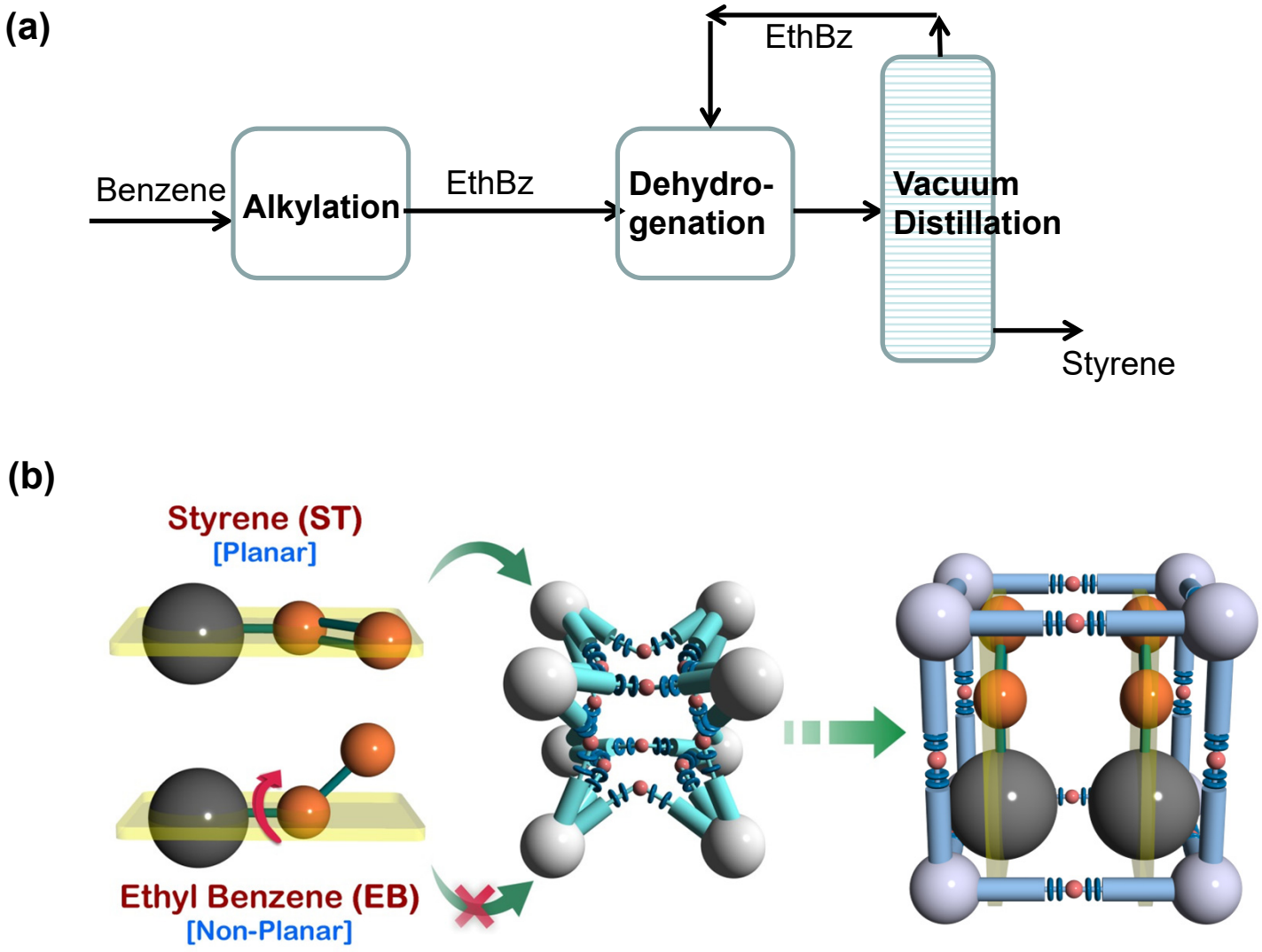

Figure S53

Separating Ethylbenzene/Styrene